Czech Technical University in Prague
Faculty of Electrical Engineering
Department of Electromagnetic Field

# Prospective Methods for Optimal Design of Electrically Small Antennas

Doctoral Thesis

Vít Losenický

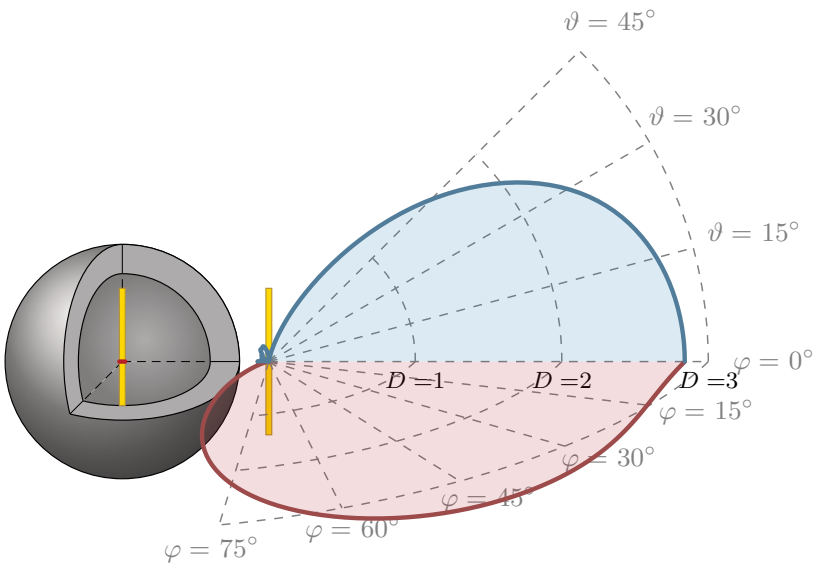


Prague, the Czech Republic — November 2023

Czech Technical University in Prague

Faculty of Electrical Engineering
Department of Electromagnetic Field

# Prospective Methods for Optimal Design of Electrically Small Antennas

Doctoral Thesis

*Author:* Ing. Vít Losenický

*Supervisor:* doc. Ing. Miloslav Čapek, Ph.D.
*Supervisor-Specialist:* doc. Ing. Lukáš Jelínek, Ph.D.

*Ph.D. program:* Electrical Engineering and Information Technology – P2612
*Branch of studies:* Radioelectronics – 2601V010

Prague, the Czech Republic — November 2023

*You don't have to be a hero to accomplish great things—to compete. You can just be an ordinary chap, sufficiently motivated to reach challenging goals.*

Edmund Hillary

# Declaration

"I hereby declare I have written this thesis independently and have quoted all the sources of information used in accordance with the methodological instructions on ethical principles for writing an academic thesis. Moreover, I state that this thesis has neither been submitted nor accepted for any other degree."

In Prague, November 15, 2023

.....
Vít Losenický

# Acknowledgement

I want to express my sincere gratitude to all those who supported and encouraged me throughout my research journey. First and foremost, I would like to thank my supervisors, Miloslav Čapek and Lukáš Jelínek, for their guidance, wisdom, expertise, and a great deal of patience. Their insightful feedback and constructive criticism have been invaluable in completing this thesis.

I am grateful to my colleagues and friends who have supported and encouraged me along the way, providing me with the necessary motivation to carry out this research. Additionally, I would like to thank prof. Daviu and prof. Gustafsson, who allowed me to visit their research groups and gain valuable information and life experiences.

Finally, I would like to acknowledge the unwavering support of my family. Their love, encouragement, and patience have been the foundation of my success. Without their support, this achievement would not have been possible.

Thank you all for your invaluable contributions to the completion of this thesis.

# Abstrakt

Tato práce se zabývá využitím vektorových sférických vln ke studiu charakteristických módů, k určování principiálních limitů a dále také ke kombinaci metody momentů s T-maticovou metodou. Základním poznatkem této práce je nalezení analytického předpisu pro charakteristické módy kulové slupky a jeho využití pro testování numerické přesnosti dostupných řešičů charakteristických módů. Na základě těchto výsledků je definován nový postup pro určení charakteristických módů, který využívá rozkladu Greenovy funkce do sférických vln, což umožňuje dosáhnout vyšší numerické dynamiky a rychlejšího výpočtu. Toho je dosaženo mimo jiné pomocí nově vytvořené projekční matice, která definuje vztah mezi lokálními bázovými funkcemi a sférickými vlnami. Tato matice je dále použita pro definici interakce mezi impedanční maticí a T-maticí. Dalším využitím rozkladu elektromagnetického pole do vektorových sférických vln je stanovení principiálních limitů vyzařovací účinnosti dvou soustředných kulových plášťů, což přispívá k lepšímu pochopení modelu ztrát v dobře vodivých objektech. Poslední aplikací rozkladu je použití projekční matice k sestavení hybridní metody pro analýzu interakce mezi elektricky malým zářičem a pasivním rozptylovačem. Tato metoda využívá poznatků získaných studiem analytické reprezentace charakteristických módů ke kombinaci metody momentů s T-maticovou metodou.

**Klíčová slova:** Návrh antén, počítačové simulace, metoda momentů, modální analýza, principiální limity, metoda T-matice.

# Abstract

Spherical wave expansion and numerical methods based on integral equations are utilized in this thesis to study various aspects of characteristic mode decomposition, the determination of fundamental bounds, and the hybridization of the method of moments and T-matrix. The numeric precision of characteristic mode solvers is validated and compared with the analytic solution, leading to recommendations and testing cases for authors of both academic and commercial packages. Inspired by the conclusions of this benchmark study, a new technique for decomposing characteristic modes is developed utilizing Green's function separation into regular and outgoing spherical vector waves. The results have higher numerical dynamics and are evaluated faster. The projection matrix between spherical vector waves and piece-wise basis functions has been established, featuring many direct applications, such as determining the radiation matrix, determining characteristic modes, and mediating the interaction between the impedance matrix and the T-matrix. The definition of the modal Q-factor is modified to be valid outside the modal resonance. The fundamental bound on radiation efficiency for an arrangement of two concentric spherical shells is found analytically. This study helps to understand the thin-sheet model used for other numerical models and to estimate its precision based on comparisons with a numerical code. Finally, a hybrid method for analyzing the interaction between an electrically small radiator and a passive scatterer is developed using the insights gained by studying the analytical representation of the characteristic modes to combine the method of moments with the T-matrix method.

**Key Words:** Antenna design, computer simulation, method of moments, modal analysis, fundamental bounds, T-matrix method.

# Contents

# 1 Introduction

Antennas have been an integral part of wireless devices since the beginning of radio communication and long-distance transmission [1]. In those early days, the need to use low frequencies [2] and the inability to build antennas with dimensions comparable to the wavelength caused the first antennas to be electrically small [3]. Radio and antenna technology gradually evolved, increasing operational frequencies and the electrical dimensions of antennas. Nevertheless, electrically small antennas (ESAs) did not disappear and have become increasingly important in handheld wireless communication devices.

Antennas are responsible for converting electrical signals into electromagnetic waves, and vice versa, which makes them an essential component of communication systems such as cellular networks [3], satellite communications [4], and wireless sensor networks [5]. The performance of these systems heavily depends on the effectiveness of the antenna design [6]. In addition, with the continuous development of wireless communication devices, their compact size is becoming an essential design parameter. Simultaneously, the complexity of these devices is increasing, leading to competition between all used functional components. This also applies to antennas that do not benefit from size reduction, which deteriorates their performance. Engineers and researchers are, therefore, investigating various techniques to optimize antenna structures to obtain the best possible performance with acceptable design complexity.

The subject of antenna design is the search for optimal shapes, material distribution, and feeding schemes [3], a problem of immense complexity. These three primary attributes are essential in determining current distribution and, consequently, the radiation parameters of the antenna. One of the main challenges in antenna design is the complexity of the electromagnetic field equations that govern their behavior. Antenna designers use manufacturing and measurement, analytical methods, and numerical simulations to achieve desired performance. The design can then be approached using various strategies, from trial-and-error, using the designer's experience, to topological optimization [7]. In general, the design process is iterative regardless of the procedure used, and if the resulting design parameters do not meet the required specifications, the model is modified, and the determination of its parameters is repeated.

Advanced numerical computational methods have received considerable attention and popularity in recent decades. This is primarily due to the growth in computational power, the growing number of publications on these topics, and the associated development of software tools for the simulation of electromagnetic problems that include these methods as standard features. One particularly intriguing and powerful

concept in this context is the characteristic mode (CM) analysis [8–10] as characteristic modes represent an innovative approach to understanding and analyzing complex electromagnetic structures. They offer a systematic way to investigate resonant behavior and energy distribution within a given structure, making them an indispensable tool for designing and optimizing various devices, from antennas to microwave circuits. The increasing adoption of CM analysis in academia and industry has become a key component of advanced numerical computational methods for solving electromagnetic problems. Nevertheless, it has also shown many scenarios for which the current CM solvers are poorly prepared. This can be illustrated by a modal analysis of an electrically small device that operates near a large conducting platform, a case often used in practice.

In parallel with the development of CM analysis, researchers have also been exploring fundamental bounds within electromagnetic systems [11]. These bounds represent theoretical limits on the performance of electromagnetic devices and are essential for benchmarking and optimizing designs. As mentioned earlier, antenna design is a complex process that requires the careful consideration of various factors, including available space and materials. By understanding these fundamental bounds, engineers and scientists can push the boundaries of what is achievable. Despite the successes of determining bounds on various parameters [12–20], there are still various tasks, such as determining bounds for multiple frequencies simultaneously or bounds for tasks with various local constraints for which the correct formulation of optimization tasks is not known.

This thesis uses spherical expansion to overcome the numerical imperfections of CM theory and the evaluation of fundamental bounds. Specifically, an analytical representation of the characteristic modes for a perfectly electrically conducting spherical shell, expressed through spherical harmonics, is used to determine the fundamental bound on the radiation efficiency in the spherical region and to verify the capability of commercial and in-house computational tools for CM analysis which makes it possible to determine the critical bottlenecks in determining CMs. Some of these problems are then addressed by suggesting an alternative way of determining the real part of the system matrix using a decomposition of the dyadic Green's function into spherical vector wave functions. This procedure creates, as an intermediate product, a projection operator connecting the space of local basis functions and the space of domain-wide basis functions in the form of spherical vector waves. This is then advantageously used in the definition of hybrid numerical methods to analyze the interaction between a small radiator and an object in its vicinity. The thesis also shows that the original definition of the CMs using the perturbation operator [8] and the definition of the CMs using the impedance operator [9] form the same characteristic basis and, in addition, it is possible to switch between these bases using the projection operator arbitrarily.

## 1.1 Structure of the Thesis

This thesis is divided into two parts. The first part, Chapter 2, is a detailed review of the current state-of-the-art, focusing on identifying the existing gaps and limitations in the literature. The open problems considered as this thesis' objectives are defined at the end in Section 2.6. This review serves as the foundation for the second part of the thesis, which addresses the means of filling these gaps. Chapter 3 briefly summarizes the individual publications listed in journals with impact factor (*IEEE Transactions on Antennas and Propagation*) and/or in the

proceedings of prestigious international conferences (*EuCAP*, *IEEE AP-S/URSI*) where the solutions to the thesis objectives were published. The thesis is concluded in Chapter 4. The publications listed in Chapter 3 are reprinted in Appendix A–E. The bibliography of the thesis and all publications are merged at the end into one list so that the reprinted publications have different numbering than the original journal papers.

Out of sheer curiosity about the capabilities of modern generative neural networks, one of the paragraphs in this thesis is created using the ChatGPT-3.5 language model [21], and it is up to the reader to guess which paragraph it is.

# 2 State of the Art

The antenna is a principal component of any wireless radio communication device, transforming the signal as a guided wave impinging on its terminal into waves propagating through the environment and vice versa. One main class of antennas is the so-called ESAs, further described in Section 2.1[1].

Electromagnetic problems involving antennas are of a wide variety, so a range of procedures of computational electromagnetism (CEM) have been developed to analyze and determine individual electromagnetic quantities. Several of these methods are often used to analyze ESAs. Among the group of differential methods, *i.e.*, methods based on the solution of Maxwell's equations in differential form, the finite element method (FEM) [22] and finite-difference time-domain (FDTD) [23] method are used. From the group of integral methods, the method of moments (MoM) [24] is widely used.

Two computational methods used in this thesis, MoM [24] and the T-matrix method [25], are introduced in Section 2.2 and compared in Section 2.2.3. MoM uses Green's function [26] to transform Maxwell's equations into a field integral equation, which is further reduced to a numerically tractable matrix, while the T-matrix method utilizes the interface condition between two different materials to express field scattering in the form of a matrix. Access to a matrix fully characterizing the system makes it possible to study its principal states, *i.e.*, its spectrum [27], or to estimate fundamental bounds on the performance of any device which occupies a subspace spanned by the operator [28]. The fact that both MoM and T-matrix methods are based on matrices allows us to hybridize them and emphasize their good properties. With that, we can effectively address scenarios that were impossible before.

Although these are common and well-studied approaches to analyzing radiation structures, each of these algorithms has its benefits and limitations. In the case of ESAs, it appears that it is favorable to use modal methods [29] which can separate the effect of the shape of an antenna and its way of excitation. The advantage of such a description of electrically small antennas is that for the selected quantities, *e.g.*, Q-factor, gain, or radiation efficiency, it is necessary to know only a small set of modes (only units of modes), the contribution of the other modes being so small that it can be neglected. Modal methods are generally presented in Section 2.3, and their specific implementation in the form of CMs is shown in Section 2.3.1. Determining

[1] For the purpose of this thesis, an antenna is considered to be a reciprocal passive linear time-invariant system.

the CMs is a numerical method based on the decomposition of matrices that can be affected by many influences [30–33]. For this reason, it is necessary to address the issue of the accuracy of their determination and to systematically verify the available solvers, which is briefly summarised in Section 2.4.

It is also possible to determine the modal electromagnetic quantities associated with the set of modes, which can be further used in seeking the principal limits (fundamental bounds) of an antenna parameter. To perform a modal analysis or to determine fundamental bounds, it is necessary to determine operators describing the radiation structure. These operators, usually in the form of matrices, represent a discretized field equation using appropriate boundary conditions. The concept of fundamental bounds is briefly summarized in Section 2.5.

## 2.1 Electrically Small Antennas

Electrically small antennas are characterized by their small size compared to the wavelength of operation. An object is said to be electrically small if its largest dimension is less than $\lambda/2\pi$ [34]. The same definition can be expressed using the wave number $k$ and the radius of the smallest circumscribing sphere $a$, which defines the electrical size as the product $ka$. An antenna is then considered electrically small if $ka < 0.5$ [35].

The electrical size is not just a general description of antenna size but also an essential parameter that significantly affects its possible performance. The reduction of electrical size inevitably leads to a deterioration of its performance, even though efforts are made to preserve the characteristics of antennas of much larger electrical sizes. The performance of ESAs is commonly characterized by their input impedance, radiation efficiency, fractional bandwidth (Q-factor), and directivity [36, 37]. These parameters and how they are affected by electrically small size are as follows:

- **The input impedance** of ESAs typically exhibits a significant reactive nature, with the exception of specific narrow frequency bands. Thus ESAs, in most cases, operate deep below their self-resonance [36, 37]. This has far-reaching consequences. ESAs must, in most cases, be equipped with additional matching circuits that connect the antenna and its feeding with maximal power transfer and minimal reflection. The high reactance also influences the shape of the frequency dependence of the input impedance, which is very steep in the resonance region of ESAs, which affects other radiation parameters such as fractional bandwidth.
- **Radiation efficiency** is the ratio between cycle mean power lost by radiation and total cycle mean lost power, which is lost by radiation and thermal dissipation [38]. In the case of ESAs, efficiency is usually low due to the low radiation resistance and the large absolute value of input reactance. However, the loss resistance of the coupling circuits, which are prewired to the antenna for these impedance values, may outweigh the antenna's radiation resistance, resulting in a low ratio between radiated and lost energy [37], and, thus, a significant reduction of the radiation efficiency.
- **The bandwidth** of an antenna is the frequency range in which the antenna can effectively transmit or receive a signal. Thus, the bandwidth is the difference between the highest and lowest frequencies in the band in which the antenna meets the given parameters, usually defined by the input impedance. ESAs have only a very narrow bandwidth because they have very steep reactance

characteristics [37]. The bandwidth of an antenna can be conveniently defined using fractional bandwidth, which, for single resonance antennas, is inversely proportional to the Q-factor [39], thus the fractional bandwidth can also be approximated by the ratio between cycle mean radiated and stored energy [36]. The inverse relationship between the fractional bandwidth and the Q-factor is crucial, mainly because of the determination of the lower fundamental bounds of the Q-factor and, therefore, the maximum bandwidth.

- **The directivity** of an antenna is a fundamental parameter that characterizes its ability to concentrate radiated energy in a specific direction. It is defined as the ratio of the radiation intensity emitted in a particular direction to that of an isotropic source [6], which radiates uniformly in all directions. In the case of ESAs, the directivity can theoretically assume a wide range of values [40]. However, due to practical considerations and design choices, antennas often radiate in patterns resembling that of an electric or magnetic dipole [37], resulting in a typical directivity value of around 1.5. Directivity is closely intertwined with gain, a metric that combines the antenna's directivity and radiation efficiency [6], offering insight into how well the antenna transforms power incident on its terminal into radio waves transmitted in a particular direction. For ESA, the gain is primarily influenced by the antenna's radiation efficiency, which plays a central role in cases where the directivity hovers around 1.5 [41]. It is worth noting that even if the directivity exceeds this value, it does not necessarily enhance gain, as such designs typically exhibit reduced efficiency. In the case of realistic small antennas, the main limitation of gain is a thermal loss, which, even if small, limits its value to a finite number [40].

A typical ESA is therefore characterized by a small bandwidth, featuring predominantly reactive input impedance with small radiation resistance, which complicates their impedance matching to other microwave components, radiated power that is only a fraction of the incident power, *i.e.*, small radiation efficiency, and a naturally omni-directional radiation pattern which is not suitable for all applications. Optimization of these multiple parameters is usually contradictory, meaning that the improvement of one parameter negatively influences the others. Therefore, the optimality of ESAs' performance is multi-criteria optimization which seeks an optimal trade-off between its parameters [42].

## 2.2 Method of Moments and T-matrix Method

### 2.2.1 Method of Moments

The MoM is a full-wave numerical approach suitable for solving small to medium-sized open boundary problems of arbitrary shapes. It is typically used in the frequency domain to solve electromagnetic radiation and scattering problems [24]. The essence of the method is converting a linear integrodifferential equation into a system of linear equations, usually represented by a system matrix and an excitation vector [24]. This conversion consists of three successive steps. At first, the geometry of the object is divided into small segments. In the next step, basis functions are assigned to expand the unknown quantity. Finally, a set of linearly independent equations is obtained by testing the governing equation with testing functions.

An in-homogeneous equation can express the original electromagnetic problem to be solved as

$$\mathcal{L}(f) = g, \tag{2.1}$$

in which $\mathcal{L}$ represents linear operator, $f$ is a reaction of a system, and $g$ is excitation.

The discretization of geometry represents an initial step for many electromagnetic numerical methods in which the conversion of continuous geometry to its representation through geometric cells takes place. There are several ways of discretization, which differ according to cell shape [43].

The next stage of the process is the introduction of basis functions over the discrete grid, which decomposes the exact solution of the problem in the domain of operator $\mathcal{L}$ into a finite set of basis functions

$$f \approx \sum_n \alpha_n f_n, \tag{2.2}$$

where $f_n$ is the set of basis functions and $\alpha_n$ are unknown weighting coefficients. This decomposition is then substituted to the original problem using the linearity of operator $\mathcal{L}$, which can be rewritten as

$$\sum_n \alpha_n L(f_n) \approx g. \tag{2.3}$$

For example, in the case of a three-dimensional perfect electric conductor (PEC) surface, Rao-Wilton-Glisson (RWG) basis functions [44] are used in connection with a triangular segmentation (due to its conformity with arbitrarily curved surfaces [45]).

The last step to transform (2.1) into a system of linear equations in matrix form is a testing procedure. To this end, a set of testing functions $w_m$, and a suitably defined [24] inner product $\langle a, b\rangle$ are applied to (2.3). When testing functions match with basis functions, $w_m = f_m \quad \forall m$, the procedure is called Galerkin testing and yields symmetric matrices [46]. The result of the testing using the inner product properties [24] can be formally written as

$$\sum_n \alpha_n \langle w_m, L f_n\rangle = \langle w_m, g\rangle, \tag{2.4}$$

which is generally expressed as a matrix equation

$$\mathbf{L}\boldsymbol{\alpha} = \mathbf{g}, \tag{2.5}$$

where $\mathbf{L}$ represents a system matrix that preserves the properties of the original integrodifferential operator and fully describes the analyzed object so that by using an arbitrary excitation $\mathbf{g}$, it is possible to obtain the field response $\mathbf{f}$ represented by the set of weighting coefficients $\boldsymbol{\alpha}$.

For a particular solution of MoM applied to electric field integral equation (EFIE) [47], the resulting matrix notation is usually written as

$$\mathbf{ZI} = \mathbf{V}, \tag{2.6}$$

in which $\mathbf{Z}$ is referred to as an impedance matrix, external sources are represented by the excitation vector $\mathbf{V}$, and the unknown weighting coefficients of the basis functions, understood as current distribution, are represented by vector $\mathbf{I}$.

Applying MoM to solve radiation and scattering problems leads to a matrix equation that allows a simple calculation of current density $\mathbf{I}$ induced in response to excitation by external electromagnetic field $\mathbf{V}$. A further result of applying this method is also the impedance matrix $\mathbf{Z}$. This matrix represents the discretized field integral equation for a given electromagnetic problem and is, therefore, dense and implicitly contains boundary conditions. This differs from other procedures, such as FEM or FDTD, where the matrix is usually sparse. Given that the impedance matrix is dense, it allows applying an inversion or decomposition. These procedures are further used to determine fundamental bounds or for analyses using modal methods.

### 2.2.2 T-matrix Method

The T-matrix method [25], also known as the null-field method, is a computational technique used in the frequency domain to solve electromagnetic scattering problems by spherical and compounded non-spherical particles of arbitrary size and surfaces. The basis of the method is the decomposition of the incident and scattered fields into a series of spherical vector wave functions and their matchings using boundary conditions of Maxwell's equations that provide a matrix describing the relationship between these two series, the T-matrix, which contains all information to solve the scattering problem.

The working principles of the T-matrix method are demonstrated on scattering from a PEC obstacle. In such a case, it is necessary to consider the electric field only. The first step is to enclose this object in the smallest possible enveloping sphere. The total electric field on the surface of the scatterer $\partial\Omega$ with an unit normal $\hat{\boldsymbol{v}}$ is then defined by the boundary condition $\hat{\boldsymbol{v}} \times \boldsymbol{E} = \mathbf{0}$, see Figure 2.1, which is satisfied by the introduction of a current density $\boldsymbol{J} = \hat{\boldsymbol{v}} \times \boldsymbol{H}$ on the surface $\partial\Omega$. Utilizing this current, it is possible to express the tangential component of the incident and scattered electric field in their integral form as

$$\begin{aligned} \boldsymbol{E}^{\mathrm{i}}(\boldsymbol{r}) &= \mathrm{j}kZ_0 \int_{\partial\Omega} \mathbf{G}\left(\boldsymbol{r}, \boldsymbol{r}'\right) \cdot \boldsymbol{J}\left(\boldsymbol{r}'\right) \mathrm{d}S', \quad \boldsymbol{r} \quad \text{inside} \quad \partial\Omega, \\ \boldsymbol{E}^{\mathrm{s}}(\boldsymbol{r}) &= -\mathrm{j}kZ_0 \int_{\partial\Omega} \mathbf{G}\left(\boldsymbol{r}, \boldsymbol{r}'\right) \cdot \boldsymbol{J}\left(\boldsymbol{r}'\right) \mathrm{d}S', \quad \boldsymbol{r} \quad \text{outside} \quad \partial\Omega, \end{aligned} \tag{2.7}$$

in which $k$ is the wavenumber, $Z_0$ is free-space impedance, and $\mathbf{G}$ is Green's dyadic [48].

The next step is to express incident and scattered electric fields as a decomposition into spherical vector wave functions so that the incident field is expressed as a weighted sum of regular spherical vector wave functions $\mathbf{u}_n^{(1)}$ and scattered field as a sum of outgoing spherical vector wave functions $\mathbf{u}_n^{(4)}$. The decomposition of the field outside the circumscribed sphere or inside the inscribed sphere can then be written in general as

$$\begin{aligned} \boldsymbol{E}^{\mathrm{i}}(\boldsymbol{r}) &= k\sqrt{Z_0} \sum_n a_n \, \mathbf{u}_n^{(1)}(k\boldsymbol{r}), \\ \boldsymbol{E}^{\mathrm{s}}(\boldsymbol{r}) &= k\sqrt{Z_0} \sum_n f_n \, \mathbf{u}_n^{(4)}(k\boldsymbol{r}), \end{aligned} \tag{2.8}$$

where $a_n$ and $f_n$ are the expansion coefficients. The electric fields from (2.7) can be transformed into a decomposition into spherical vector wave functions of the

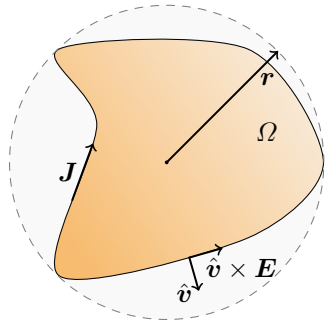


**Figure 2.1:** An object $\Omega$ inside the smallest circumscribing sphere of radius $r$, with the boundary condition imposed on the object's surface.

form (2.8) by substituting the spherical vector waves expansion of Green's dyadic, which results in relations

$$\begin{aligned} \boldsymbol{E}^{\mathrm{i}}(\boldsymbol{r}) &= k^2 Z_0 \sum_{\alpha} \mathbf{u}_{\alpha}^{(1)}(k\boldsymbol{r}) \int_{\Omega} \mathbf{u}_{\alpha}^{(4)}\left(k\boldsymbol{r}'\right) \cdot \boldsymbol{J}\left(\boldsymbol{r}'\right) \mathrm{d}S', \\ \boldsymbol{E}^{\mathrm{s}}(\boldsymbol{r}) &= -k^2 Z_0 \sum_{\alpha} \mathbf{u}_{\alpha}^{(4)}(k\boldsymbol{r}) \int_{\Omega} \mathbf{u}_{\alpha}^{(1)}\left(k\boldsymbol{r}'\right) \cdot \boldsymbol{J}\left(\boldsymbol{r}'\right) \mathrm{d}S'. \end{aligned} \tag{2.9}$$

The last step of the method is to solve the scattering problem, convert it into an algebraic equation, and find the T-matrix. The solution of the problem is then based on known incident field $\boldsymbol{E}^{\mathrm{i}}$, according to the knowledge of which of the coefficients $a_n$ from (2.8) can be determined. In case of surface current density $\boldsymbol{J}$ is replaced by its expansion into a set of basis functions, it is also possible to express this solution in the form of an algebraic equation in which the relation between coefficients $\mathbf{a}$ and $\mathbf{f}$ is represented by the desired T-matrix

$$\mathbf{f} = \mathbf{T}\mathbf{a}. \tag{2.10}$$

When the values of the expansion coefficients $\mathbf{f}$ are found, the scattering problem is solved. An essential product of this method is matrix $\mathbf{T}$ itself, which contains complete information about the scattering properties of the object it represents and is entirely independent of the incident or scattered field. Thus, for a given problem, this matrix can be computed only once and used many times for different definitions of the incident field.

### 2.2.3 Comparison of MoM and T-matrix Method

The MoM and the T-matrix method introduced in the previous sections share some essential properties. Nevertheless, they typically solve electromagnetic problems of different scopes. As such, they are good candidates for hybridization.

Both methods use field integral equations, *i.e.*, they both rely on the knowledge of the system's impulse response (Green's function). Once Green's function is found, the boundary conditions are implicitly considered. Therefore, only the obstacle has to be discretized. One of the outputs of both methods is a system matrix

(impedance matrix, T-matrix), which characterizes a radiation/scattering problem. These matrices can be decomposed, *e.g.*, into modes, or can be used to investigate fundamental bounds. These techniques assist with effective antenna analysis and design and are introduced later.

The different ways these methods solve the scattering problem predetermine their properties. MoM relies on determining a surface current density that typically employs piece-wise basis functions. They effectively describe arbitrarily shaped objects; however, they require adopting a discretization scheme and powerful algorithms capable of inverting large algebraic systems. In contrast, the T-matrix method uses entire domain basis functions to represent incident and scattered fields. Their use is straightforward for regular obstacles only. Entire domain basis functions limit the possibility of defining discrete sources, common for problems solved by MoM. It is obvious that if the methods are to coexist, it is necessary to find a relationship between the used bases.

The properties described above show that neither of these methods is universal and that it is possible to find scenarios in which one method dominates. However, since many of their properties are complementary, it would be advantageous to combine them together. Such a hybrid method has wide applicability across computational electromagnetism. For example, a scenario with two interacting objects, such as a fed antenna of a complex shape and a large passive scatterer placed nearby, is a challenging problem when both methods are used separately but an easy task for the hybrid method. To this purpose, an interaction operator between the objects has to be derived, and the system matrix has to be assembled from the blocks describing individual objects and their interaction represented in different bases, *i.e.*, utilizing either MoM or the T-matrix. Even so, the method retains all features typical of a solution of an integral equation, *e.g.*, the system matrix is dense, and it is possible to apply a modal decomposition to it or to search for fundamental bounds using it.

## 2.3 Modal Analysis

Modal analysis provides detailed information regarding the dynamic properties of a system in various engineering fields, including structural mechanics [49], quantum mechanics [50], acoustics [51], and electromagnetism [52] This is achieved by the diagonalization of the studied linear operator associated with determining eigenvalues and eigenvectors. In most cases, the decomposition cannot be done analytically, *i.e.*, the problem has to be expressed in its algebraic form. This can be done using suitable numerical methods such as MoM or the T-matrix method, described above, or the finite element method. The modal decomposition is then implemented by solving a generalized eigenvalue problem which can be written as

$$\mathbf{A}\mathbf{x}_n = \lambda_n \mathbf{B}\mathbf{x}_n, \tag{2.11}$$

in which $\mathbf{A}$ and $\mathbf{B}$ are matrices representing the linear operators, and $\lambda_n$ is an eigenvalue corresponding to eigenvector $\mathbf{x}_n$. Several numerical routines are available to solve the eigenvalue problem effectively. For example, the implicitly restarted Arnoldi method [53]. The result is a set of modes representing the principle solution of a given system, *i.e.*, such solutions whose reinsertion into the system yields the same mode just linearly scaled by the corresponding eigenvalue. This behavior is illustrated in Figure 2.2.

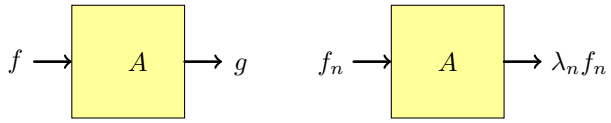


**Figure 2.2:** Visual representation of the different behavior of operator $A$ when applied to a general function (left) and its eigenfunction (right).

Depending on the particular engineering problem, there is practically an infinite number of choices of matrices $\mathbf{A}$ and $\mathbf{B}$ in (2.11). The following decompositions are common to radiation problems in electromagnetism:

- natural modes [32, 54],
- characteristic modes [9],
- radiation efficiency modes [16, 55],
- stored energy modes [56],
- directivity modes [57],
- "Loop-Star" modes [58].

### 2.3.1 Characteristic Modes

The eigenmodes of the transition and scattering matrices form the bases of the CMs that have been very popular in the field of antenna studies in recent years. The history of this modal analysis goes back to the 1960s when characteristic modes were introduced by Garbacz [8, 59] who wanted to find a basis representing a field scattered by an obstacle.

To derive these modes, Garbacz used the diagonalization of the T-matrix (perturbation operator), which defines the relationship between the regular and outgoing spherical waves. The decomposition can be written as an eigenvalue problem

$$\mathbf{T}\mathbf{f}_n = t_n \mathbf{f}_n, \tag{2.12}$$

where $\mathbf{f}_n$ is a characteristic vector containing coefficients of outgoing spherical waves, and $t_n$ is the corresponding characteristic value.

The work of Garbacz was followed up by Harrington and Mautz [9] who employed MoM for perfect conductors and formulated a generalized eigenvalue problem (GEP) as

$$\mathbf{Z}\mathbf{I}_n = (1 + \mathrm{j}\lambda_n)\,\mathbf{R}\mathbf{I}_n, \tag{2.13}$$

in which $\mathbf{Z} = \mathbf{R} + \mathrm{j}\mathbf{X}$ is impedance matrix. A characteristic basis is found by solving this GEP. It is seen in (2.13) that the decomposition diagonalizes the impedance matrix.

No excitation is considered in (2.12) and (2.13). If the excitation is given, the characteristic modes add up, leading to the solution given by (2.6).

The comparison of (2.12) and (2.13) shows that Garbacz's and Harrington's definitions of characteristic modes are visually different. This raises the question of how the two definitions are related. Harrington hypothesized their mutual relationship without going into much detail [9]. Their relationship has only recently been rigorously demonstrated in [60*] and then elaborated in detail in [61].

The key step to establishing the relationship between formulations based on the T-matrix, (2.12), and impedance matrix, (2.13), is to find the projection between the entire-domain basis of spherical waves (in which the T-matrix is represented) and a local basis (in which the impedance matrix is represented). This projection can be defined using the expansion of Green's dyadic function into spherical waves [48] as

$$\mathbf{U}_1 = k\sqrt{Z}\int_{\Omega} \mathbf{u}_n^{(1)}\left(k\boldsymbol{r}\right)\cdot\boldsymbol{\psi}_i\left(\boldsymbol{r}\right)\mathrm{d}V, \tag{2.14}$$

where $\mathbf{u}_n^{(1)}$ are real-valued spherical waves and $\boldsymbol{\psi}_i\left(\boldsymbol{r}\right)$ are the local basis functions, *e.g.*, RWG basis functions. By comparing (2.8) and (2.9) for the scattered field using the knowledge of projector $\mathbf{U}_1$, it is possible to write the algebraic relationship between the expansion coefficients in both bases as

$$\mathbf{f}_n = -\mathbf{U}_1\mathbf{I}_n. \tag{2.15}$$

Similarly, it is possible to express the incident field through regular spherical waves. Assuming that the sources are located outside the minimum circumscribed sphere, it is possible to write

$$\mathbf{V} = \mathbf{U}_1^{\mathrm{T}}\mathbf{a}_n. \tag{2.16}$$

By substituting (2.15) and (2.16) into (2.6) is possible to obtain the relation between the impedance matrix $\mathbf{Z}$ and T-matrix $\mathbf{T}$ as

$$\mathbf{T} = -\mathbf{U}_1\mathbf{Z}^{-1}\mathbf{U}_1^{\mathrm{T}}, \tag{2.17}$$

and by (2.6) and using the relation (2.10), the relation between the eigenvalues of both CM decompositions is found as

$$t_n = -\frac{1}{1+\mathrm{j}\lambda_n}. \tag{2.18}$$

The decomposition of the T-matrix (2.12) and impedance matrix (2.13) are equivalent and lead to the same modes, only represented in different bases. In both cases, the decomposition forms a basis of orthogonal vectors

$$\frac{1}{2}\mathbf{I}_n^{\mathrm{H}}\mathbf{R}\mathbf{I}_m = \frac{1}{2}\mathbf{f}_n^{\mathrm{H}}\mathbf{f}_m = P_n^{\mathrm{rad}}\delta_{nm}, \tag{2.19}$$

where $P_n^{\mathrm{rad}}$ is the cycle mean power radiated by the n-th mode, superscript $^{\mathrm{H}}$ refers to complex conjugation, and $\delta_{nm}$ is the Kronecker delta [62].

The Rayleigh quotient is given by characteristic number $\lambda_n$ and is proportional to the ratio between reactive and radiated power

$$\lambda_n = \frac{2\omega\left(W_n^{\mathrm{m}} - W_n^{\mathrm{e}}\right)}{P_n^{\mathrm{rad}}} \approx -\frac{\mathrm{Im}\{t_n\}}{\mathrm{Re}\{t_n\}} = \frac{\mathbf{I}_n^{\mathrm{H}}\mathbf{X}\mathbf{I}_n}{\mathbf{I}_n^{\mathrm{H}}\mathbf{R}\mathbf{I}_n}, \tag{2.20}$$

in which $W_n^{\mathrm{m}}$ and $W_n^{\mathrm{m}}$ stand for electric and magnetic stored energy of the $n$-th characteristic mode. Three states are distinguished depending on the value of $\lambda_n$: a negative value indicates the capacitive behavior of a given mode, a positive value refers to inductive behavior, and if the value is zero, the mode is in a resonance state. The magnitude of the eigenvalue can grow beyond all limits if the value of

the radiated power is close to zero, $\lambda_n \in (-\infty, \infty)$. In contrast, the magnitude of eigenvalues $t_n$ is limited, so they all lie on a circle in the complex plane.

The method of characteristic modes has two essential features. First, no excitation is assumed, therefore, the characteristic currents provide radiation properties of an obstacle, depending solely on the scatterer's geometry (and frequency). The second advantage is a sparsity of the characteristic basis, *i.e.*, that only a few characteristic modes are sufficient to describe the far-field characteristics of a small object. As such, it can be applied to reduce the computational burden of many problems, such as performing feeding synthesis [63] or evaluation of fundamental bounds [64].

Commercial software implements the characteristic modes evaluation to decompose an impedance matrix only [65, 66]. While straightforward and easy to implement, it has some known issues depending on the particular integral equation used: there can be internal resonances for closed obstacles, spurious modes can occur, or the modes can appear and disappear thanks to poor meshing and finite numerical precision. Significant challenges arise when attempting to study material bodies using the impedance-matrix-based approach. In such cases, employing formulations like PMCHWT [67] becomes necessary, leading to modifications in the process of obtaining characteristic modes [68]. Scattering formulations utilizing the T-matrix [25] or scattering dyadic [48] eliminate these deficiencies.

A few drawbacks cannot be mitigated by any means since they are directly related to the definition of CMs. The first follows directly from the definition of CMs, according to which CM basis is orthogonal in the far field. Thus, this basis can represent the near-field only outside the circumscribing sphere, see Fig. 2.1. The second problem is related to the post-processing method referred to as modal tracking. This method is used when looking for an answer to the question *"How does the given characteristic mode evolve with a change in frequency?"* To find the answer, it is necessary to obtain the sets of characteristic modes at different frequencies and use the tracking algorithm to find the corresponding modes across the sets. For these purposes, several algorithms have been developed using, *e.g.*, correlations between current densities [69, 70], correlations between radiation diagrams [70, 71], or the determination of crossing avoidances based on the von Neumann-Wiegner theorem [72].

## 2.4 Validation of Characteristic Mode Solvers

In the field of any numerical simulation, numerical solver accuracy, efficiency, and scalability are crucial for obtaining meaningful results. The validation of electromagnetic numerical solvers involves comparing the results of simulations with available experimental data or analytical solutions.

The Institute of Electrical and Electronics Engineers (IEEE) has established standards for validating electromagnetic (EM) solvers and providing a benchmark for assessing their performance. IEEE Std 1597.1-2008, "Standard for Validation of Computational Electromagnetics Computer Modeling and Simulations," [73] and IEEE Std 1597.2-2010, "Recommended Practice for Validation of Computational Electromagnetics Computer Modeling and Simulations," [74] are widely recognized standards for the validation of EM solvers. These standards provide a comprehensive framework for verifying and validating EM solvers, including guidelines for conducting validation studies, evaluating results, and reporting results in a standardized manner.

An important aspect of the validation is choosing a suitable test case. In this regard, a spherical shell of homogeneous material can be an ideal candidate because of its well-defined and analytically tractable geometry. This allows for a comparison between the simulation results and analytical solutions while accounting for errors in the model, discretization, numerical precision, etc.[31].

Contemporary CM solvers, predominantly based on EFIE and MoM, are known to suffer from several imperfections, which should be systematically studied:

- Errors in the model: The characteristic mode solver's accuracy depends on the geometry and material models used in the simulation. Improper modeling of the structure can lead to inaccurate results.
- Singularity treatment: Evaluation of the impedance matrix can encounter singularities, points, or regions in the structure where the solution becomes undefined. When calculating the impedance matrix, these points must be treated correctly.
- Numerical instability: CM solvers can be subject to numerical instabilities, especially when the impedance matrix is ill-conditioned or singular. This can result in inaccurate results and convergence issues.
- Finite numerical precision: The limited precision of digital computers can result in numerical errors and instability in the simulation results, particularly when dealing with large matrices that can be ill-conditioned and sensitive to numerical errors.
- Quality of modal tracking: Incorrect modal tracking may lead to a misinterpretation of the modal data and cause difficulties in efficient antenna design.

With all the challenges associated with CM analysis, it is essential to ask how precise the results are. This highlights the importance of validating CM solvers, which involves comparing the results of simulations with known benchmark solutions and experimental data when available. Systematic benchmarking and validation help to identify potential sources of error and ensure the accuracy and reliability of the simulation results, as it was studied in detail in [75*], and some of the findings were addressed in [76*]. By improving CM solver precision, complex structures' behavior can be better understood, leading to more accurate predictions and improved performance. Therefore, investing in the validation of CM solvers can result in significant benefits, both in terms of the accuracy of the simulation results and the potential impact on practical applications.

## 2.5 Fundamental Bounds

Fundamental bounds are limits that certain physical quantities or systems cannot exceed. These bounds are often set by the laws of physics and are seen as fundamental principles that govern the behavior of the universe. Examples of fundamental bounds include the speed of light [77], the uncertainty principle [78], and Shannon's channel capacity [79]. Understanding these bounds is crucial for developing new theories and technologies. In electromagnetism, a fundamental bound on a given parameter is understood as a performance of a hypothesized optimal device, represented by a circuit, electromagnetic field, or an optimal current density distribution. The fundamental bound provides a useful benchmark for the design and performance evaluation of realized devices. By understanding the limitations imposed by the fundamental bounds, engineers and designers can strive to design antennas that

approach this theoretical limit while considering other factors such as cost, complexity, and practical constraints.

The beginnings of fundamental bounds in antenna engineering are connected with studies on the upper bound on antenna bandwidth. This topic was studied by Chu [80], who, using a circuit model, found the optimal solution as a decomposition into spherical waves [81] outside the sphere surrounding the antenna. With this, he showed that it is possible to approximate the lower bound of the Q-factor (upper bound on the bandwidth) as a sole function of electric size. Chu's approach was further extended by Thal [82, 83] who modified the equivalent circuit to include the electromagnetic field inside the region of the sphere.

The fundamental bounds presented by Chu were derived only for spherically shaped objects. However, the objective was to find the fundamental bounds of arbitrarily shaped bodies. To achieve this goal, the way to determine the Q-factor had first to be discovered [84]. The method is based on Poynting's complex theorem [85] and the method of subtraction of the radiated power associated with the radial part of Poynting's vector. This technique was later further extended in [86, 87].

Another generalization in determining fundamental limits was the transition from field quantities to source quantities, *i.e.*, currents. The Q-factor is expressed in terms of currents as the ratio of the stored energy and radiated power (this expression merges with the relation for characteristic values $\lambda_n$ in the form of Rayleigh's quotient) in [88, 89] and later extended by using different ways of calculating the field energy in [90–92]. The first formulation of the relation for the Q-factor into matrix form, using products of MoM, impedance matrix, and current expansion coefficients, paved the way for the application of convex optimization [93] for the determination of fundamental bounds [12].

Since then, many antenna parameters were treated analogously, *e.g.*, antenna gain, or directivity. However, the works on radiation efficiency limits are scarce [94]. Those that have addressed this topic have used various methods, such as the expansion into spherical waves [95, 96] and recently in [97*], convex optimization [98, 99], modal methods [100, 101], or Chu's equivalent circuits [102, 103].

In recent years, the matrix representation of various antenna parameters in quadratic forms has been widely used in optimization problems written as quadratically constrained quadratic programs (QCQPs). Lagrange duality and modal analysis are two effective techniques that can simplify the solution of these QCQPs. The original problem is transformed into a dual problem in Lagrange duality by introducing Lagrange multipliers for the constraints [93]. The dual problem is always convex and provides an upper bound for the original (primal) problem that can be more computationally tractable and can be used to obtain information about the optimal solution. As long as the dual gap is zero, a solution to the dual problem yields a solution to the primal problem.

In modal analysis, the optimization problem is transformed into a lower-dimensional subspace defined by the eigenmodes of a relevant matrix. By representing the problem in eigenspace, the size of the problem can be reduced, and the quadratic forms can be simplified. When combined with Lagrange duality, modal analysis can further improve the computational efficiency and accuracy of the solutions obtained when solving QCQPs. Moreover, with modal decomposition, chosen quadratic forms are diagonalized, which greatly simplifies the problem formulation and numerical operations, such as matrix inversion. An extreme example is the spherical shell, where all quadratic forms are diagonalizable simultaneously.

As there are effective ways to determine fundamental bounds, which have recently received a lot of attention, a large number of papers have been published dealing

with finding single-criteria bounds for various antenna parameters, as well as the multi-criteria fundamental bounds combining more parameters together, such as:

- maximizing antenna directivity and gain [28, 57],
- minimizing antenna Q-factor [104, 105],
- maximizing antenna radiation efficiency [101, 106], and
- extremism of value of multi-criteria parameters [42, 107, 108].

The fundamental bounds are not just a theoretical exercise but have a real impact on antenna design. Even though they cannot directly tell what the optimal antenna should look like, they can provide valuable information about how far away a given design is from the optimum. Thus, it has been shown that several antenna designs lie close to the optimum [105, 109–113].

## 2.6 Thesis Objectives

The main objectives of the thesis are defined as follows:

1. To formulate an analytical solution of characteristic modes for a spherical shell to benchmark existent numerical solvers and to get a close-form solution for further tests.
2. To derive and verify the upper bound on radiation efficiency for a spherical shell in closed form, compare it with a numerical solution and investigate the surface resistivity model's validity.
3. To derive and implement a projection operator between method-of-moments' piece-wise basis functions and spherical waves, and use this operator to improve the precision of characteristic mode decomposition.
4. To combine spherical wave expansion and method of moments in a hybrid method utilizing both entire-domain and piece-wise basis functions.
5. To create a comprehensive MATLAB [114] package containing a set of functions aimed at consolidating the knowledge presented in published research papers on spherical functions and their application to calculate electromagnetic quantities.

# 3 Thesis Solutions

## 3.1 Analytical Representation of Characteristic Mode Decomposition

- M. Capek, P. Hazdra, M. Masek, and **V. Losenicky**, "Analytical Representation of Characteristic Mode Decomposition," *IEEE Transactions on Antennas and Propagation*, vol. 65, no. 2, pp. 713–720, Feb. 2017, DOI: 10.1109/TAP.2016.2632725.

This paper deals with various aspects of the characteristic mode analysis. An analytical functional for the characteristic mode decomposition and associated eigenvalue problem are defined in this paper. Based on this representation, it is possible to design approximate analytical prescriptions of current distribution for particular, yet canonical, obstacles such as a dipole, a loop, or a cylinder. The Rayleigh quotient is used to compare the similarity of current distributions with the numerical full-wave solutions.

Finding analytical formulas for current distributions is a starting point for several studies dealing with antenna analysis and design issues, such as the ability to benchmark MoM and CM solvers or to explain the ability of inductive modes to resonate. For these purposes, three canonical examples are presented for which analytical formulations are found: a thin dipole (see Figure 3.1), two parallel dipoles, and a loop (cylinder). It is also identified that when properly normalized, a spherical shell, whose characteristic fields are equivalent to spherical harmonics, is the most suitable candidate for benchmarking purposes. In addition, the Q-factor analysis of the cylinder revealed that applying the common method for its evaluation [115] provides negative Q values. On this account, the prescription for the Q-factor was enriched with a new term that establishes a link between the frequency behavior of eigenvalues and the modal stored energies.

The paper also opens up the idea of verifying available characteristic modes solvers and their particular parts based on known analytical prescriptions of characteristic modes for the spherical shell.

The paper is reprinted in Appendix A.

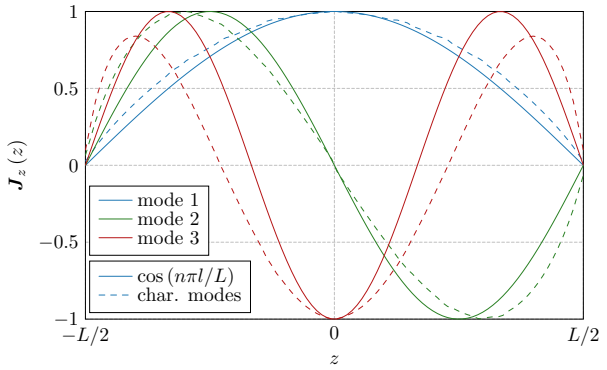


**Figure 3.1:** Numerically determined current distributions of a thin strip dipole's first three characteristic modes with a length-to-width ratio of 100 compared with corresponding sine approximations.

## 3.2 Validating the Characteristic Modes Solvers

- M. Capek, **V. Losenicky**, L. Jelinek, and M. Gustafsson, "Validating the Characteristic Modes Solvers," *IEEE Transactions on Antennas and Propagation*, vol. 65, no. 8, pp. 4134–4145, Aug. 2017, DOI: `10.1109/TAP.2017.2708094`.

This paper is a follow-up to the paper in Appendix A and elaborates on the systematical validation of the CM decomposition routinely performed in software packages. The validation is based on the knowledge of the analytical prescription for the radiation quantities of a given object and their subsequent comparison with results coming from the numerical solution. As has already been stated in Appendix A, a possible candidate for this use is a spherical shell whose CMs (see Figure 3.2) match with spherical harmonics when scaled correctly. Despite its geometrical simplicity, a spherical shell provides a rich testing scenario with convenient properties, *e.g.*, it contains degenerated modes and internal resonances, the geometry does not conform with triangular mesh, and the number of significant modes rapidly increases with electrical size.

Based on the analytical prescription of CMs, several test cases focus on different aspects of the modal analysis. These include the accuracy of determining the eigenvalues and eigenvectors (characteristic currents), verification of modal tracking, or comparison of characteristic far-fields. These tests are applied to several commercial in-house packages, and their results are presented in the paper.

It was shown that all tested packages deliver comparable results when determining the characteristic modes for a given frequency. The main limiting factor was shown to be (finite) numerical precision. In the case of modal tracking, however, some packages produce unsatisfactory results.

The results stimulated broader activity within the community [116, 117].

The paper is reprinted in Appendix B.

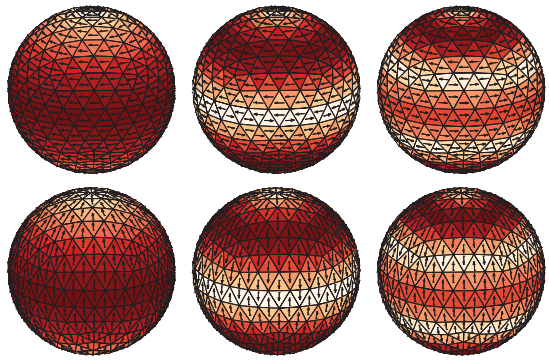

**Figure 3.2:** Current densities of the first three (with the lowest magnitude of characteristic number) inductive and capacitive characteristic modes of a spherical shell.

## 3.3 Dissipation Factors of Spherical Current Modes on Multiple Spherical Layers

- **V. Losenicky**, L. Jelinek, M. Capek, and M. Gustafsson, "Dissipation Factors of Spherical Current Modes on Multiple Spherical Layers," *IEEE Transactions on Antennas and Propagation*, vol. 66, no. 9, pp. 4948–4952, Sept. 2018, DOI: 10.1109/TAP.2018.2841408.

The spherical shell is commonly used to evaluate the fundamental limits for various electromagnetic metrics because it is an analytically tractable object. Its symmetricity allows for the simultaneous diagonalization of all physical operators [118]. This helps to assess the precision and stability of numerical techniques which are, afterward, used for dealing with arbitrarily shaped obstacles [119, 120]. The same approach is applied in this paper which focuses on determining the fundamental bounds of radiation efficiency. Maximizing radiation efficiency is achieved by minimizing the ratio between lost and radiated power, referred to as the dissipation factor, which provides considerable advantages for optimization purposes because it allows for the removal of the dependence on surface resistivity, and its optimization leads directly to the solution of the generalized eigenvalue problem.

One way to obtain current distributions reaching the fundamental bound on dissipation factor or radiation efficiency is to combine suitable spherical harmonics that coincide with characteristic modes in the case of the spherical shell. The optimal composition of spherical harmonics is uniquely given (except for degeneracies existing due to spherical shell symmetries) and includes properly weighted dominant TM and TE modes. These modes have the lowest modal dissipation factors and enforce self-resonance.

The scenario with one spherical shell can be further generalized by adding more spherical layers concentric with the original layer, see the illustration in Figure 3.3, thus achieving lower dissipation factor values. The reduction of the dissipation factor can be continued by gradually adding additional concentric layers, indicating that the volumetric current distribution is favorable regarding radiation efficiency [107].

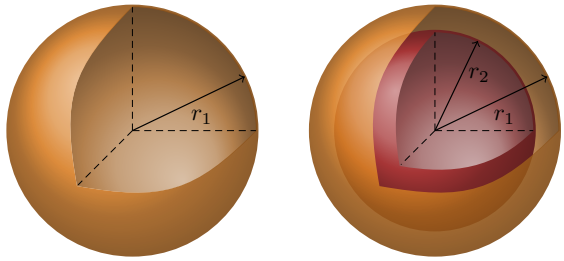


**Figure 3.3:** Illustration of a spherical shell and two concentric spherical shells which are used in determining the fundamental limits on the radiation efficiency.

The paper is reprinted in Appendix C.

## 3.4 Accurate and Efficient Evaluation of Characteristic Modes

- D. Tayli, M. Capek, L. Akrou, **V. Losenicky**, L. Jelinek, and M. Gustafsson, "Accurate and Efficient Evaluation of Characteristic Modes," *IEEE Transactions on Antennas and Propagation*, vol. 66, no. 12, pp. 7066–7075, Dec. 2018, DOI: `10.1109/TAP.2018.2869642`.

This paper builds on Section 3.2, which identified that one of the challenges of CM analysis is the low-rank nature of the radiation part of the impedance matrix, which notably restricts the number of significant CMs and their precision. The issue is addressed through two distinct approaches. The first involves an alternative methodology for determining the radiating part of the impedance matrix. The second approach capitalizes on the fact that most real-world electromagnetic problems converted to a discrete model have more degrees of freedom than the feasible number of modes obtainable via modal analysis. Consequently, it proves advantageous to initially transform the task to be represented by smaller matrices, reducing its degrees of freedom, before proceeding with the decomposition process. This transformation makes the computational task well-defined and greatly speeds up its evaluation.

To remedy the numerical issues related to the properties of the radiation matrix, the paper focuses on its analytical factorization. The study shows another way of constructing the radiation matrix using the spherical wave expansion of the dyadic Green's function, which allows factorizing the radiation matrix into the product of projection matrices. These projection matrices define the relationship between two distinct bases, the basis used in evaluating MoM and the basis of spherical vector waves, which can be used to provide the interaction between two distinct objects described in these two different bases. The relationship of these two bases is demonstrated in Figure 3.4.

The factorized radiation matrix allows us to define an alternative way of calculating CMs, reduce computational complexity, and offer significantly higher numerical dynamics compared to the classical GEP.

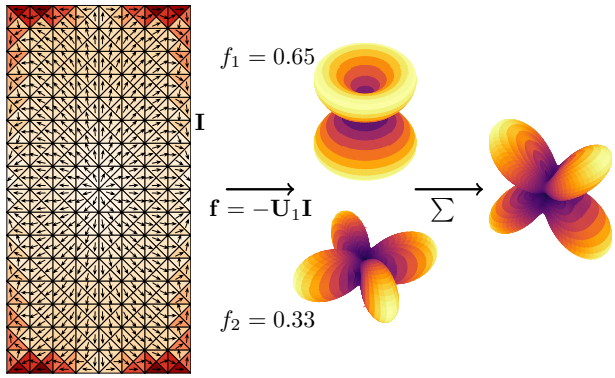


**Figure 3.4:** Projection of a characteristic mode onto the basis of spherical harmonics. Projection matrix $\mathbf{U}_1$ transforms current density $\mathbf{I}$ into the coefficients of spherical waves (only two waves whose coefficients have the largest magnitude are shown), which are then summed to obtain the total radiation diagram.

The paper is reprinted in Appendix D.

## 3.5 Method of Moments and T-matrix Hybrid

- **V. Losenicky**, L. Jelinek, M. Capek, and M. Gustafsson, "Method of Moments and T-matrix Hybrid," *IEEE Transactions on Antennas and Propagation*, vol. 70, no. 5, pp. 3560–3574, May 2022, DOI: 10.1109/TAP.2021.3138265.

This paper introduces a hybrid computational scheme combining the MoM formulation of EFIE and the T-matrix method. Such a scheme efficiently models the interaction between an electrically small arbitrarily-shaped radiator and an electrically large passive object. The method excels in cases when the large object is of canonical shape.

The hybrid method combines the advantages of both methods: a precise description of the small radiator by MoM and a compact representation of a large neighboring object by the T-matrix. The projection operator formulated in Section 3.4 is used to couple MoM and T-matrix descriptions. A by-product of the method development is a simple formula to determine the T-matrix from the impedance matrix of an arbitrarily shaped object, which can be utilized for CM decomposition with favorable properties as illustrated by Figure 3.5.

The study presents the definition of the method supported by several examples illustrating its performance, *e.g.*, an analysis of the interaction of an antenna and passive object in case the antenna is located interior or exterior of the passive object. All these examples are verified by a solution performed in a commercial computational tool.

The paper on the hybridization of MoM and the T-matrix method is reprinted in Appendix E. Recently, the findings published in this paper have gained further attention in [121] in which the original idea is expanded by the application of a general scattering matrix instead of an impedance matrix.

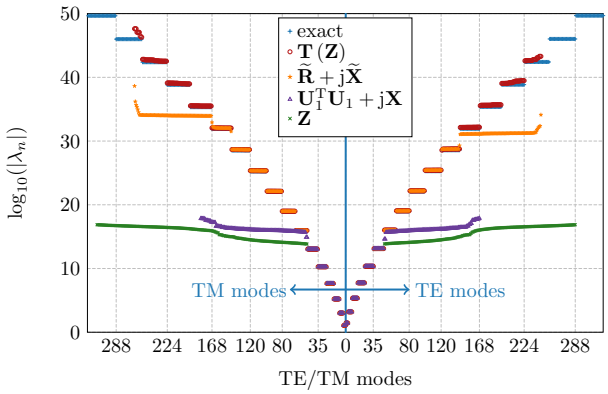


**Figure 3.5:** Comparison of the characteristic numbers of a spherical shell of electrical size $ka = 0.5$, which are determined using all available methods that have been used in Appendices A–E. The values determined by the various numerical methods are compared with the exact values based on the analytical formulae for the eigenvalues of a spherical shell.

## 3.6 Package of Spherical Functions

The aforementioned papers use the spherical functions and waves as an analytical tool. One of the results of this thesis is their implementation as a MATLAB package. This package, integrated into AToM (Antenna Toolbox for Matlab) [122], has found applications in both academia and engineering and has proven to be a versatile tool for a variety of tasks, *e.g.*, [61, 123–125].

An original set of several functions used in Appendix D has evolved into a powerful MATLAB package which was significantly expanded in connection with the publication of AppendixE and contains, *e.g.*, transformation of impedance matrices to T-matrices, functions combining T-matrices (useful for complex scattering systems), or a code for the efficient calculation of the properties of multilayered multi-material spheres. The package can calculate the projection matrix between spherical waves and piece-wise (RWG) basis functions.

# 4 Conclusion

The thesis has extensively studied the properties of characteristic modes in both their analytical and numerical forms. The analytical representation of characteristic modes for a spherical shell was utilized to develop a systematic approach to validate various aspects of characteristic mode decomposition and identify its weaknesses. Applying this benchmark procedure to commercial solvers provides important feedback regarding further software improvement.

The properties of the characteristic modes of a spherical shell, together with the validation findings, have been utilized to introduce a projection matrix relating spherical waves with basis functions used in the method of moments. This matrix allowed us to define a more accurate and efficient approach to determining characteristic modes. This advancement in computational methodology enhances the precision of the results and reduces computational time. It is also shown that the proposed projection matrix can be used in several other places, such as in determining the positive semidefinite radiation part of the impedance matrix or the evaluation of a T-matrix from an impedance matrix.

The above-mentioned matrix was further used to define a hybrid computational method combining the method of moments and the T-matrix method. It was shown that such a method has excellent properties for analyzing the interaction of a small radiator with its surroundings. Last but not least, the spherical projection matrix plays a crucial role in connecting scattering and impedance definition of characteristic modes.

The presented thesis also studied the fundamental bounds of radiation efficiency. The analytical definition of characteristic modes has been used to show that the maximum efficiency favors volume current distributions instead of surfaces.

## 4.1 Future Work

The following themes represent future work directions raised from this thesis:

1. The hybrid method can address today's specific challenges, such as antennas implanted in the human body.
2. Another topic is the generalization of the hybrid method. Currently, the method describes the relationship between one radiator and one passive object or two radiators that can be separated by a plane. Nevertheless, it is possible to consider any number of passive and active objects.

3. The impedance matrix is an important ingredient in determining fundamental limits. Since there is a relationship between the impedance matrix and the T-matrix, applying the T-matrix to determine the fundamental bounds could reduce complexity and speed up these calculations.
4. The decomposition into characteristic modes formulated using the T-matrix detached this technique from integral equations and method of moments. This allows the study of characteristic modes using generic electromagnetic solvers and opens a way to characteristic decompositions of scenarios with complex materials. Similarly, the hybrid method can be used to define substructure characteristic modes, greatly reducing the computational burden.

# A Analytical Representation of Characteristic Modes Decomposition

**Published as:** M. Capek, P. Hazdra, M. Masek, and **V. Losenicky**, "Analytical Representation of Characteristic Mode Decomposition," *IEEE Transactions on Antennas and Propagation*, vol. 65, no. 2, pp. 713–720, Feb. 2017, DOI: 10.1109/TAP.2016.2632725.

**Abstract**— Aspects of the theory of characteristic modes, based on their variational formulation, are presented and an explicit form of a related functional, involving only currents in a spatial domain, is derived. The new formulation leads to deeper insight into the modal behavior of radiating structures as demonstrated by a detailed analysis of three canonical structures: a dipole, an array of two dipoles and a loop, cylinder and a sphere. It is demonstrated that knowledge of the analytical functional can be utilized to solve important problems related to the theory of characteristic modes decomposition such as the resonance of inductive modes or the benchmarking of method of moments code.

**Index terms:** Antenna theory, eigenvalues and eigenfunctions, electromagnetic theory.

## A.1 Introduction

The theory of characteristic modes (CMs), formally developed by Garbacz [8] and Harrington and Mautz [9], has become very popular in recent years as this theory constitutes a general approach to characterizing the modal resonant behavior of arbitrarily shaped antennas and scatterers [10]. In its original form, which is considered here, the CM assumes perfect electric conductors (PEC) in a vacuum. Academic interest and a number of publications dealing with CMs continue to grow. However, most papers focus only on the application character, such as [126–128]. Excluding the first attempt to summarize CMs in a book [29], there are also related chapters to be found in older books [129] and [130].

This paper briefly reviews characteristic mode decomposition and what constitutes the necessary theoretical background. An analytical form of the functional, composed of reactive and radiated power, is derived, based on previous research [91], [131]. This relation has to be satisfied for each mode but is not restricted to the

characteristic basis. Hence, it is possible to specify arbitrary current distribution (the CM can be predicted, see [132]) and compare it with real CMs. Based on this result, properties of canonical shapes are investigated, including inductive modes. Analogically, if the modes are analytically known, they can be substituted into a derived functional instead of using an approximative solution given by the numerical spectral decomposition of an underlying operator.

## A.2 Derivation of the functional

Based on previous work by Garbacz [8], Harrington [9] reduced the CMs into the following generalized eigenvalue problem (GEP, [133])

$$\mathcal{X}\left(\boldsymbol{J}_n\right) = \lambda_n \mathcal{R}\left(\boldsymbol{J}_n\right), \tag{A.1}$$

where $\mathcal{R}$ and $\mathcal{X}$ are real and symmetric operators forming the impedance operator

$$\mathcal{Z}\left(\boldsymbol{J}_n\right) = \mathcal{R}\left(\boldsymbol{J}_n\right) + \mathrm{j}\mathcal{X}\left(\boldsymbol{J}_n\right) = \boldsymbol{n}_0 \times \left(\mathrm{j}\omega \boldsymbol{A} + \nabla\phi\right), \tag{A.2}$$

$\boldsymbol{A}$ and $\phi$ are corresponding magnetic and electric time-harmonic potentials in Lorenz gauge [85], $\boldsymbol{J}_n$ is the modal current density, and $\boldsymbol{n}_0$ is the unit vector tangential to the PEC boundary of a radiator. The continuous operator $\mathcal{Z}$ is usually discretised by the method of moments (MoM, [24]), utilizing a proper set of basis functions

$$\boldsymbol{J}_n\left(\boldsymbol{r}\right) \approx \sum_{m=1}^{N} I_{mn} \boldsymbol{f}_m\left(\boldsymbol{r}\right), \tag{A.3}$$

where $I_{mn}$ are (modal) expansion coefficients and $\boldsymbol{f}_m\left(\boldsymbol{r}\right)$ are frequency-independent basis functions, e.g., RWG basis functions [44]. Consequently, the MoM procedure leads to an impedance matrix $\mathbf{Z} = \mathbf{R} + \mathrm{j}\mathbf{X}$, which is the discrete representation of the analytical operator $\mathcal{Z}$. Finally, the CMs can be defined in (common) algebraic form [9]

$$\mathbf{X}\mathbf{I}_n = \lambda_n \mathbf{R}\mathbf{I}_n, \tag{A.4}$$

which is, in comparison to (A.1), numerically solvable for an arbitrary radiator since it is based on real and symmetric matrices of size $N \times N$, where $N$ is the number of basis functions.

The solution of the GEP produces the characteristic basis $\{\boldsymbol{J}_n, \lambda_n\}$ of eigencurrents $\boldsymbol{J}_n$ and associated eigenvalues $\lambda_n$ and, due to the properties of the impedance matrix, all eigenvalues are real with all eigencurrents equiphasal (they can also be selected as real, [134]). Furthermore, the CMs minimize the ratio of the net reactive power $\omega\left(\mathbf{W} - W_\mathrm{e}\right)$ to radiated power $P_\mathrm{rad}$. Note that the extremal value of radiated to stored power is considered for the basis as a whole.

It is known [29] that the GEP (A.1) minimizes a power functional[1]

$$\mathcal{F}\left(\boldsymbol{J}_n\right) = \frac{\langle \boldsymbol{J}_n, \mathcal{X}\boldsymbol{J}_n \rangle}{\langle \boldsymbol{J}_n, \mathcal{R}\boldsymbol{J}_n \rangle} = \frac{2\omega(W_\mathrm{m}^n - W_\mathrm{e}^n)}{P_\mathrm{r}^n} = \lambda_n, \tag{A.5}$$

[1]Through this paper, the following notation is used $\langle \boldsymbol{f}, \boldsymbol{g} \rangle = \int_\Omega \boldsymbol{f}^* \cdot \boldsymbol{g} \ \mathrm{d}\Omega$ and $\langle \boldsymbol{f}, \boldsymbol{g} \rangle_\mathrm{r} = \int_\Omega \boldsymbol{f} \cdot \boldsymbol{g} \ \mathrm{d}\Omega$.

where $W_{\mathrm{m}}^n$ and $W_{\mathrm{e}}^n$ are modal magnetic and electric potentials-based energies, defined here as

$$W_{\mathrm{m}}^n = \frac{1}{2}\,\mathrm{Re}\int\limits_V \boldsymbol{A}\cdot\boldsymbol{J}_n^*\,\mathrm{d}V, \tag{A.6}$$

$$W_{\mathrm{e}}^n = \frac{1}{2}\,\mathrm{Re}\int\limits_V \varphi\rho_n^*\,\mathrm{d}V, \tag{A.7}$$

with $P_{\mathrm{r}}^n$ as modal radiated power which is commonly normalized as $P_{\mathrm{r}}^n = 1\,\mathrm{W}$. It should be noted that energies (A.6) and (A.7) are not equal to true electric ($\int_V \epsilon\|\boldsymbol{E}\|^2\,\mathrm{d}V/2$) and magnetic ($\int_V \mu\|\boldsymbol{H}\|^2\,\mathrm{d}V/2$) energy [135]. However, a clear advantage of (A.6) and (A.7) is that they can be calculated easily and directly from the (characteristic) currents if they are prescribed analytically or calculated numerically. The paradigm used, and its further extension towards the stored energy, is briefly discussed in Section A.2.1.

A particular form of the above mentioned functional (A.5), established directly for the sources (currents/charges) on the antenna, is derived using (A.2) and it reads

$$\mathcal{F}\big(\boldsymbol{J}_n\big) = \frac{\langle \boldsymbol{J}_n, \mathcal{X}\boldsymbol{J}_n\rangle}{\langle \boldsymbol{J}_n, \mathcal{R}\boldsymbol{J}_n\rangle} = -\frac{\mathrm{Re}\displaystyle\int\limits_V (\boldsymbol{A}\cdot\boldsymbol{J}_n^* - \phi\rho_n^*)\,\mathrm{d}V}{\mathrm{Im}\displaystyle\int\limits_V (\boldsymbol{A}\cdot\boldsymbol{J}_n^* - \phi\rho_n^*)\,\mathrm{d}V}, \tag{A.8}$$

where $V$ is the volume of an antenna and $\rho_n$ is the charge density. Inserting the continuity equation [85], $\rho = -\nabla\cdot\boldsymbol{J}/\mathrm{j}\omega$, the functional involves only currents and reads

$$\mathcal{F}\big(\boldsymbol{J}_n\big) = \frac{\displaystyle\iint\limits_{V\,V'} \mathcal{J}\big(\boldsymbol{J}_n\big)\frac{\cos(kR)}{R}\,\mathrm{d}V'\,\mathrm{d}V}{\displaystyle\iint\limits_{V\,V'} \mathcal{J}\big(\boldsymbol{J}_n\big)\frac{\sin(kR)}{R}\,\mathrm{d}V'\,\mathrm{d}V} = \kappa_n, \tag{A.9}$$

where $\mathcal{J}\big(\boldsymbol{J}_n\big) = \big(k^2\boldsymbol{J}_n(\boldsymbol{r})\cdot\boldsymbol{J}_n^*(\boldsymbol{r}') - \nabla\cdot\boldsymbol{J}_n(\boldsymbol{r})\nabla'\cdot\boldsymbol{J}_n^*(\boldsymbol{r}')\big)$, $R = |\boldsymbol{r}-\boldsymbol{r}'|$ is Euclidean distance, $k$ is the wavenumber and $\kappa_n$ is the Rayleigh quotient [136], which is equal to characteristic number $\lambda_n$ when the true characteristic current $\boldsymbol{J}_n$ enters into (A.9).

Thanks to the "source" formulation (A.9), arbitrary current distribution can be studied and its properties with true CMs can be compared. This formulation extends the understanding of the original definition in [9], since, as will be shown later, we can study the separated components[2] of (A.9).

It is important to stress that the functional is minimized by characteristic currents, i.e. solutions of (A.1). Such a (eigen) basis maximizes the radiated power and minimizes the net reactive power, indicating external resonances of the radiator. Hence, the extremum of (A.9) is given by characteristic basis $\{\boldsymbol{J}_n\}$ with associated eigenvalues $\lambda_n$.

[2]In the numerator, the net reactive power may be further split into its "current" and "charge" parts to express the modified magnetic and electric energies separately. For more details see [91, 137–139].

An exact analytical solution for characteristic currents is exceedingly complicated with only two bodies of finite extent already known, one of them being a spherical shell [140]. However, the expression (A.9) permits the definition of an arbitrary current distribution $\widetilde{\boldsymbol{J}}$ without the necessity of numerically computing the impedance matrix $\mathbf{Z}$ and its decomposition in (A.4). In addition, if we analytically try to test a basis $\widetilde{\boldsymbol{J}}$ that is similar to the true CM basis, we can precisely analyze its behaviour and estimate how close the selected current distribution is to the optimal solution [132].

### A.2.1 Relation Between Characteristic Modes and Stored Enegy

There is an interesting relationship between decomposition into CMs and the evaluation of the modified stored electromagnetic energy, proposed by Vandenbosch in [91] as

$$\widetilde{W}_{\mathrm{sto}} = \frac{1}{4}\left\langle \boldsymbol{J}, \frac{\partial \mathcal{X}}{\partial \omega}\boldsymbol{J} \right\rangle, \tag{A.10}$$

in which the structure of $\mathcal{X}$ is obvious from (A.2) and $\boldsymbol{J}$ is the current density which, in the context of this paper, can be composed as

$$\boldsymbol{J} \approx \sum_n \alpha_n \boldsymbol{J}_n, \tag{A.11}$$

where $\alpha_n$ is given in [9]. If (A.3) is substituted, (A.10) can be represented in a useful matrix form as proposed by Gustafsson et al. [141]

$$\widetilde{W}_{\mathrm{sto}} \approx \frac{1}{4}\mathbf{I}^{\mathrm{H}}\frac{\partial \mathbf{X}}{\partial \omega}\mathbf{I} \tag{A.12}$$

and anticipated much earlier by Harrington and Mautz [89].

It is argued in [89] that in the vicinity of $n$th modal resonances the quality factor $Q_n$, defined as

$$Q_n = \frac{\omega}{2}\frac{\partial \lambda_n}{\partial \omega}, \tag{A.13}$$

is approximately equal to the quality factor rigorously derived by Vandenbosch and later reformulated by Gustafsson, i.e.,

$$Q_{\mathbf{X},n} = \frac{\omega \widetilde{W}^n_{\mathrm{sto}}}{P^n_{\mathrm{r}}} \approx Q_n. \tag{A.14}$$

The argumentation is based on the assumption that the dominant frequency variation is due to the imaginary part of the impedance matrix [89]. Interestingly, the relationship between these two quality factors[3] can be expressed rigorously as

$$Q_n = Q_{\mathbf{X},n} - \lambda_n Q_{\mathbf{R},n}, \tag{A.15}$$

in which $Q_{\mathbf{R},n}$ is defined in the same way as $Q_{\mathbf{X},n}$, although $\mathcal{R}$ or $\mathbf{R}$ is used instead of $\mathcal{X}$ or $\mathbf{X}$. For the exact derivation of (A.15), see Appendix A.A. Moreover, the

[3]Please, keep in mind that there are number of quality factor $Q$ definitions through the literature with possible different meaning [36].

above-mentioned assumption is not needed since the equality $Q_n = Q_{\mathbf{X},n}$ is based on definition (A.5) where the eigenvalues are zero at the modal resonances.

Equality between (A.13), (A.15) and (A.10), (A.12) establishes explicit link between frequency behavior of eigenvalues $\lambda_n$ and modified modal stored energies [142]. This connection is possible thanks to the modal potential-based energies (A.6), (A.7), which occur both in definition of eigenvalues (A.5) and in (A.10) through (A.26).

## A.3 Elementary Radiators — Case Studies

In certain (simple) cases the CM basis can be sufficiently approximated by analytical currents. We inspect three canonical examples:

- a thin-strip dipole (Section A.3.1),
- two parallel coupled dipoles, separated by distance $h$ with in-phase and out-of-phase modes (Section A.3.2),
- a loop with uniform mode (Section A.3.3).

These examples establish a direct way to understand stationary inductive modes. It will be seen that these fulfil $\nabla \cdot \boldsymbol{J}(\boldsymbol{r}) = 0$, i.e., they have no charge. Observations denoted in this section introduce material which is to be developed in Section A.4.

### A.3.1 Thin-strip dipole

Let us consider a thin-strip dipole of length $L$ and width $w = L/100$. Since the dipole is thin the inductive modes are not considered and the current has to fulfill the Dirichlet boundary condition at its ends. It is significant that the choice of any mode from the basis predestinates the basis, as a whole, as the modes are orthogonal. We consider the natural first-order current basis[4]

$$\widetilde{\boldsymbol{J}}_n(z) = \mathbf{z}_0 K_0 \delta(y) \sin\left(\frac{\pi n z}{L}\right), x \in \left(-\frac{w}{2}, \frac{w}{2}\right), z \in (0, L), \tag{A.16}$$

where the surface current density

$$K_0 = \frac{1}{h} \tag{A.17}$$

is assumed. The divergence of (A.16) is

$$\mathbf{z}_0 \cdot \frac{\partial \widetilde{\boldsymbol{J}}_n(z)}{\partial z} = K_0 \delta(y) \frac{\pi n}{L} \cos\left(\frac{\pi n z}{L}\right). \tag{A.18}$$

Due to the complexity[5] of (A.16), (A.16) and (A.18) were inserted in (A.9) and solved numerically in MATLAB [144]. First, three modes, $n = \{1, 2, 3\}$, are considered. Figure A.1 shows the $\kappa_n$ quotients, together with exact eigenvalues $\lambda_n$, obtained by solving (A.1) in CST-MWS software [145]. A good match is attained, even for such a simple basis (A.16).

[4]The tilde in $\widetilde{\boldsymbol{J}}_n(z)$ expresses that we insert artificial current, since an exact form of the mode is not known.

[5]Following the tedious induced-EMF procedure [143] for basis (A.16), closed form solution to (A.9) can be found. It is expected (see results for slightly different basis treated in [143, chapter 14]) that the results would present similar complexity, not giving additional physical insight.

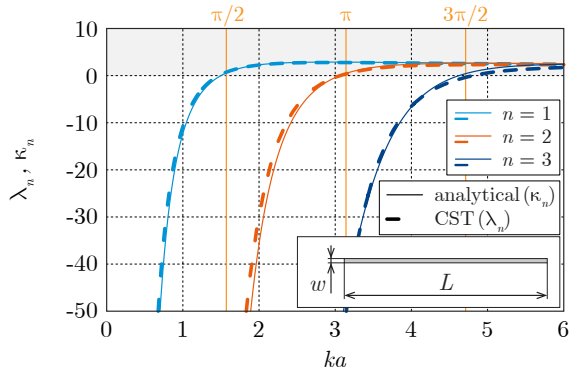


**Figure A.1:** The radiation quotients $\kappa_n$ for the first three natural modes of a thin-strip dipole (ratio $L/w = 100$ and 962 triangular segments used for numerical calculation) compared to CM eigenvalues $\lambda_n$ from CST-MWS. Resonance of modes occur for $ka \cong n\pi/2$ which agree well with theoretical predictions.

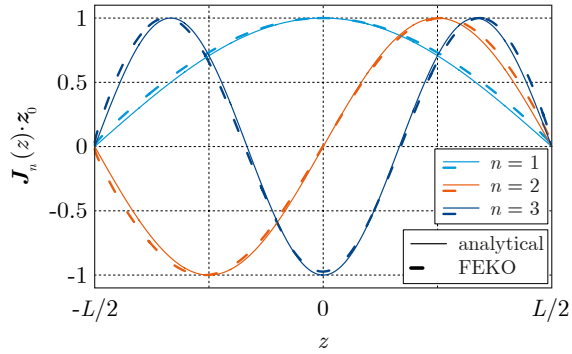


**Figure A.2:** Comparison of characteristic modes calculated in FEKO (discretization into 407 linear segments) and analytical current distribution (A.16) for the first three modes at resonance on a thin-wire dipole. The amplitude of all three modes is normalized to unity.

It can be seen from Fig. A.2 that the agreement between the CM current and its approximation is good, especially for the dominant mode. The analytical current in (A.16) is, in fact, exact for a non-radiating 1D resonator, while, in turn, the real CMs maximize radiation and, thus, the shape slightly deviates from the sine basis (A.16), [146].

### A.3.2 Two thin-strip dipoles

The next scenario involves two closely spaced collinear thin-strip dipoles with length $L$, separation $h = L/50$ and strip width of $w = L/100$. There are, depending on the

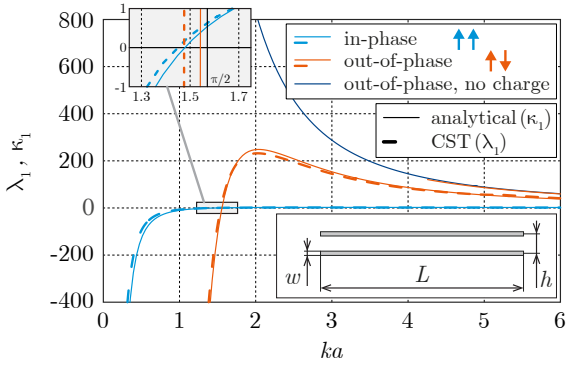


**Figure A.3:** The radiation quotients $\kappa_1$ for in-phase, out-of-phase, and testing current with no charge ($\nabla \cdot \widetilde{\boldsymbol{J}}_1 \equiv 0$) of two closely spaced thin wire ($L/h = 100$) dipoles. The detail of the position at which resonance occurs is depicted in the inset. The results are compared with the eigenvalues $\lambda_1$ of the same (thin-strip) structure calculated in CST (except for the testing current with no charge which is artificial), where 1924 triangle elements have been used.

actual orientation of currents, two possible basic modes: in-phase and out-of phase. Currents are considered in the form of fundamental distribution $\widetilde{\boldsymbol{J}}_1$ from (A.16).

For the in-phase mode [147], the course of the $\kappa_1$ quotient (light-blue line at Fig. A.3) is similar to that of the dominant mode on a single dipole. It radiates well and the two in-phase currents may be interpreted as one, flowing along a thicker dipole in a manner similar to a folded dipole. This is not the case for the out-of-phase mode, where the radiated power is much lower. Consequently, the orange line in Fig. A.3 shows extremely steep resonance for this mode. Other properties, especially those regarding radiated Q factors, have been discussed in [142] and analytically treated in [148].

Using (A.9), it is possible to investigate the hypothetical situation where the currents on the dipoles are out-of-phase but with the charge density eliminated ($\nabla \cdot \widetilde{\boldsymbol{J}}_1 \equiv 0$). It strongly resembles the situation where the ends of the dipoles are connected to form a loop. The dark-blue line in Fig. A.3 reveals that this mode does not resonate because the "charge" part in (A.9) is missing and the mode, thus, exhibits pure inductive character. In the next section we show that this behaviour is similar to the uniform zero-order mode on a loop.

### A.3.3 A loop

A loop is an elementary radiator on which the uniform (also termed static or inductive) mode with $\nabla \cdot \widetilde{\boldsymbol{J}}_0 = 0$ exists and its behaviour is similar to the modified out-of-phase mode previously analysed. Current distribution on a thin-wire loop of radius $\chi$ and height $h = \chi/100$ is expressed in cylindrical coordinates $(r, \varphi, z)$ as

$$\widetilde{\boldsymbol{J}}_0(\varphi, r, z) = \boldsymbol{\varphi}_0 K_0(z)\, \delta(r - \chi), \quad z \in \left(-\frac{h}{2}, \frac{h}{2}\right) \tag{A.19}$$

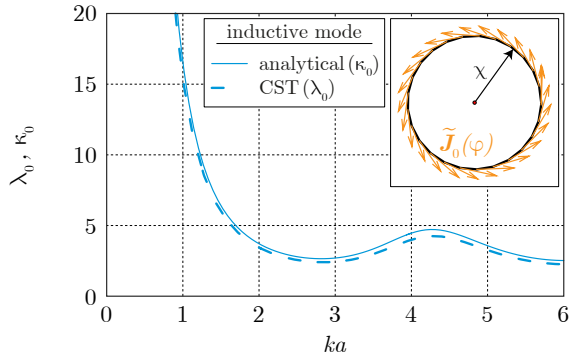


**Figure A.4:** Radiation quotient $\kappa_0$ for the uniform mode of loop. A comparison with CM eigenvalue $\lambda_0$ from CST-MWS (1258 triangle elements) is also shown. The uniform mode does not resonate in any given frequency range. However, it can be expected to resonate at extremely high values of $ka$. This behaviour will be closely investigated later.

with surface density (A.17), which simplifies (A.9) to

$$\kappa_0 = \frac{\displaystyle\int_0^{2\pi} \cos(\varphi)\,\frac{\cos(k\chi\varphi)}{\chi\varphi}\,\mathrm{d}\varphi}{\displaystyle\int_0^{2\pi} \cos(\varphi)\,\frac{\sin(k\chi\varphi)}{\chi\varphi}\,\mathrm{d}\varphi}. \tag{A.20}$$

The pure inductive character ($\kappa_0 > 0$) can be clearly seen in Fig. A.4. The agreement between (A.20) and $\lambda_0$ obtained by CST is reasonably good as the current is uniquely defined and does not change with frequency. The minor difference is caused by two slightly different models: the reduced kernel with equivalent radius $\chi/200$ has been utilized to deal with the singularity during the evaluation of (A.20), while the thin-strip loop has been calculated in the CST.

Uniform modes do not contribute significantly to far field, but they are important when evaluating near field, input impedance and stored energies.

## A.4 On the utilization of the analytical functional

The usefulness of the analytical functional (A.8) is investigated in a series of examples involving two surface bodies, a cylinder and a spherical shell. It is important to note that the purpose of this section is to demonstrate the potential applications and not to provide a comprehensive treatment of all issues mentioned.

### A.4.1 Can inductive modes resonate?

The first example deals with the same topology introduced in Section A.3.3 the only difference being the variable height $h$ of the loop. For a significant height, we obtain a cylinder and we need to integrate in $z$-dimension as well. As mentioned already, the uniform mode can occur on the loop-like topology and it is often claimed that this inductive mode, i.e., a mode with $\lambda_n \to \infty$ for $ka \to 0$, cannot resonate [10]. This question can easily be investigated using tools presented in this paper.

The same current (A.19) is assumed for the cylindrical shell. Both the uniform (A.17) and the Maxwellian surface current distribution

$$K_0(z) = \frac{2}{\pi\sqrt{h^2 - 4z^2}}, \tag{A.21}$$

were tested. In both cases the current was normalized as

$$\int_{-\frac{h}{2}}^{\frac{h}{2}} K_0(z)\,\mathrm{d}z = 1. \tag{A.22}$$

The results presented in this section were quite insensitive to the choice of (A.17) or (A.21), thus, the distribution physically closer to reality (A.21) was used.

It can easily be seen that the analytical current (A.19) has no charge, i.e.,

$$\nabla \cdot \widetilde{\boldsymbol{J}}_0(\varphi, r, z) = \frac{1}{r}\frac{\partial \widetilde{J_\varphi}}{\partial \varphi} = 0. \tag{A.23}$$

As a consequence, the $\phi\rho_0^*$ terms in (A.8) are identically zero, which, in conjunction with (A.7), immediately leads to $W_\mathrm{e}^0 = 0$. Inspecting (A.8), it seems that such a current cannot resonate, however this is only true when $\mathbf{W}^0$ is always positive, which is not the case here.

The uniform mode for a cylinder of various $\chi/h$ is depicted in Fig. A.5 in terms of eigenangles [149]

$$\delta_n = \frac{180}{\pi}\left(\pi - \operatorname{atan}(\lambda_n)\right). \tag{A.24}$$

The characteristic eigenangles normalize the eigenvalues and indicate the electromagnetic behaviour of CMs. Modes are capacitive for $\delta_n > 180°$, inductive for $\delta_n < 180°$ and resonate for $\delta_n = 180°$. We can see in Fig. A.5 that the uniform mode of the sufficiently tall cylinder can cross the resonance even if it lacks $W_\mathrm{e}$ energy (charge). This observation is verified in Fig. A.6 in which the eigenvalues were calculated using the AToM package [150] (solid lines), in CST-MWS (cross markers) and finally evaluated according to (A.17) with (A.19) substituted

$$\kappa_0 = \frac{\displaystyle\int_0^{2\pi}\int_{-\frac{h}{2}}^{\frac{h}{2}}\int_{-\frac{h}{2}}^{\frac{h}{2}} K_0(z_1)\,K_0(z_2)\cos(\varphi)\,\frac{\cos(kR)}{R}\,\mathrm{d}z_1\,\mathrm{d}z_2\,\mathrm{d}\varphi}{\displaystyle\int_0^{2\pi}\int_{-\frac{h}{2}}^{\frac{h}{2}}\int_{-\frac{h}{2}}^{\frac{h}{2}} K_0(z_1)\,K_0(z_2)\cos(\varphi)\,\frac{\sin(kR)}{R}\,\mathrm{d}z_1\,\mathrm{d}z_2\,\mathrm{d}\varphi}. \tag{A.25}$$

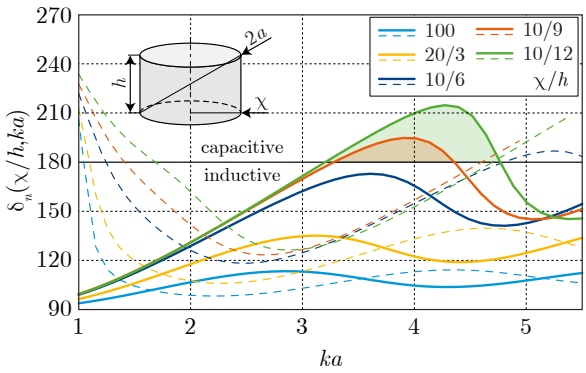


**Figure A.5:** Characteristic numbers of a PEC cylinder depicted in terms of characteristic angles $\delta_n$ as a function of $ka$ and radius to height ratio. The exact dimensions of the cylinder are shown in the inset. The capacitive modes are depicted by dashed lines, whereas the inductive modes are depicted by solid lines. It can be seen that the modes for $\chi/h = \{10/9, 10/12\}$ cross the resonance line $\delta = 180°$ at $ka \approx 3.2$.

where $R = \sqrt{2\chi^2\left(1-\cos\left(\varphi\right)\right)+\left(z_1-z_2\right)^2}$ and the axial symmetry of the cylinder have been utilized as in (A.20) in order to reduce one of integrals in $\varphi$ direction.

The fact that the uniform mode can resonate, even when $W_\mathrm{e}^0 = 0$, clearly indicates that the term $\mathbf{W}^0$ can be negative. Finally, using the formula for modified stored energy (A.10) from [91]

$$\widetilde{W}_\mathrm{sto} = \mathbf{W} + W_\mathrm{e} + W_\mathrm{rad} \tag{A.26}$$

and evaluating it according to formulas (63) and (64) in [91], we obtain the values of quality factor $Q$. The results are depicted in Fig. A.7. The uniform mode on the tall cylinder has a negative value of modified stored energy $\widetilde{W}_\mathrm{sto}$, which means that $\mathbf{W}^0 < W_\mathrm{rad}$ since $W_\mathrm{e}^0 = 0$. This is equivalent to the negative slope of eigenvalue $\lambda_0$ in (A.13) and both observations lead to the negative value of the quality factor $Q$.

The same behaviour has already been described in [12], and, so far, only loop-like, divergence-free currents were found, which supports the reasoning in [12]. Using another kind of analysis, the characteristic modes, we hypothesize that the problem is caused by extraordinary uniform currents with $W_\mathrm{e} \approx 0$ which, in reality, cannot exist independently (it can be shown that there is no realistic feeding that can excite only $\boldsymbol{J}_0$ mode).

### A.4.2 Numerical analysis of CMs as GEP – Benchmarks utilizing a spherical shell

Bearing in mind the results of the previous sections, we can perform a series of benchmarks, employing the knowledge of characteristic modes and numbers in analytical form. To do this, we need to find a scatterer whose characteristic modes are known analytically. The perfect candidate is a spherical shell, whose characteristic fields coincide with properly normalized spherical harmonics [8]. The characteristic numbers can be evaluated analytically if the characteristic currents

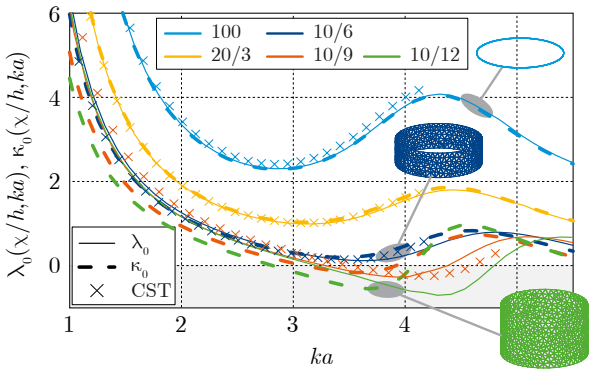


**Figure A.6:** Characteristic numbers of uniform mode of the PEC cylinder from Fig. A.5 are depicted as a function of $ka$. The dimensions are the same as in Fig. A.5. For comparison purposes, the eigenvalues $\lambda_0$ calculated in AToM are compared with CST-MWS (cross markers) and with analytical evaluation of $\kappa_0$ given by (A.25) and (A.17) (dashed lines). The overall agreement is good, however, the evaluation of the analytical current varies from true characteristic mode for higher $ka$ and higher $\chi/h$. Even in such cases the qualitative behaviour is the same – the uniform mode can resonate.

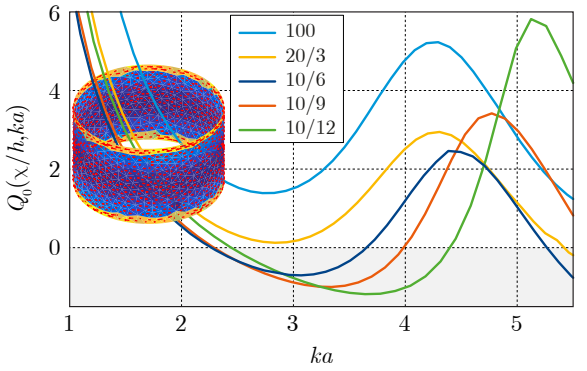


**Figure A.7:** Quality factor $Q$ of uniform modes from Fig. A.6 for the same dimensions of the PEC cylinder. Thanks to the additional term $W_{\text{rad}}$ [91], quality factor $Q$ is negative not only for modes with $\chi/h = \{10/9, 10/12\}$, but also for $\chi/h = 10/6$ (blue curve). The distribution of the current density on the cylinder is depicted in the inset.

are substituted into (A.8). This becomes of interest when dealing with the numerical solvers which are encumbered with rounding (and other) numerical errors.

The characteristic numbers $\lambda_n$, obtained using decomposition (A.4) of the impedance matrices $\mathbf{Z}$ from different commercial and in-house packages, are compared with exact radiation coefficients $\kappa_{kl}^{\mathrm{TE/TM}}$ calculated via (A.8) for spherical harmonics $\boldsymbol{J}_{kl}^{\mathrm{TE/TM}}$ [151], see Fig. A.8 and Fig. A.9, respectively. The software packages have been used to generate impedance matrices and, in all cases, the eigendecomposition has been performed in Matlab. The exact characteristic numbers are depicted by solid black lines and constitute known references. It can be seen that even state-of-the-art commercial simulators are capable of finding only the first four $\mathrm{TM}_{kl}$ and $\mathrm{TE}_{kl}$ modes. This is caused mainly by the $2k+1$ degeneracy (the number of degenerated modes increases rapidly) and by the limited (double) numerical precision. Surprisingly, the number of well-defined modes is not influenced by the number of discretization triangles $N_\Delta$. On the contrary, the relative error between analytically and numerically calculated characteristic numbers is a function of $N_\Delta$ which is confirmed by Fig. A.10. While the relative error of dominant $\mathrm{TM}_{1l}$ and $\mathrm{TE}_{1l}$ modes is a few percentage points, it quickly reaches about 10 % for groups of $\mathrm{TM}_{4l}$ and $\mathrm{TE}_{4l}$ modes. The overall results, presented in Figs. A.8–A.10, favour the in-house Matlab tool AToM. However, FEKO [152] and CEM One [153] packages reach comparable results. The routines available for free in [154] suffer from non-symmetry of produced impedance matrices. This issue can be resolved manually during pre-processing to reduce the relative error significantly. Notice that CST is not depicted since the impedance matrices cannot be acquired.

Other tests, e.g., those involving modal currents, can be performed as well. For example, the numerically calculated characteristic modes on the spherical shell can be compared with their analytical forms via

$$\epsilon_{nkl} = \left\langle \boldsymbol{J}_n, \boldsymbol{J}_{kl}^{\mathrm{TE/TM}} \right\rangle . \tag{A.27}$$

However, that study goes beyond the scope of this paper.

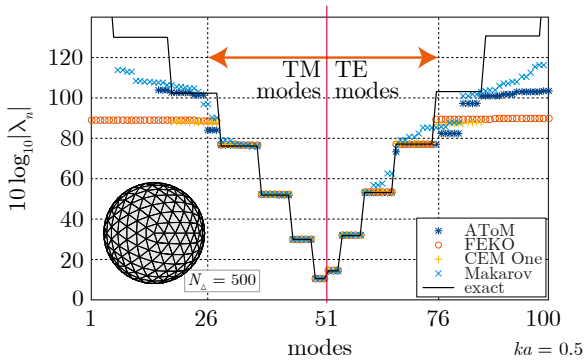


**Figure A.8:** The characteristic numbers $\lambda_n$ of the spherical shell at $ka = 0.5$ are depicted for four numerical solvers. The sphere was discretized into $N_\triangle = 500$ triangles. Modes up to $\mathrm{TM}_{4l}$ and $\mathrm{TE}_{4l}$ have been found correctly, including their degeneracy. The magnitude of all modes has been limited to values $|\lambda_{\max}| = 10^{11}$ with the characteristic modes being sorted according to their magnitude. Characteristic numbers on the left side originally had negative values, whereas numbers on the right side had positive values. The exact values of the characteristic numbers are depicted by the solid black line.

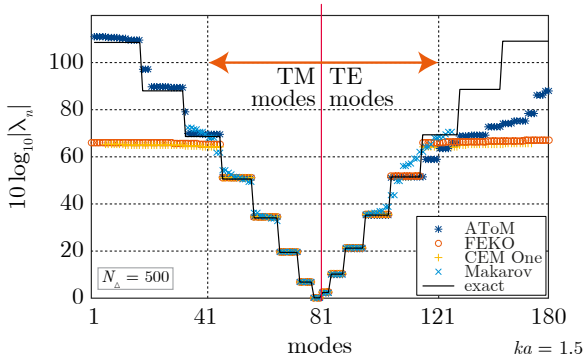


**Figure A.9:** The characteristic numbers $\lambda_n$ for the spherical shell at $ka = 1.5$. The curves represent the same quantities as in Fig. A.8, including the results processing. Compared to Fig. A.8 more than two times the number of modes have been found correctly since all modes are closer to their resonance.

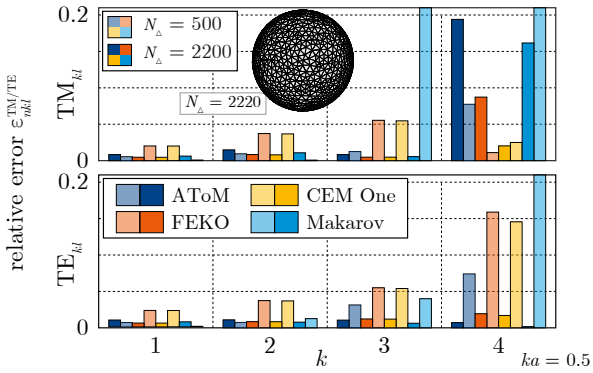


**Figure A.10:** Comparison of the relative errors of the first four TM and TE characteristic modes of a spherical shell at $ka = 1/2$. The relative error is evaluated with respect to the analytically evaluated characteristic numbers, while arithmetic mean of the characteristic numbers of all degenerated modes has been calculated and depicted by error bars. The selected software packages are differentiated by various colours, with mesh densities depicted by dark and light tints.

## A.5 Conclusion

The paper discusses specific advances of the theory of characteristic modes as introduced by Garbacz, Harrington and Mautz, but expressed here in terms of a particular functional, which is minimized by eigencurrents. This novel formula provides a different perspective on characteristic mode decomposition.

The usefulness of the functional is illustrated by three canonical examples: a dipole, two closely spaced dipoles and a loop. It was shown that the functional formulation is better suited to be analysed than the original formulation because there is no impedance matrix involved. A deeper investigation of the modes on a dipole reveals the limitations of the approximation of the zero-order current distribution expressed as a sin function.

Knowledge of the analytical functional is important for a few significant topics dealing with various issues of antenna analysis and design. In particular, any method of moment code or characteristic mode solver can be benchmarked using analytical results for a spherical shell.

## A.A Relationship between $Q_n$ and $Q_{\mathbf{X},n}$

The purpose of this appendix is to derive (A.15). To simplify the underlying mathematical nomenclature, the derivation is done for all quantities in their matrix forms. First, modal quality factor Q (A.13) is expressed in terms of characteristic currents using the matrix form of (A.5) as

$$Q_n = \frac{\omega}{2}\frac{\partial}{\partial\omega}\left(\frac{\mathbf{I}_n^{\mathrm{H}}\mathbf{X}\mathbf{I}_n}{\mathbf{I}_n^{\mathrm{H}}\mathbf{R}\mathbf{I}_n}\right), \tag{A.28}$$

then the differentiation is performed

$$Q_n = Q_{\mathbf{X},n} + \frac{\omega \dfrac{\partial \mathbf{I}_n^{\mathrm{H}}}{\partial \omega} \mathbf{X} \mathbf{I}_n}{\mathbf{I}_n^{\mathrm{H}} \mathbf{R} \mathbf{I}_n} - \frac{1}{2} \frac{\mathbf{I}_n^{\mathrm{H}} \mathbf{X} \mathbf{I}_n \omega \dfrac{\partial}{\partial \omega} \left( \mathbf{I}_n^{\mathrm{H}} \mathbf{R} \mathbf{I}_n \right)}{\left( \mathbf{I}_n^{\mathrm{H}} \mathbf{R} \mathbf{I}_n \right)^2}, \tag{A.29}$$

in which the quality factor (A.15) has been substituted and the following identity has been employed

$$\omega \frac{\partial \mathbf{I}_n^{\mathrm{H}}}{\partial \omega} \mathbf{X} \mathbf{I}_n + \mathbf{I}_n^{\mathrm{H}} \mathbf{X} \omega \frac{\partial \mathbf{I}_n}{\partial \omega} = 2\omega \frac{\partial \mathbf{I}_n^{\mathrm{H}}}{\partial \omega} \mathbf{X} \mathbf{I}_n \tag{A.30}$$

since the modal currents are supposed to be purely real. Then, the RHS of (A.4) is substituted into the last two terms on the RHS of (A.29), which yields

$$Q_n = Q_{\mathbf{X},n} + \lambda_n \left( \frac{\omega \dfrac{\partial \mathbf{I}_n^{\mathrm{H}}}{\partial \omega} \mathbf{R} \mathbf{I}_n}{\mathbf{I}_n^{\mathrm{H}} \mathbf{R} \mathbf{I}_n} - \frac{1}{2} \frac{\omega \dfrac{\partial}{\partial \omega} \left( \mathbf{I}_n^{\mathrm{H}} \mathbf{R} \mathbf{I}_n \right)}{\mathbf{I}_n^{\mathrm{H}} \mathbf{R} \mathbf{I}_n} \right). \tag{A.31}$$

Finally, performing the differentiation in the last term on the RHS of (A.31) and using identity (A.30), we get

$$Q_n = Q_{\mathbf{X},n} - \lambda_n \frac{\mathbf{I}_n^{\mathrm{H}} \omega \dfrac{\partial \mathbf{R}}{\partial \omega} \mathbf{I}_n}{2 \mathbf{I}_n^{\mathrm{H}} \mathbf{R} \mathbf{I}_n} = Q_{\mathbf{X},n} - \lambda_n Q_{\mathbf{R},n}. \tag{A.32}$$

## Acknowledgement

The authors would like to thank Lukas Jelinek and Leslie Ryan for their valuable comments and Mats Gustafsson for a fruitful discussion which led to the discovery of crucial ideas presented in the paper. The authors are also grateful for the opportunity to use the method of moment code written by Vladimir Sedenka. They would also like to thank the three anonymous reviewers whose remarks improved the clarity of this paper.

# B Validating the Characteristic Modes Solvers

**Published as:** M. Capek, **V. Losenicky**, L. Jelinek, and M. Gustafsson, "Validating the Characteristic Modes Solvers," *IEEE Transactions on Antennas and Propagation*, vol. 65, no. 8, pp. 4134–4145, Aug. 2017, DOI: 10.1109/TAP.2017.2708094.

**Abstract**— Characteristic modes of a spherical shell are found analytically as spherical harmonics normalized to radiate unitary power and to fulfill specific boundary conditions. The presented closed-form formulas lead to a proposal of precise synthetic benchmarks which can be utilized to validate the method of moments matrix or performance of characteristic mode decomposition. Dependence on the mesh size, electrical size and other parameters can systematically be studied, including the performance of various mode tracking algorithms. A noticeable advantage is the independence on feeding models. Both theoretical and numerical aspects of characteristic mode decomposition are discussed and illustrated by examples. The performance of state-of-the-art commercial simulators and academic packages having been investigated, we can conclude that all contemporary implementations are capable of identifying the first dominant modes while having severe difficulties with higher-order modes. Surprisingly poor performance of the tracking routines is observed notwithstanding the recent ambitious development.

**Index terms:** Eigenvalues and eigenfunctions, convergence of numerical methods, numerical analysis, numerical stability

## B.1 Introduction

Characteristic mode (CM) decomposition [8, 9] has become a popular tool for analyzing and designing scatterers and antennas, mainly due to the physical insight gained by modal decomposition without a particular feeding considered [10, 155]. CM decomposition yields a set of real-valued currents which form an orthonormal basis with respect to their radiation patterns and the useful properties of the CMs render this technique appealing for antenna designers [156–158]. Consequently, CM decomposition has been the subject of implementation into commercial tools, such as FEKO [152], WIPL-D [159], and CST [160], and there also exist a plethora of

academic tools, employed primarily for research related to the CM [150, 154, 161, 162].

The amount of scientific data generated along with the publication activity in the field of CMs is immense. It is therefore surprising that the question of how accurate these results are is scarcely assessed. The rare exception is an early study by Mautz and Harrington, where the results of their FORTRAN implementation [163] of CM decomposition is compared to the first analytically known eigenvalues of a spherical shell [134, Table II]. This lack of detailed numerical benchmarking of the CMs was the main motivation for the developments presented in this paper.

Benchmarking activities, see [31, 73, 74, 164] and the references therein for examples, are essential for the validation and quality assessment of methods and tools of computational electromagnetics and are of particular interest for those methods with known numerical issues, as is the case of CM decomposition [32, 33, 142, 165]. As suggested in [73], four benchmarks are readily available in computational electromagnetics, namely the comparisons to a closed form solution [31, 166], to a standard problem [167, 168], to a measurement or to other modeling techniques [169–171]. The advantages and disadvantages of these possibilities are detailed in [73] and have led authors to the decision to select a comparison to the analytical model. The drawback of this choice is that analytic solutions are only available for canonical geometries such as ellipsoids and cylinders [31, 166]. The advantage of negligible error levels in the analytic model [172, 173], however, outweighs it.

In this paper we propose four independent benchmarks devoted to various aspects of CM decomposition to validate characteristic eigenvalues, their tracking and conformity between analytically and numerically calculated characteristic currents or characteristic far-field patterns. Moreover, since CMs do not take into account feeding, they can also be used for investigating the accuracy of impedance matrix assemblage which is strongly dependent on discretization [30], the selection of basis functions [43], the quadrature rules used and singularity treatment [174, 175]. As a testing object we propose a perfectly electrically conducting (PEC) sphere for which the characteristic eigenvalues and characteristic eigencurrents are known analytically [8]. The symmetry of the spherical shell also introduces eigenspace degeneration [176] which, together with the null-space of the impedance operator at internal resonances of the shell [43], introduces serious problems with modal tracking [69–71, 177, 178].

The paper is organized as follows. CM decomposition is briefly recapitulated in Section B.2 and the analytic solution to spherical shell is provided in Section B.3. The matrix form of CM decomposition is defined in Section B.4, including a thorough discussion of the numerical issues behind the decomposition. The benchmarks are proposed in Section B.5 and applied on various packages in Section B.6. The paper is concluded in Section B.7.

## B.2 Characteristic Modes Decomposition

The CMs are introduced [9] as solutions to a generalized eigenvalue problem [179]

$$\mathcal{X}\left(\boldsymbol{J}_n\right) = \lambda_n \mathcal{R}\left(\boldsymbol{J}_n\right) \tag{B.1}$$

where $\mathcal{R}$ and $\mathcal{X}$ represent the real and imaginary parts of the impedance operator [24]

$$\mathcal{Z}\left(\boldsymbol{J}_n\right) = \mathcal{R}\left(\boldsymbol{J}_n\right) + \mathrm{j}\mathcal{X}\left(\boldsymbol{J}_n\right) = \hat{\boldsymbol{n}} \times \hat{\boldsymbol{n}} \times \boldsymbol{E}\left(\boldsymbol{J}_n\right), \tag{B.2}$$

with $\boldsymbol{E}$ being the scattered electric field [180], $\boldsymbol{J}_n$ the modal current density, $\lambda_n$ the characteristic eigenvalue and $\hat{\boldsymbol{n}}$ the unit normal to the PEC surface $\Omega$ [180] which, in this text, coincides with the radial direction. The time-harmonic quantities under the convention $\boldsymbol{\mathcal{J}}(\boldsymbol{r},t) = \mathrm{Re}\{\boldsymbol{J}(\boldsymbol{r},\omega)\exp(\mathrm{j}\omega t)\}$, with $\omega$ being the angular frequency, are used throughout the paper.

The CMs are commonly normalized with respect to unitary radiated power, *i.e.*,

$$\begin{aligned}\frac{1}{2}\int_{\Omega}\boldsymbol{J}_m^*\cdot\mathcal{Z}(\boldsymbol{J}_n)\,\mathrm{d}S =& \frac{1}{2}\int_{\Omega}\boldsymbol{J}_m^*\cdot\boldsymbol{E}(\boldsymbol{J}_n)\,\mathrm{d}S\\ &= (1+\mathrm{j}\lambda_n)\,\delta_{mn} = \kappa_n\delta_{mn},\end{aligned} \tag{B.3}$$

where $\delta_{mn}$ is the Kronecker delta [181], which allows eigenvalues $\lambda_n$ to be expressed as [9]

$$\lambda_n = \frac{\mathrm{Im}\{\kappa_n\}}{\mathrm{Re}\{\kappa_n\}} = \frac{\displaystyle\int_{\Omega}\boldsymbol{J}_n^*\cdot\mathcal{X}(\boldsymbol{J}_n)\,\mathrm{d}S}{\displaystyle\int_{\Omega}\boldsymbol{J}_n^*\cdot\mathcal{R}(\boldsymbol{J}_n)\,\mathrm{d}S}, \tag{B.4}$$

in which $\mathrm{Re}\{\cdot\}$ and $\mathrm{Im}\{\cdot\}$ denote the real and imaginary parts, respectively.

Considering only the currents distributed on surfaces, the uniqueness and completeness of CM decomposition is ensured outside internal resonances [182], *i.e.*, when all modal currents $\boldsymbol{J}_n$ radiate. In the light of (B.1) and (B.3), a sound definition of characteristic modes can thus be stated as follows: *Characteristic modes form a basis of real-valued current densities which diagonalizes the impedance operator $\mathcal{Z}$ and possess orthonormal radiation patterns.*

## B.3 Analytical Decomposition

The analytical solution of CMs decomposition on a spherical shell is presented in this section and the results are to be further used as a reference. We start with a short inspection of systems with potentially known analytical solutions in Section B.3.1 and the CMs of a spherical shell are presented in Section B.3.2.

### B.3.1 Separable Systems

Orthonormality of far-field radiation patterns and completeness are properties shared between CMs and specific solutions to the vector Helmholtz's equation in separable systems [183]. Particularly, the solutions to the vector Helmholtz's equation [183] in spherical, conical, rectangular and cylindrical (circular-cylindrical, elliptical-cylindrical, paraboloidal-cylindrical) coordinate systems, orthonormalized with respect to the far-field[1], can be equated to characteristic modes.

The above-mentioned set of possible candidates is further restricted by a practical requirement on the finite extent of the studied structures so that the model can be discretized without using periodic boundary conditions. Consequently, we are left with two feasible coordinate systems – spherical and conical. From these two,

[1]Known solutions to the vector Helmholtz's equation in spheroidal coordinates do not guarantee orthonormality [184].

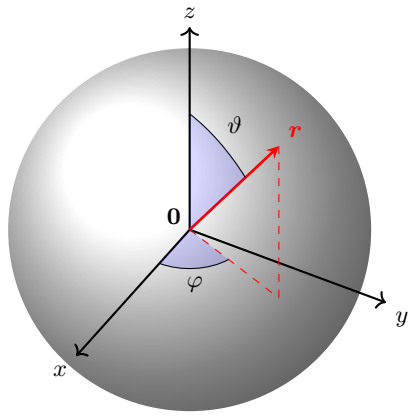


**Figure B.1:** Sketch of a spherical shell and the used coordinate system.

we have chosen spherical modes othonormal with respect to spherical surfaces [81]. Such modes correspond to a surface current density distributed on a spherical shell. In comparison to conical solutions, they are formally simpler and, significantly, exhibit high order degeneracies which complicate modal tracking considerably, see Section B.4.

### B.3.2 CM Decomposition of a Spherical Shell

The analytical form of characteristic currents on a spherical shell, see Fig. B.1, can be found in the work of Garbacz [8] where it is a result of diagonalization of a scattering matrix, though without any derivation and with the characteristic numbers $\lambda_n$ from (B.1) presented in a slightly different form $(-1/\kappa_n)$ which is more favorable for a scattering scenario. Here, instead, we provide a rationale to solve the problem from the perspective of (B.3) and then present results which can be used as a standard for numerical tests.

The orthonormal set of electric fields [81]

$$\boldsymbol{E}_{pq}^{\mathrm{TE}}\left(r \geq a\right) = -C_{pq}\left(ka\right)\gamma_p\left(ka\right)\boldsymbol{M}_{pq}\left(\mathrm{h}_p^{(2)}, r, \vartheta, \varphi\right), \tag{B.5}$$

$$\boldsymbol{E}_{pq}^{\mathrm{TM}}\left(r \geq a\right) = C_{pq}\left(ka\right)\gamma_p\left(ka\right)\boldsymbol{N}_{pq}\left(\mathrm{h}_p^{(2)}, r, \vartheta, \varphi\right) \tag{B.6}$$

corresponding to surface current densities

$$\boldsymbol{J}_{pq}^{\mathrm{TE}} = C_{pq}\left(ka\right)\hat{\boldsymbol{r}} \times \boldsymbol{N}_{pq}\left(\mathrm{j}_p, a, \vartheta, \varphi\right), \tag{B.7}$$

$$\boldsymbol{J}_{pq}^{\mathrm{TM}} = C_{pq}\left(ka\right)\hat{\boldsymbol{r}} \times \boldsymbol{M}_{pq}\left(\mathrm{j}_p, a, \vartheta, \varphi\right), \tag{B.8}$$

distributed on a spherical shell of radius $r = a$ are the desired solutions to the vector Helmohltz's equation for $\boldsymbol{r}$ denoting radial direction,

$$\gamma_p\left(ka\right) = Z_0 ka\,\mathrm{j}_p\left(ka\right)\frac{\partial\left(ka\,\mathrm{j}_p\left(ka\right)\right)}{\partial ka}, \tag{B.9}$$

functions $\boldsymbol{M}_{pq}$ and $\boldsymbol{N}_{pq}$ being defined in [81], $Z_0 = \sqrt{\mu_0/\varepsilon_0}$ being the free-space impedance and $\mathrm{j}_p$ ($\mathrm{h}_p^{(2)}$) being the spherical Bessel (Hankel) function of $p$-th order [181]. Setting then

$$C_{pq}\left(ka\right) = \frac{k}{\gamma_p\left(ka\right)}\sqrt{\frac{Z_0\left(2p+1\right)\left(p-q\right)!}{\pi\left(1+\delta_{q0}\right)p\left(p+1\right)\left(p+q\right)!}}, \tag{B.10}$$

such solutions also satisfy (B.3) and can be identified with the characteristic modes of a spherical shell, see Fig. B.1. Substituting (B.5), (B.6), (B.7) and (B.8) into (B.3), the characteristic numbers are found in analytic form as

$$\lambda_p^{\mathrm{TE}} = -\frac{\mathrm{y}_p\left(ka\right)}{\mathrm{j}_p\left(ka\right)} \tag{B.11}$$

and

$$\lambda_p^{\mathrm{TM}} = -\frac{\left(p+1\right)\mathrm{y}_p\left(ka\right) - ka\,\mathrm{y}_{p+1}\left(ka\right)}{\left(p+1\right)\mathrm{j}_p\left(ka\right) - ka\,\mathrm{j}_{p+1}\left(ka\right)}, \tag{B.12}$$

where $\mathrm{y}_p$ is the spherical Bessel function of the second kind and $p$-th order.

To simplify the notation, an aggregated index $n$ is adopted from [185] as

$$\boldsymbol{J}_n = \left\{\boldsymbol{J}_{pq}^{\mathrm{TE}}, \boldsymbol{J}_{pq}^{\mathrm{TM}}\right\}, \tag{B.13}$$

and the characteristic numbers, $\lambda_n \in (-\infty, \infty)$, are rescaled in terms of so-called characteristic angles $\delta_n \in [90^\circ, 270^\circ]$ as [149]

$$\delta_n = 180\left(1 - \frac{1}{\pi}\arctan\left(\lambda_n\right)\right). \tag{B.14}$$

The characteristic numbers $\lambda_n$ belonging to the first six TE and TM modes (not counting degenerations) are depicted in Fig. B.2 and the corresponding characteristic angles $\delta_n$ are depicted in Fig. B.3.

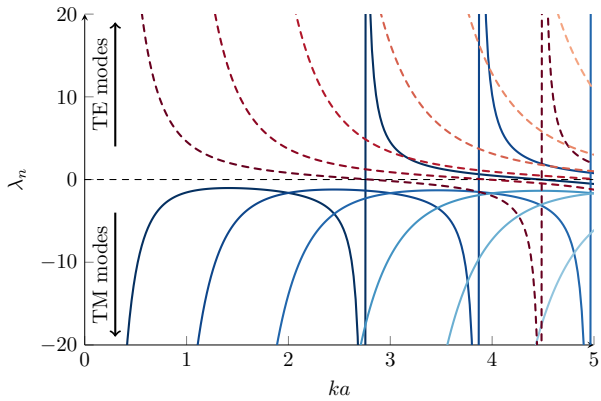


**Figure B.2:** Characteristic eigenvalues $\lambda_n$ of a spherical shell of radius $a$. The first six TE and TM modes are depicted. The vertical lines (where the eigenvalues are not well-defined functions) correspond to the internal resonances and they are kept in the figure to simplify the tracking of different modes. Modes with $\lambda_n > 0$ are predominantly inductive while $\lambda_n < 0$ are predominantly capacitive.

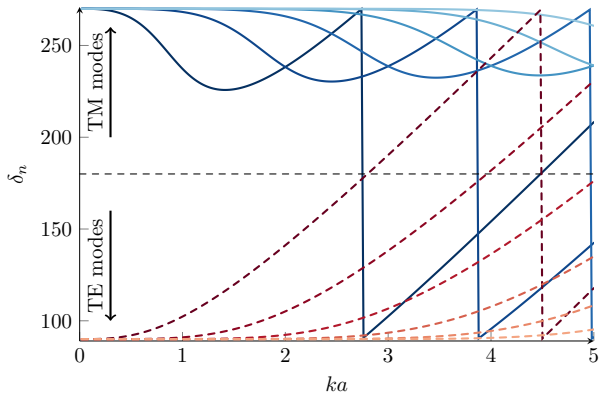


**Figure B.3:** Characteristic eigenangles $\delta_n$ of a spherical shell. The first six TM and TE modes are depicted, *cf.* Fig. B.2.

## B.4 Numerical Evaluation

A numerical solution to the characteristic modes of a spherical shell is found in this section, including a discussion of related numerical issues.

In the common treatment [43], the operator (B.2) is represented in a basis of

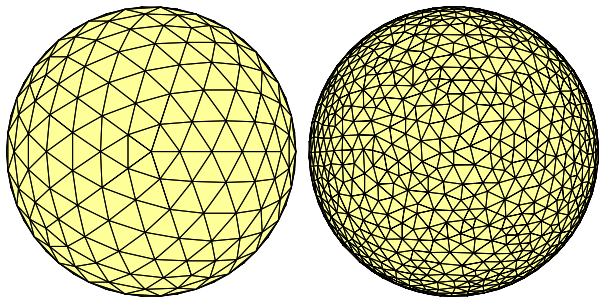

**Figure B.4:** Spherical shell from Fig. B.1 triangularized into 500 triangles (left) and 2200 triangles (right) with 750 (left) and 3300 (right) RWG basis functions, respectively. The coarser discretization is used throughout the paper and, wherever required, the results are compared with those for the denser grid.

piecewise functions $\{\boldsymbol{\psi}_u\}$ [43] in the form of the impedance matrix

$$\mathbf{Z} = \mathbf{R} + \mathrm{j}\mathbf{X} = [Z_{uv}] = \left[ \int_{\Omega} \boldsymbol{\psi}_u^* \mathcal{Z}\left(\boldsymbol{\psi}_v\right) \,\mathrm{d}S \right] \tag{B.15}$$

and the relation (B.1) is transformed into the matrix equation

$$\mathbf{X}\mathbf{I}_n = \lambda_n \mathbf{R}\mathbf{I}_n \tag{B.16}$$

with modal current density from (B.1) calculated as

$$\mathbf{J}_n = \sum_u I_{nu}\, \boldsymbol{\psi}_u. \tag{B.17}$$

Formula (B.16) is of general validity, and, therefore, characteristic modes of arbitrarily shaped bodies can be found in this way at the expense, however, of the occurrence of various numerical issues and artifacts which are discussed below.

### B.4.1 Known Numerical Issues

The numerical issues connected to (B.16) will be demonstrated on a spherical shell discretized into a triangular mesh grid, see Fig. B.4, with RWG basis functions [44] applied. The mesh grid was exported from FEKO [152] as a NASTRAN file [186] and is freely available [116]. Spherical geometry allows a near-perfect triangular mesh consisting of equiangular triangles to be generated, see Fig. B.4.

When dealing with the CMs, the following issues arise:

#### B.4.1.1 Indefiniteness of a Real Part of the Impedance Matrix

The importance of algebraic properties of matrices $\mathbf{R}$ and $\mathbf{X}$ can readily be seen from (B.3) and (B.16). To obtain real characteristic numbers and vectors, these

matrices have to be symmetric, *i.e.*, Galerkin testing procedure should properly be applied [24]. If matrices are slightly non-symmetric, they can be symmetrized *ex post* as

$$\mathbf{Z}_{\text{sym}} = \frac{1}{2}\left(\mathbf{Z} + \mathbf{Z}^{\text{T}}\right), \tag{B.18}$$

in which superscript T denotes matrix transposition. Since matrix $\mathbf{R}$ serves in (B.16) as a weighing operator [179] and represents radiated power, its positive definiteness, $\mathbf{R} \succ 0$, is crucial. In fact, a potential violation of this condition is one of the biggest known issue related to the CMs [134]. On the contrary, matrix $\mathbf{X}$ is usually well-posed.

In order to present this last problem numerically, matrix $\mathbf{R}$ of a spherical shell discretized into 500 triangles (left panel in Fig. B.4) is decomposed as

$$\mathbf{R}\hat{\mathbf{I}}_n = \xi_n \hat{\mathbf{I}}_n \tag{B.19}$$

and the eigenvalues $\xi_n$ are depicted in Fig. B.5. The results correspond to matrix $\mathbf{R}$ obtained by two different packages: the commercial package FEKO [152] and the academic tool AToM [150]. For the sake of clarity, the absolute values of the eigenvalues are shown in logarithmic scale and the negativity of the eigenvalues is indicated by the marker (star) used. Note that eigenvalues $\xi_n$ are proportional to the radiated power [24].

Generally, we see that only a few modes radiate well (top left part of Fig. B.5) and that at least one half of all eigenvalues are negative (right half of Fig. B.5). These negative eigenvalues are related to the presence of ubiquitous numerical noise and they should be removed from matrix $\mathbf{R}$ using (B.19) and substituting $\xi_n \equiv 0$ [28] in the consecutive back-composition

$$\mathbf{R}_{\text{pos}} = \hat{\mathbf{I}}\boldsymbol{\xi}\hat{\mathbf{I}}^{\text{T}}, \tag{B.20}$$

where $\hat{\mathbf{I}}$ is a matrix containing column vectors $\hat{\mathbf{I}}_n$ and $\boldsymbol{\xi}$ is a diagonal matrix containing eigenvalues $\xi_n$. Unfortunately, formula (B.20) cannot cure the imminent fact that matrix $\mathbf{R}$ is ill-conditioned.

Matrix $\mathbf{R}$ originating from FEKO is non-symmetric, which causes its different appearance as compared to other curves. For the second set of eigenvalues, the matrix has been symmetrized according to (B.18) prior to decomposition (B.19). Two different orders of Gaussian quadrature rule [187] have been used in AToM [24]. In comparison to FEKO, AToM has been able to find more modes, namely those highlighted in the shaded oval denoted by number I. This fact will play an important role at a further point and is most probably caused by single precision arithmetic used in FEKO, see Appendix B.A for the simulation setup. It is also demonstrated by high negative eigenvalues highlighted by oval II in Fig. B.5 that centroid approximation (only one quadrature point in each triangle) does not lead to a well behaved matrix $\mathbf{R}$. It is obvious that the number of properly found modes directly reflect the quality of numerics used when constructing the impedance matrix.

### B.4.1.2 Mode Degeneracy

Degeneracy can be traced back to the geometrical symmetries of the $\Omega$ region [50, 176, 188] and it poses complications with mode tracking [33, 69, 70]. A spherical shell has a degeneracy [81] of

$$N(p) = 2p + 1, \tag{B.21}$$

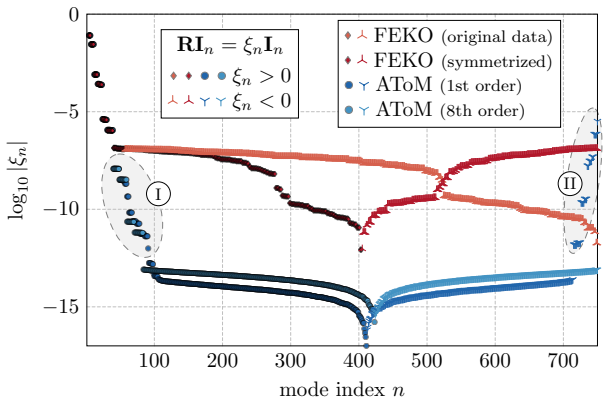


**Figure B.5:** Eigenvalues of a real part of the impedance matrix of a spherical shell discretized into 500 triangles.

which means that for $p$-th order there are $N_p$ degenerated modes. Therefore, each solid and dashed line in Fig. B.2 and Fig. B.3 has $2p + 1$ multiplicity. The effect of degeneracy is also seen in Fig. B.5 as it appears as stairs spreading their length from left to right. Except for geometrical degeneracies (B.21), the numerical tracking procedure is yet more complicated for the occasional degeneracies occurring at frequencies where TM and TE modes intersect.

The possibility of reducing the number of geometrically degenerated modes lies in the utilization of the procedure from [188] which, however, relies on a particular choice of basis functions and it is therefore problem-dependent. One useful work-around is to make the mesh grid markedly non-symmetrical which helps to remove the degeneracies.

### B.4.1.3 Internal Resonances

Internal resonances are inherent to all closed PEC surfaces [43, 182, 189] and make the matrix $\mathbf{Z}$ ill-conditioned at resonance frequencies. They occur at those frequencies at which non-radiating current sources may exist, *i.e.*, where denominators of (B.11) and (B.12) vanish. The consequences of solving (B.16) at these frequencies are explained in [32, 189, 190], where it is also important to notice the comparison between resonances of the CMs and natural modes. At the internal resonance, the characteristic numbers abruptly change value between plus and minus infinity, see Fig. B.2. The majority of tested packages suffer from this issue, although they can effectively be solved using Combined Field Integral Equation (CFIE) [191].

### B.4.1.4 Dependence on Conformity and Mesh Density

Equation (B.16) is solved for approximate models like those depicted in Fig. B.4 and the question arises of which mesh scheme describes the original smooth object best [43, 172]. Quality of mesh grid, mesh density with respect to conformity, rounding errors, and computational requirements should all be taken into account

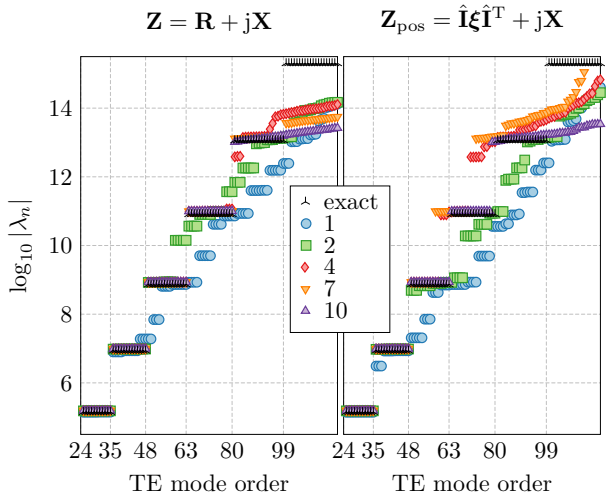


**Figure B.6:** Comparison of characteristic eigenvalues of the impedance matrix found by the AToM package with analytically known results. The results correspond to a spherical shell discretized into 500 triangles with electric size $ka = 1.5$. Various orders of quadrature rule [187] used in the evaluation of the impedance matrix were used and the graph is zoomed in on the area in which the data differ the most. The left panel shows CM decomposition (B.16) of the original impedance matrix $\mathbf{Z}$ (B.15), while the right panel shows CM decomposition of the modified impedance matrix $\mathbf{Z}_{\mathrm{pos}}$ with a positively definite real part (B.20).

when dealing with this question. It is also important to note that, although a finer mesh better describes the original object, the increased number of potential modes is redeemed by a higher level of numerical noise resulting in more invalid modes, *cf.* Fig. B.5, longer computational time and higher memory consumption.

#### B.4.1.5 Dependence on Integration and Singularity Treatment

As with the previous issue, this point is merely a technicality, yet it strongly influences the final results. The higher order quadrature rules [43] have a great impact on the quality of results, see Fig. B.6. Higher-order basis functions can be advantageously applied as well [43]. Special care should also be taken with singularities [174, 175] occurring during the evaluation of (B.15).

## B.5 Benchmarks

Knowing the analytic results and common issues behind characteristic mode decomposition, the following benchmarks are proposed:

**Test #1** Characteristic eigenvalues of impedance matrix $\mathbf{Z}$ for a given electrical size $ka$, see Section B.5.1.

| $ka$ | | Single p. | Double p. | Quadruple p. |
|---|---|---|---|---|
| | bits $b$ | 23 | 52 | 112 |
| | $\log_{10}\left(2^b\right)$ | $\approx 6.924$ | $\approx 15.65$ | $\approx 33.72$ |
| 0.5 | $p_{\max}^{\mathrm{TE/TM}}$ | 4/4 | 7/7 | 12/12 |
| | $N\left(p_{\max}^{\mathrm{TE/TM}}\right)$ | 24/24 | 63/63 | 168/168 |
| 1.5 | $p_{\max}^{\mathrm{TE/TM}}$ | 6/6 | 10/10 | 17/17 |
| | $N\left(p_{\max}^{\mathrm{TE/TM}}\right)$ | 48/48 | 120/120 | 323/323 |

**Table B.1:** Number of theoretically achievable TE and TM modes dependent on used numerical precision in Matlab and electrical size $ka$. The number of TE and TM modes $N$ was calculated according to (B.21) with $p_{\max}^{\mathrm{TE}}$ and $p_{\max}^{\mathrm{TM}}$ substituted.

**Test #2** Modal tracking in a given range of $ka$, see Section B.5.2.

**Test #3** Conformity between analytically and numerically calculated characteristic currents $\boldsymbol{J}_n$, see Section B.5.3.

**Test #4** Correspondence of analytically and numerically calculated characteristic far-fields, see Section B.5.4.

All the aforementioned tests are extremely simple to implement and add minimal demands on post-processing. The key features to be investigated within all the tests are

- choice of the basis and testing functions,
- precision of the integration scheme used,
- precision and robustness of the singularity treatment used,
- quality of the tracking algorithm.

Notice that a fixed mesh is used and that the errors due to meshing are not considered.

### B.5.1 Test #1

The first test focuses on the quality of an impedance matrix, thus making it an efficient benchmark of the method of moments codes. The analytically known eigenvalues $\lambda_n$ from (B.11) and (B.12) are compared with eigenvalues obtained by CM decomposition (B.16) of impedance matrix $\mathbf{Z}$ from (B.15), its symmetrized form $\mathbf{Z}_{\mathrm{sym}}$ from (B.18), or of an impedance matrix with a positively definite real part (B.20). The test is proposed for electrical sizes $ka = 0.5$ and $ka = 1.5$, so that both electrically small and reasonably large objects are tested. The spectrum of eigenvalues is calculated by the generalized Schur decomposition [179] (`eig` with QZ algorithm in Matlab) and all eigenvalues which are infinite, complex-valued or correspond to mode with $\mathbf{I}_n^{\mathrm{H}}\mathbf{R}\mathbf{I}_n \leq 0$ are removed. The analytical results are depicted in Fig. B.7. The maximum number of modes for three different numerical precisions are summarized in Table B.1.

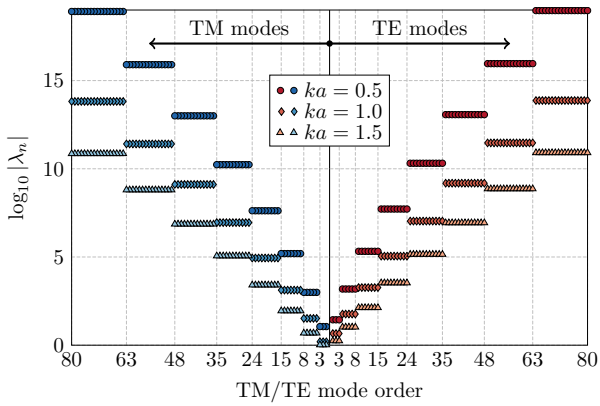


**Figure B.7:** Analytically evaluated characteristic numbers of TM and TE modes of a spherical shell for several electrical sizes $ka$.

### B.5.2 Test #2

The second test investigates the frequency behavior of characteristic eigenvalues. The setup is as follows: 100 modes should be calculated at 226 equidistantly spaced frequency samples between $ka = 0.5$ and $ka = 5$, and mode tracking should be provided. The number of modes is selected from Fig. B.2, considering mode degeneracy (B.21) so that, theoretically, all required data to track the first six TE and TM modes are provided ($2\sum_1^6 (2p+1) = 96$). The frequency span is chosen to cover a couple of internal resonances. The number of frequency samples is chosen as a trade-off between sufficient $ka$ sampling ($\Delta ka = 0.02$) and a computationally feasible solution. The reference solution is depicted in Fig. B.2 and Fig. B.3.

### B.5.3 Test #3

The conformity of numerically calculated characteristic currents $\mathbf{J}_n$ with the analytical results (B.7) and (B.8) is studied with the third test using

$$\chi_n = \max_p \sqrt{\sum_{q=-p}^{p} \left| \int_\Omega \hat{\mathbf{J}}_n(\mathbf{r}) \cdot \hat{\mathbf{J}}_{pq}^{\mathrm{TM/TE}}(\mathbf{r}) \, \mathrm{d}S \right|^2}, \tag{B.22}$$

and the current $\hat{\mathbf{J}}(\mathbf{r})$ is normalized according to

$$\hat{\mathbf{J}} = \frac{\mathbf{J}}{\sqrt{\int_\Omega \mathbf{J}(\mathbf{r}) \cdot \mathbf{J}(\mathbf{r}) \, \mathrm{d}S}}. \tag{B.23}$$

Ideally, the coefficient $\chi_n$ should be equal to unity for all $n$.

### B.5.4 Test #4

Far-fields $\boldsymbol{F}_{pq}^{\mathrm{TE/TM}}(\vartheta,\varphi)$ of analytical characteristic modes of a spherical shell can be deduced from (B.5), (B.6) and, following the definition of characteristic modes from Section B.2, they should form an orthogonal and complete set. Since characteristic radiation patterns are commonly used in practice [71, 192], a meaningful test is to compare numerically evaluated characteristic far-fields $\boldsymbol{F}_n$ with analytical ones via

$$\zeta_n = \frac{\max\limits_{p} \sum\limits_{q=-p}^{p} \left| P_{pq,n}^{\mathrm{TE/TM}} \right|^2}{\sum\limits_{p,q} \sum\limits_{\mathrm{TE/TM}} \left| P_{pq,n}^{\mathrm{TE/TM}} \right|^2} \tag{B.24}$$

where

$$P_{pq,n}^{\mathrm{TE/TM}} = \frac{1}{2Z_0} \int\limits_{4\pi} \left( \boldsymbol{F}_{pq}^{\mathrm{TE/TM}} \right)^* \cdot \boldsymbol{F}_n \sin\vartheta \,\mathrm{d}\vartheta \,\mathrm{d}\varphi. \tag{B.25}$$

The metric $\zeta_n$ should ideally be equal to unity for all $n$.

As for the previous test, metric $\zeta_n$ should mostly judge the quality of numerically evaluated current patterns which are directly reflected in the corresponding far-fields. Simultaneously, it tests the fundamental property of CMs, far-field orthogonality.

## B.6 Results

This section presents the results of four tests from the last section performed on the numerical packages implementing method of moment solution to field integral equations, namely on:

- FEKO [152],
- CST-MWS [160],
- WIPL-D [159],
- CEM One [193]
- AToM [150],
- Makarov [154].

The most important settings of the solvers used are specified in Appendices B.A–B.E.

### B.6.1 Test #1

The results of the first test are depicted in Fig. B.8 for electric size $ka = 0.5$ and in Fig. B.9 for electric size $ka = 1.5$, respectively. In both cases, the spherical shell was discretized into 500 discretization elements and, unless otherwise stated, the triangular mesh grid from Fig. B.4 was used. The impedance matrices of FEKO and Makarov's code are originally slightly non-symmetric, therefore (B.18) was applied before the analysis. The order of Gaussian quadrature in CEM One and AToM can be controlled by the user which is why the selected integration scheme is explicitly mentioned in the parentheses. Data from CST-MWS were not analyzed[2].

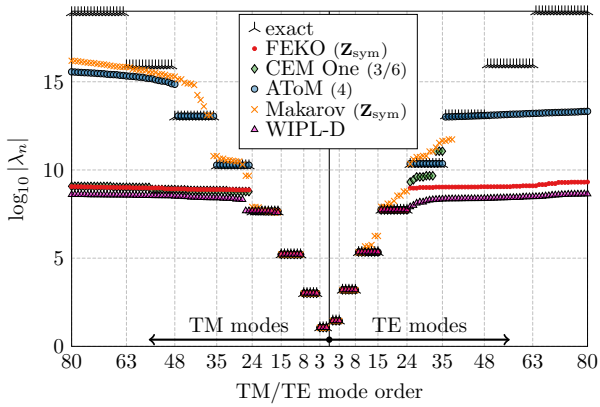


**Figure B.8:** Characteristic numbers for a spherical shell of electrical size $ka = 0.5$ discretized into 500 triangles. Selected commercial and in-house tools are compared. The small number in brackets means the order of quadrature rule. Matrices which have been manually symmetrized are explicitly mentioned.

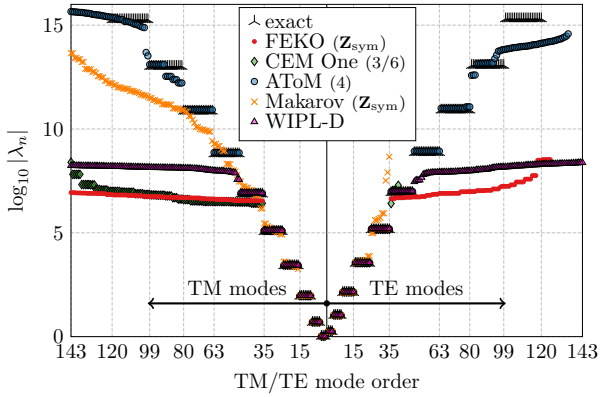


**Figure B.9:** Characteristic numbers for a spherical shell of electrical size $ka = 1.5$ discretized into 500 triangles. The meaning of all abbreviations is the same as in Fig. B.8.

The accuracy of the academic package AToM is limited by the double numerical precision used. Therefore, the six and eight lowest order non-degenerated TE and TM modes are correctly found in Fig. B.8 and Fig. B.9, respectively. The commercial packages are able to represent the first four or five modes, most likely for the use of single precision. Notice that, theoretically, 14 or 20 non-degenerated TM and

[2]The impedance matrix is not accessible and it is thus not guaranteed that the same algorithm for eigenvalue decomposition is used for all tested cases.

TE modes could be retrieved, see Table B.1. In the light of this, the number of correctly found modes is relatively low. The lack of numerical precision can be partially compensated using VPA (Variable Precision Arithmetic) in Matlab or the Multiprecision Computing Toolbox [194]. However, these improvements have the potential to add only a couple of additional modes and always at the cost of extreme computational time.

The presented results suggest that the slight non-symmetry of an impedance matrix is not a major issue. However, care should be taken with the numerical precision used and the application of the high-order quadrature rule in conjunction with the precise implementation of singular terms.

### B.6.2 Test #2

This test focuses on the mode tracking algorithm, therefore, only packages with this utility implemented could be analyzed. In all cases, the tracking analysis was performed in the frequency range from $ka = 0.5$ to $ka = 5$, and then, to produce lucid graphical outputs, only the problematic region of $ka \in [2.5, 5]$ was depicted.

The results from the AToM package are depicted in Fig. B.10. The panel (a) shows the raw data acquired from the Implicitly Restarted Arnoldi method [195] (`eigs` in Matlab). This method was advantageously utilized since only the first 100 modes are required at each frequency. The gray-colored ellipses highlight two exemplary samples at which the data are missing. The panel (b) shows the modal data after the tracking procedure. A careful inspection reveals a couple of disconnected modes, one incomplete mode (missing data are highlighted by the gray-colored ellipse) and one missing inductive mode (depicted by the red dashed line). The systematic frequency shift between analytically predicted and numerically calculated internal resonances can be attributed to finite meshing is a consequence of the slightly smaller electrical size of the mesh grid.

The results from the FEKO package are depicted in Fig. B.11. The raw data in panel (a) are similar to those found with the AToM package, however, the tracked modes in panel (b) are far from perfect.

The next analyzed package is WIPL-D which uses a quadrilateral mesh grid with higher-order basis functions which is why its results cannot be directly compared with other packages. However, the results seem promising, see Fig. B.12, except at those places where the crossing-avoidances were incorrectly detected (see the inset).

The last package to undergo testing was CST-MWS. In comparison to the previous packages, CST-MWS uses CFIE for CMs analysis. Only the first four modes were found and, even though 226 frequency samples were required, 1000 interpolated values were returned, see Fig. B.13. The effect of the interpolation is evident from the enlarged section. The tracking procedure seems to be relatively computationally demanding as only 15 modes could be calculated and only four modes were found. On the other hand, these modes are well-tracked.

### B.6.3 Test #3

The third test was performed only for the AToM and FEKO packages at $ka = 1.5$ for a mesh grid composed of 500 and 2200 triangles, see Fig. B.14 and Fig. B.15. The similarity coefficient $\chi_n$ from (B.22) decreased significantly faster for the poorer mesh grid, however, the number of sufficiently represented modes, say those with $\chi_n > 0.9$, was similar for both mesh grids. The influence of the higher-order quadrature rule is obvious and the number of well-defined currents, approximately the first 80 TM

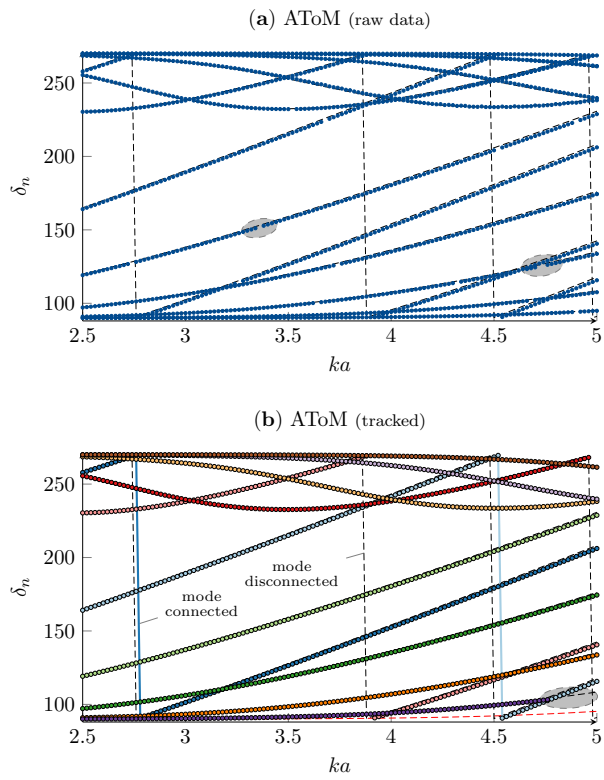


**Figure B.10:** Test of tracking procedure provided by the AToM package. Raw characteristic angles are depicted in panel (a). Tracked modes are depicted in panel (b). Due to the complexity of original data (100 modes), only one mode from each degenerated eigenspace is depicted. This explains the missing data in panel (a), highlighted by the shaded ovals. Notice the depicted difference in panel (b) for connected and disconnected modes.

and TE modes, including degeneracies, corresponds perfectly with the number of precisely calculated eigenvalues, see Fig. B.9.

### B.6.4 Test #4

Test metric $\zeta_n$ from (B.24) was evaluated at electrical size $ka = 1.5$ for data obtained from the AToM and FEKO packages, with results depicted in Fig. B.16 and Fig. B.17. The test was not performed using the CST-MWS package since it internally normalizes characteristic modes via $L^2$ norm and not via (B.3). The results could, therefore, not be compared with others. The CEM One package does not have characteristic far-fields implemented.

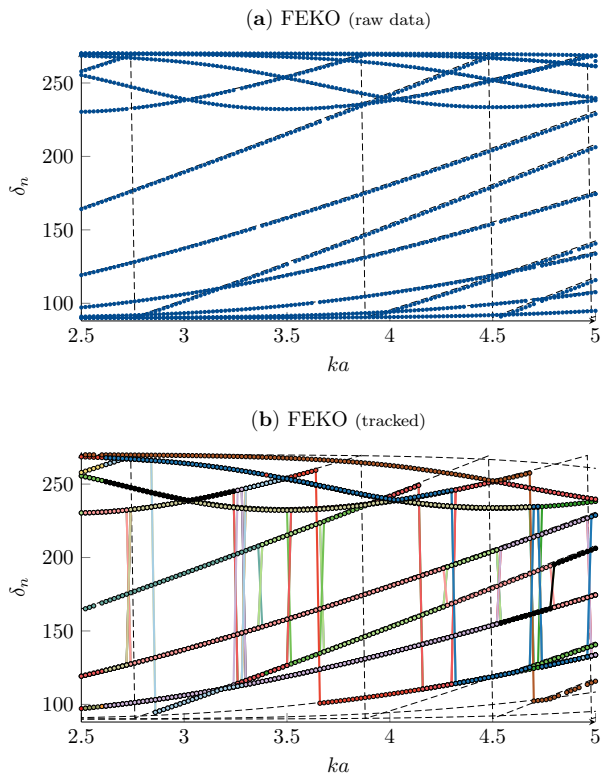


**Figure B.11:** Comparison of raw (untracked) and tracked characteristic angles for the FEKO package.

For proper assessment, the results in both figures should be compared simultaneously since only simultaneous compliance with $\zeta_n \approx 1$ and $P_{\mathrm{r},n} \approx 1$ is sufficient to pass the test, with $P_{\mathrm{r},n}$ being the far-field radiated power of the $n$-th characteristic mode, *i.e.*, the denominator of (B.24). The normalization of radiated power may seem to be automatic, but for higher order modes the normalization (B.3), performed numerically via $\mathbf{I}^{\mathrm{H}}\mathbf{R}\mathbf{I} = 2$, does not imply unitary radiated power in far-field.

Only modes with real eigenvalues and positive radiated power were taken in the case of AToM. Data from FEKO were left in their original form. In all cases, the integration (B.25) was discretized in $N_\vartheta = N_\varphi = 100$ points. This angular discretization was checked by artificially testing analytical modes which resulted in $\zeta_n \approx 1$ and $P_{\mathrm{r},n} \approx 1$ for all analytical modes within the depicted range.

The performance in all tested cases is quite unsatisfactory, but generally corresponds to the other tests. The results suggest that far-field decomposition into more than five TE modes and five TM modes (not including degenerations) of a spherical shell is unsafe within the used triangularization of a sphere and double precision. Higher quadrature rules and careful singularity treatment, seen in the case of AToM

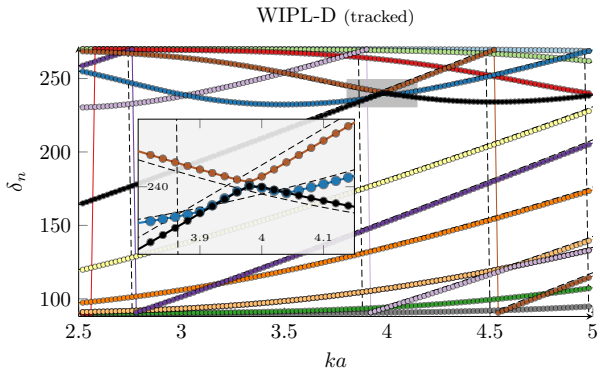


**Figure B.12:** Tracked characteristic angles for the WIPL-D package. The region highlighted by gray color is enlarged in the inset and shows that selected modes are not tracked perfectly.

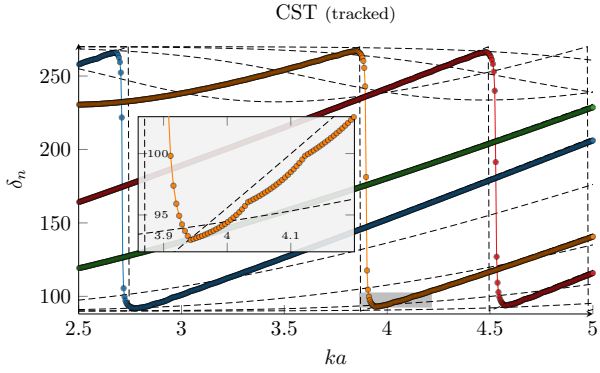


**Figure B.13:** Tracked characteristic angles for the CST package. The region highlighted by gray color is enlarged in the inset and shows that data are highly interpolated.

with an 8-th order of quadrature, add more proper modes, but the gain is not as high as in other tests.

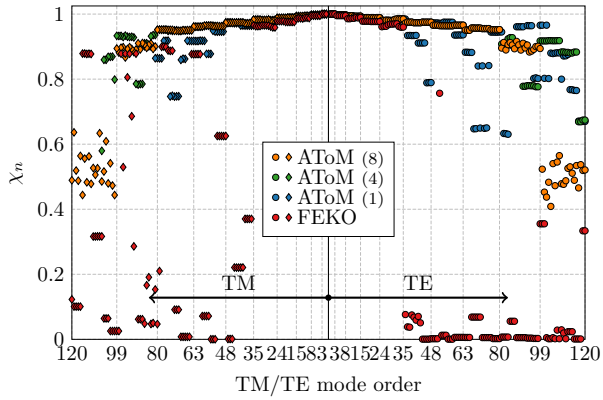


**Figure B.14:** Similarity of numerically evaluated characteristic currents for a spherical shell discretized into 500 triangles and an analytically known current from (B.7) and (B.8). The electrical size is $ka = 1.5$. Coefficients $\chi_n$ were calculated according to (B.22) for three different orders of the Gaussian quadrature rule $\{1, 4, 8\}$ used in the AToM package to calculate impedance matrices and for the FEKO package.

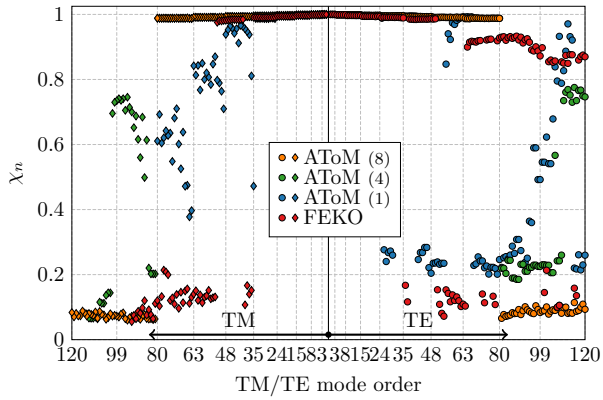


**Figure B.15:** Same similarity study as in Fig. B.14 which was for a spherical shell discretized into 2200 triangles.

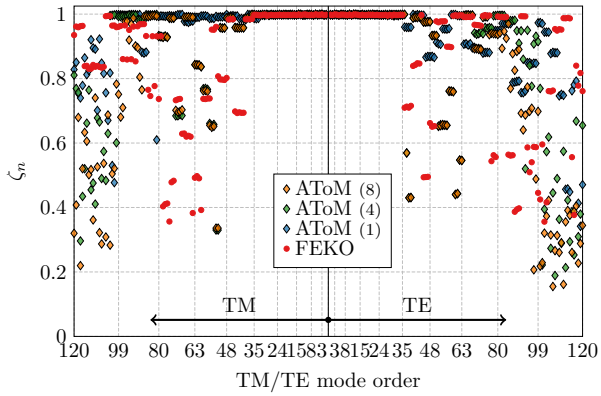


**Figure B.16:** Similarity of numerically and analytically evaluated characteristic far-fields for a spherical shell discretized into 500 triangles at electrical size $ka = 1.5$. Coefficients $\zeta_n$ were calculated according to (B.24).

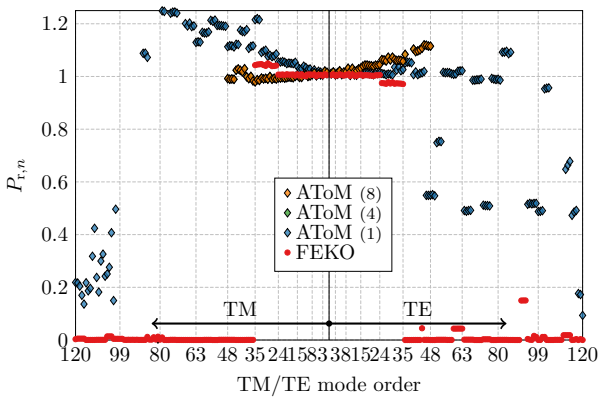


**Figure B.17:** Far-field radiated power (denominator of (B.24)) of $n$-th characteristic mode. The same input data as for Fig. B.16 have been used. Note that the radiated power of some higher order modes is out of the depicted range.

## B.7 Conclusion

A set of sensitive benchmarks applicable to the majority of contemporary method of moments packages was proposed. The major advantages are formal simplicity, the low number of necessary inputs, the independence on particular feeding model and minimal required post-processing.

All tested packages showed satisfactory performance in calculating characteristic eigenvalues at a single frequency, although some of them were limited out of the single numerical precision range. Without exception, however, they performed well below theoretically achievable results. In the case of modal tracking, the differences were more severe and some packages showed unsatisfactory results. It has been demonstrated that factors, such as singularity treatment, high-order quadrature rules and used floating-point numerical precision, greatly influence the results. A persisting problem is also the numerical ill-posedness of the real part of impedance matrix caused by dominance of only couple of modes. The application of any technique increasing its dynamical range while preserving its precision is, therefore, of interest since it may significantly improve the number of correctly found characteristic modes.

Future work should be aimed toward analytical characteristic modes of more complex shapes which could further stress the precision of available method of moments codes. Promising candidates are surfaces which can be described in conical or spheroidal coordinate systems.

## B.A FEKO Setup

FEKO (ver. 14.0-273612, [152]) was used with the following settings: a mesh structure was imported into the software using the Nastran file format [186] and the CMs and far-fields were chosen as a request for the FEKO solver. Data from FEKO were acquired using *.out, *.os, *.mat and *.ffe files. The impedance matrices were imported by an in-house wrapper [162]. Double precision was enabled for data storage in solver settings. The number of modes used for each test were as follows: Test #2 99 modes, Test #3 500 modes and Test #4 300 modes, respectively.

## B.B WIPL-D Setup

WIPL-D (v13, [159]) uses higher-order basis functions with a quadrilateral mesh grid. Therefore, individual meshing was used. Surface angle tolerance was set to 15 degrees. Additionally, a non-symmetrical mesh was created in order to obtain better stability of mode calculations. An integral solver with CM decomposition was utilized with double precision and enhanced-1 for Integral Accuracy. The matrices for Test #1 were delivered by the developer of the WIPL-D package and data for Test #2 included first 100 modes.

## B.C CST-MWS Setup

CST-MWS (ver. 2016.7, [160]) setting was as follows: the spherical shell was created using a sphere modeling tool and converted into a sheet. The parameter cells per wavelength was set to 5.25 in general mesh properties which led to a mesh grid of 500 triangular elements. The Integral equation solver was chosen and the

number of requested modes was set to 16. It is worth noting that regardless of the choice of number of frequency samples in CMA accuracy settings, CST-MWS always used 1001 frequency samples.

## B.D CEM One Setup

CEM One (2015.2, [193]) setting was as follows: a mesh grid was imported using the Nastran file format [186]. The impedance matrix was obtained by the "Save System Matrix" in the Final Output Parameters. Quadrature order was set in a *.dat file as:

```
#RUMSEY
simple 3 6
double 3 6
```

The first number represents the quadrature order for far elements and the second number represents the quadrature order for singularities. The impedance matrix was saved using a `ncdump` command in the E-Field command Prompt.

## B.E AToM Setup

AToM (pre-product ver.) setting was as follows: a mesh grid was imported using the Nastran file format [186]. The number of modes was set manually to 100 for Test #2 (the `eigs` routine was used) and kept as the maximum for the other tests (the `eig` routine). In AToM, RWG basis functions with the Galerkin procedure are adapted [44]. The Gaussian quadrature is implemented according to [187] and singularity treatment is implemented from [174]. The tracking of the CMs follows [69], including some recently added adaptive strategies [70]. Since AToM is written in Matlab, no other import procedures were needed.

## Acknowledgement

The authors would like to thank Vladimir Sedenka from BUT and Michal Masek from CTU in Prague for implementing the method of moments and characteristic modes solvers within the AToM package, and would also like to thank to Gerhard Kristensson from Lund University for a fruitful discussion concerning separable systems, Kurt Schab from NC State University, Doruk Tayli from Lund University and Jasmin Music from WIPL-D for providing the impedance matrices.

# C | Dissipation Factors of Spherical Current Modes on Multiple Spherical Layers

**Published as:** **V. Losenicky**, L. Jelinek, M. Capek, and M. Gustafsson, "Dissipation Factors of Spherical Current Modes on Multiple Spherical Layers," *IEEE Transactions on Antennas and Propagation*, vol. 66, no. 9, pp. 4948–4952, Sept. 2018, DOI: 10.1109/TAP.2018.2841408.

**Abstract**— Radiation efficiencies of modal current densities distributed on a spherical shell are evaluated in terms of dissipation factor. The presented approach is rigorous, yet simple and straightforward, leading to closed-form expressions. The same approach is utilized for a two-layered shell and the results are compared with other models existing in the literature. Discrepancies in this comparison are reported and reasons are analyzed. Finally, it is demonstrated that radiation efficiency potentially benefits from the use of internal volume which contrasts with the case of the radiation Q-factor.

**Index terms:** Radiation efficiency, Antenna theory, Optimization methods

## C.1 Introduction

The fundamental bounds on radiation efficiency have become increasingly interesting in recent years [102, 103, 119] as low radiation efficiency, together with a high radiation Q-factor presents a serious performance bottleneck for all electrically small antenna designs [36].

Similar to fundamental bounds on radiation Q-factor, fundamental bounds on radiation efficiency were first approached using the example of a spherical shell. The reason is twofold. First, the mathematics of spherical modes is analytically tractable. Second, it has been assumed [102] that, analogous to radiation Q-factor, the best radiation efficiency belongs to surface spherical modes.

The major purpose of this communication is to extend the study presented in [102] by providing a full-wave treatment of multilayer scenarios and to provide evidence that the surface spherical currents do not form a lower bound to the dissipation factor of a general volumetric radiator. Considering the practical demand on resonance

and the fact that loss-less external tuning is unreachable [102, 103, 119, 196], here, attention is primarily paid to self-resonant current densities, and the externally tuned results are considered only as intermediate products. All analytical results are verified with full-wave numerical calculations.

The communication is organized as follows. In Section C.2, the lowest dissipation factor for a single spherical shell is derived and compared with existing results. The model is generalized to two spherical layers in Section C.3, and to multiple layers in Section C.4. The communication is concluded in Section C.5.

## C.2 Dissipation factor of a single spherical layer

This section reformulates the results presented in [102] by directly manipulating vector spherical waves [48]. Some discrepancies in the model used in [102] are also indicated.

It is possible to show [81] that, within a time-harmonic steady state, electric field $\boldsymbol{E}$ and surface current density $\boldsymbol{J}$, corresponding to the modes of a spherical layer of radius $a$, read

$$\boldsymbol{E}_{mn}^{\mathrm{TE}} = -Z_0\,\zeta_n\,(ka)\,\psi_n'\,(ka)\,\boldsymbol{M}_{mn}, \tag{C.1}$$

$$\boldsymbol{E}_{mn}^{\mathrm{TM}} = Z_0\,\psi_n\,(ka)\,\zeta_n'\,(ka)\,\boldsymbol{N}_{mn}, \tag{C.2}$$

$$\boldsymbol{J}_{mn}^{\mathrm{TE}} = \hat{\boldsymbol{r}} \times \boldsymbol{N}_{mn}, \tag{C.3}$$

$$\boldsymbol{J}_{mn}^{\mathrm{TM}} = \hat{\boldsymbol{r}} \times \boldsymbol{M}_{mn}, \tag{C.4}$$

where

$$\psi_n\,(x) = x\mathrm{j}_n\,(x)\,, \tag{C.5}$$

$$\chi_n\,(x) = -x\mathrm{y}_n\,(x)\,, \tag{C.6}$$

$$\zeta_n\,(x) = x\mathrm{h}_n^{(2)}\,(x) = \psi_n\,(x) + \mathrm{j}\chi_n\,(x)\,, \tag{C.7}$$

are Riccati-Bessel functions, the symbol $'$ denotes differentiation, $Z_0$ is the free-space impedance, $k$ is the free-space wavenumber, $\mathrm{j}_n$, $\mathrm{y}_n$ and $\mathrm{h}_n^{(2)}$ are the spherical Bessel's functions of order $n$ [197], functions $\boldsymbol{M}$ and $\boldsymbol{N}$ are spherical vector waves defined in [81] with Bessel's function $\mathrm{j}_n$ inserted, and $\hat{\boldsymbol{r}}$ is the unit vector pointing in the radial direction. Electric field $\boldsymbol{E}_{mn}^{\mathrm{TE/TM}}$ and current density $\boldsymbol{J}_{mn}^{\mathrm{TE/TM}}$ also depend on spherical angular variables, but this dependence is of no relevance in this paper.

In order to evaluate radiation efficiency $\eta$ of modal current distributions, this paper uses dissipation factor $\delta$ [88] defined via $\eta = 1/\,(1+\delta)$. Dissipation factor is thus the ratio of the cycle mean power lost by conduction and cycle mean power lost by radiation.

In order to evaluate dissipation factors of surface current distributions, the complex power [180]

$$P_{\mathrm{rad}} + \mathrm{j}P_{\mathrm{react}} = -\frac{1}{2}\int\limits_S \boldsymbol{J}^* \cdot \boldsymbol{E}\,\mathrm{d}S \tag{C.8}$$

and cycle mean lost power

$$P_{\mathrm{lost}} = \frac{R_{\mathrm{s}}}{2}\int\limits_S \boldsymbol{J}^* \cdot \boldsymbol{J}\,\mathrm{d}S \tag{C.9}$$

are needed, where $^*$ denotes complex conjugation, and $R_\mathrm{s}$ denotes surface resistance (homogeneously distributed over the surface $S$). For current densities flowing on highly conducting bodies, a surface resistance model $R_\mathrm{s} = 1/(\sigma d)$ can be assumed, with $d$ being an effective penetration distance of the field into the conductor. For electrically thick conductors, $d$ can be put equal to the penetration depth [85].

In line with [102] and considering a major cost of resonance tuning to radiation efficiency [119] let us also prepare the grounds to form a resonant combination of selected spherical modes. To that point suppose a current density

$$\boldsymbol{J} = \boldsymbol{J}^\mathrm{e} + \alpha \boldsymbol{J}^\mathrm{m} \tag{C.10}$$

with tuning coefficient

$$|\alpha|^2 = -\frac{P^\mathrm{e}_\mathrm{react}}{P^\mathrm{m}_\mathrm{react}} \tag{C.11}$$

is formed with $\boldsymbol{J}^\mathrm{e}$ and $\boldsymbol{J}^\mathrm{m}$ being capacitative and inductive (excess electric or magnetic energy) spherical modes (C.3), (C.4), and $P^\mathrm{e}_\mathrm{react}$, $P^\mathrm{m}_\mathrm{react}$ being the corresponding reactive powers (C.8). Owing to the orthogonality of spherical modes [81], the current density (C.10) is self-resonant with $P_\mathrm{react} = 0$.

The dissipation factor $\delta$, corresponding to the current density (C.10), reads

$$\delta = \frac{P_\mathrm{lost}}{P_\mathrm{rad}} = \frac{P^\mathrm{e}_\mathrm{lost} + |\alpha|^2 P^\mathrm{m}_\mathrm{lost}}{P^\mathrm{e}_\mathrm{rad} + |\alpha|^2 P^\mathrm{m}_\mathrm{rad}} = \frac{\delta^\mathrm{e} - \dfrac{\lambda^\mathrm{e}}{\lambda^\mathrm{m}}\delta^\mathrm{m}}{1 - \dfrac{\lambda^\mathrm{e}}{\lambda^\mathrm{m}}}, \tag{C.12}$$

where mode orthogonality has once more been employed and where normalized reactances

$$\lambda^{\mathrm{e/m}} = \frac{P^{\mathrm{e/m}}_\mathrm{react}}{P^{\mathrm{e/m}}_\mathrm{rad}}. \tag{C.13}$$

were defined.

At small electrical sizes, where bounds on dissipation are of interest, the capacitive modes $^\mathrm{e}$ are the spherical TM modes, while inductive modes $^\mathrm{m}$ are the spherical TE modes. The last step prior to evaluation of (C.12) is thus to find the dissipation factors $\delta_n^{\mathrm{TE/TM}}$. The substitution of (C.1)–(C.4) into (C.8) and (C.9) leads to

$$\delta^\mathrm{TE}_{\circ,n} = \frac{R_\mathrm{s}}{Z_0} \frac{1}{\left(\psi_n\left(ka\right)\right)^2}, \tag{C.14}$$

$$\delta^\mathrm{TM}_{\circ,n} = \frac{R_\mathrm{s}}{Z_0} \frac{1}{\left(\psi'_n\left(ka\right)\right)^2}, \tag{C.15}$$

and to the expressions for the normalized reactances

$$\lambda^\mathrm{TE}_{\circ,n} = \frac{\chi_n\left(ka\right)}{\psi_n\left(ka\right)}, \tag{C.16}$$

$$\lambda^\mathrm{TM}_{\circ,n} = \frac{\chi'_n\left(ka\right)}{\psi'_n\left(ka\right)}, \tag{C.17}$$

which are equal to the characteristic numbers of a perfectly conducting spherical layer [75]. Subindex $\circ$ in (C.14)–(C.17) denotes quantities corresponding to a single spherical layer.

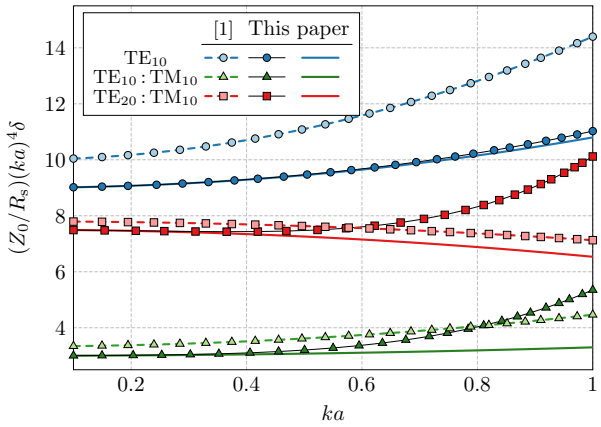


**Figure C.1:** Comparison of results (14), (16) and (19) from [102] with corresponding results of this paper. A comparison of the asymptotic (solid line) and full-wave (solid line with marks) expressions derived in this paper is also shown. The results correspond to a single spherical layer. The dissipation factors originating from [102] were multiplied by a factor of two, since [102] originally assumed two infinitesimally spaced resistive layers.

The dissipation factor (C.12) of any resonant combination of two spherical modes on a single spherical layer can easily be evaluated by substituting (C.14)–(C.17) into (C.12).

A direct comparison with dissipation factors evaluated in [102] reveals that the dissipation factors evaluated above are approximately two times higher. The reason for this discrepancy is the assumption[1] made in [102] that the spherical shell is composed of an inner and outer surface, both exhibiting the same surface resistance $R_s$. Assuming that the radial distance between the layers is negligible with respect to wavelength, it is easy to prove that such a configuration leads exactly to two times lower dissipation factors when compared to a single layer[2]. The reason is that the radiated power increases four times (due to cross terms in the $\boldsymbol{E} \cdot \boldsymbol{J}^*$ product), while losses increase only by a factor of two (having no cross terms in the $\boldsymbol{J} \cdot \boldsymbol{J}^*$ product). The mathematical proof is given in the next section.

Taking into account the above-mentioned factor of two (multiplying the results of [102] by two), the comparison of results derived here and the results derived in [102] is shown in Fig. C.1 and, simultaneously, in Table C.1, adopting the naming convention from [102]. The results presented here coincide with those derived in [103] and are well approximated by the results derived in [102]. With respect to the comparison it is also important to note a considerable difference between asymptotic formulas and full wave results which, in the $\mathrm{TM}_{10} : \mathrm{TE}_{10}$ case, reaches a 20 % error rate at $ka = 0.8$ and grows with increasing electrical size.

[1] We would like to thank C. Pfeiffer for pointing this out to us during a private discussion.

[2] The two-layer scenario can be understood as a transformation $d \to 2d$ within the surface resistance model $R_s = 1/(\sigma d)$ which leads to $R_s \to R_s/2$ and thus to two times smaller dissipation factors according to (C.14) and (C.15).

**Table C.1:** Comparison of asymptotic formulas for dissipation factor $\delta$ normalized by $Z_0/R_\mathrm{s}$ resulting from [102] and from this paper. The results correspond to a single spherical layer.

| $(Z_0/R_\mathrm{s})\,\delta$ | Paper [102] multiplied by 2 | This paper |
|---|---|---|
| $\mathrm{TE}_{10}$ | $\dfrac{10}{(ka)^4}+\dfrac{22}{5\,(ka)^2}$ | $\dfrac{9}{(ka)^4}+\dfrac{9}{5\,(ka)^2}$ |
| $\mathrm{TM}_{10}:\mathrm{TE}_{10}$ | $\dfrac{10}{3\,(ka)^4}+\dfrac{34}{30\,(ka)^2}$ | $\dfrac{3}{(ka)^4}+\dfrac{3}{10\,(ka)^2}$ |
| $\mathrm{TM}_{10}:\mathrm{TE}_{20}$ | $\dfrac{78}{10\,(ka)^4}-\dfrac{94}{140\,(ka)^2}$ | $\dfrac{15}{2\,(ka)^4}-\dfrac{27}{28\,(ka)^2}$ |

### C.2.1 A Note on Non-Resonant Current Distributions

The dissipation factors presented in Fig. C.1 assume resonant current distributions due to the major dissipation cost of resonance tuning [119]. Nevertheless, the non-resonant dissipation factors (C.14), (C.15) are also of importance. As an example, these analytical results can be used to validate more general dissipation bounds, such as those presented in [94]. In particular, for a single spherical surface the results shown in [94, Eq. 18, version 5] suggest $(Z_0/R_\mathrm{s})\,\delta = 6/\,(2ka)^2$, while the first-order asymptotic expansion of (C.15) gives $(Z_0/R_\mathrm{s})\,\delta = 9/\,(2ka)^2$ for the lowest TM mode. The bound presented in [94] is thus rather conservative for a spherical shell. It is also important to notice that, for small electrical sizes, non-resonant electric-dipole-like dissipation factors scale as $1/\,(ka)^2$, while resonant dissipation factors scale as $1/\,(ka)^4$, see [119] for a more general exposition of this phenomenon

## C.3 Dissipation factor of two spherical layers

The reduction of the dissipation factor by the specific composition of two resistive layers evokes the question of the general behavior of this setup. Specifically, assume that when forming a resonant current distribution (C.10), its constituents are yet another combination of spherical modes on two distinct layers of radius $a$ and radius $b < a$. The capacitive current will be formed as

$$\boldsymbol{J}^\mathrm{e} = \boldsymbol{J}^\mathrm{e}_a + \beta^\mathrm{e}\boldsymbol{J}^\mathrm{e}_b \tag{C.18}$$

and the inductive current will be formed as

$$\boldsymbol{J}^\mathrm{m} = \boldsymbol{J}^\mathrm{m}_a + \beta^\mathrm{m}\boldsymbol{J}^\mathrm{m}_b, \tag{C.19}$$

where it is assumed that currents of the same type (capacitive or inductive) are always formed by the same spherical mode. On the contrary, currents $\boldsymbol{J}^\mathrm{e}$ and $\boldsymbol{J}^\mathrm{m}$ are always formed by two distinct spherical modes and are thus orthogonal with respect to complex power as well as lost power. Therefore, formula (C.12) also remains valid in this case.

Dissipation factors and normalized reactances corresponding to (C.18) and (C.19) read

$$\delta_{\circledcirc,n}^{\mathrm{TE}} = \frac{AB + \left|\beta^{\mathrm{TE}}\right|^2 \frac{A}{B}}{AB + 2\mathrm{Re}\left[\beta^{\mathrm{TE}}\right] + \frac{\left|\beta^{\mathrm{TE}}\right|^2}{AB}} \delta_{\circ,n}^{\mathrm{TE}}, \tag{C.20}$$

$$\delta_{\circledcirc,n}^{\mathrm{TM}} = \frac{AB + \left|\beta^{\mathrm{TM}}\right|^2 \frac{B}{A}}{AB + 2\mathrm{Re}\left[\beta^{\mathrm{TM}}\right] + \frac{\left|\beta^{\mathrm{TM}}\right|^2}{AB}} \delta_{\circ,n}^{\mathrm{TM}}, \tag{C.21}$$

$$\lambda_{\circledcirc,n}^{\mathrm{TE}} = \frac{AB + 2\mathrm{Re}\left[\beta^{\mathrm{TE}}\right] + \frac{\left|\beta^{\mathrm{TE}}\right|^2}{CB}}{AB + 2\mathrm{Re}\left[\beta^{\mathrm{TE}}\right] + \frac{\left|\beta^{\mathrm{TE}}\right|^2}{AB}} \lambda_{\circ,n}^{\mathrm{TE}}, \tag{C.22}$$

$$\lambda_{\circledcirc,n}^{\mathrm{TM}} = \frac{AB + 2\mathrm{Re}\left[\beta^{\mathrm{TM}}\right] + \frac{\left|\beta^{\mathrm{TM}}\right|^2}{AD}}{AB + 2\mathrm{Re}\left[\beta^{\mathrm{TM}}\right] + \frac{\left|\beta^{\mathrm{TM}}\right|^2}{AB}} \lambda_{\circ,n}^{\mathrm{TM}}, \tag{C.23}$$

where

$$\begin{aligned} A &= \frac{\psi_n(ka)}{\psi_n(kb)}, \quad B = \frac{\psi_n'(ka)}{\psi_n'(kb)}, \\ C &= \frac{\chi_n(ka)}{\chi_n(kb)}, \quad D = \frac{\chi_n'(ka)}{\chi_n'(kb)}, \end{aligned} \tag{C.24}$$

and where the $\circledcirc$ symbol denotes quantities corresponding to two spherical layers.

As an example, the results of (C.20) for a $\mathrm{TE}_{10}$ mode are depicted in Fig. C.2 and Fig. C.3. A comparison of the curves in Fig. C.2 and the curves in Fig. C.1 shows that irrespective of ratio $b/a$, the $\mathrm{TE}_{10}$ current distribution on two spherical layers always results (for a specific $\beta^{\mathrm{TE}}$) in a lower dissipation factor than that of a single spherical layer[3]. The optimal values of $\beta^{\mathrm{TE}}$ and $\beta^{\mathrm{TM}}$ are solutions to

$$\left(\beta_{\mathrm{opt}}^{\mathrm{TE}}\right)^2 + \beta_{\mathrm{opt}}^{\mathrm{TE}} \frac{B}{A}\left(A^2 - 1\right) - B^2 = 0, \tag{C.25}$$

$$\left(\beta_{\mathrm{opt}}^{\mathrm{TM}}\right)^2 + \beta_{\mathrm{opt}}^{\mathrm{TM}} \frac{A}{B}\left(B^2 - 1\right) - A^2 = 0. \tag{C.26}$$

The frequency sweep corresponding to the same scenario in Fig. C.2, but with optimal $\beta^{\mathrm{TE}}$, is shown in Fig. C.3. It can be observed that the reduction of dissipation factor for the two-layer scenario is almost independent of electrical size.

The attention is now turned to the lowest dissipation factor for the two-layer scenario. Drawing an analogy with Section C.2, the lowest dissipation factor is

[3]Notice that two infinitesimally spaced spherical layers assumed in [102] correspond to $A = B = C = D = \beta^{\mathrm{TE/TM}} = 1$ and thus exactly to two times lower dissipation factors in comparison to a single layer scenario.

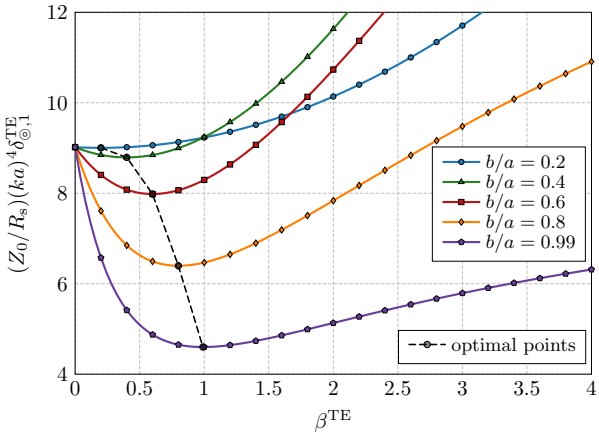


**Figure C.2:** Normalized dissipation factor corresponding to a $TE_{10}$ mode distributed on two spherical layers of radius $a$ and radius $b < a$. The results correspond to electrical size $ka = 0.1$. A curve showing the minima of the dissipation factors is also shown.

assumed to be formed by a resonant combination of $TE_{10}$ and $TM_{10}$ modes. When composing this resonant combination, according to (C.10) in the two layer scenario, a first thought could be to set $\beta^{TE}$ and $\beta^{TM}$ to their optimal values according to (C.25) and (C.26), then form a resonant combination. This is, however, not an optimal choice as is shown in Fig. C.4. In the two-layer scenario, the normalized reactances $\lambda^{e/m}$ are also functions of $\beta^{TE}$ and $\beta^{TM}$ making the minimum of the total dissipation factor an optimization problem with two variables. Depending on electrical size $ka$ and ratio $b/a$ the optimal values can deviate significantly from those predicted by (C.25) and (C.26) for stand alone TM and TE modes, see Fig. C.4.

The optimal resonant combination $TM_{10} : TE_{10}$, shown in Fig. C.4, was proposed in [102] as a current density with the lowest dissipation factor from all free-space current distributions. An inductive extension of the analysis shown in this section, however, suggests that the addition of more layers should reduce dissipation even further.

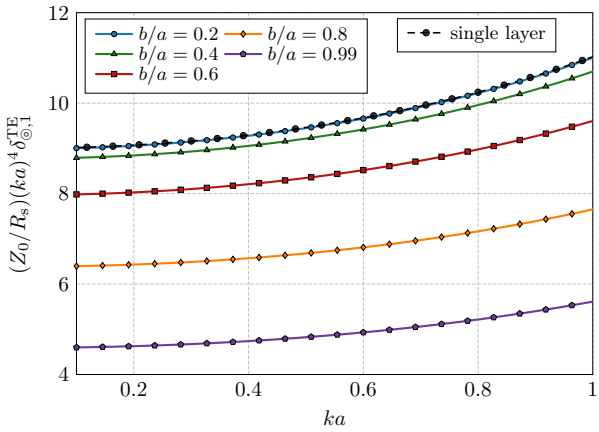


**Figure C.3:** Normalized dissipation factor corresponding to a $\mathrm{TE}_{10}$ mode distributed on two spherical layers of radius $a$ and radius $b < a$. Optimal values of $\beta^{\mathrm{TE}}$ were used.

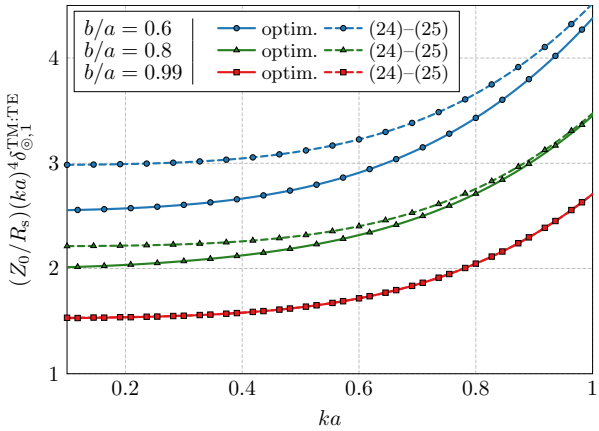


**Figure C.4:** Normalized dissipation factor corresponding to a $\mathrm{TM}_{10} : \mathrm{TE}_{10}$ combination distributed on two spherical layers of radius $a$ and radius $b < a$. Optimal values of $\beta^{\mathrm{TE}}$, $\beta^{\mathrm{TM}}$ were either evaluated according to (C.25) and (C.26) or by two variable optimization.

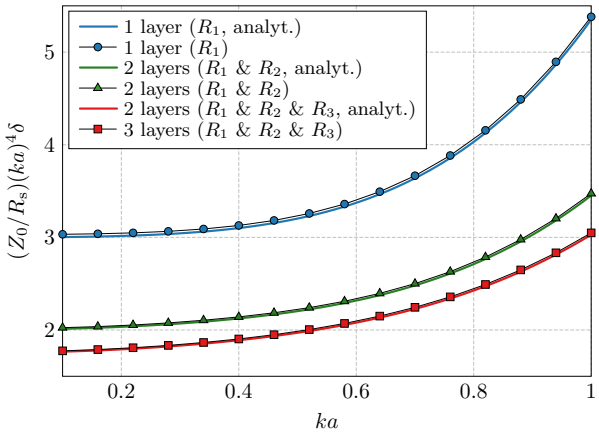


**Figure C.5:** Normalized dissipation factors of the optimal self-resonant current densities distributed on one, two and three spherical layers of the same surface resistance. The radii of the layers $R_1 = a$, $R_2 = 0.8a$, and $R_3 = 0.6a$ have been used. The analytical data correspond to the resonant $\mathrm{TM}_{10} : \mathrm{TE}_{10}$ combination.

## C.4 Dissipation factor of multiple layers

The case of more than two spherical layers is a straightforward extension of (C.20)–(C.23). The number of terms in complex power (C.8), however, increases and explicit relations become too long. It is also important to realize that the optimization of coupling parameters $\beta$ will attain more dimensions. Last, but not least, it is important to realize that we did not prove that the resonant combination of $\mathrm{TM}_{10} : \mathrm{TE}_{10}$ modes on multiple spherical layers is the global minimizer to the resonant dissipation factor within spherical geometry. Due to the preceding reasons, this Section will compare a purely numerical approach with the analytical treatment.

The numerical method used here, and described in [101, 104, 107], is able to find the global minimizer for an arbitrary surface current support. The results for one, two, and three spherical shells are shown in Fig. C.5 and compared to the analytical resonant combination of the $\mathrm{TM}_{10} : \mathrm{TE}_{10}$ modes. Good agreement of the numerical and analytical results in Fig. C.5 can be observed. A slight discrepancy can be attributed to the problem of comparing data corresponding to a perfect spherical surface with its triangularized (570 triangles per layer) counterpart. This allows us to finish this communication with the following statements:

- The addition of more spherical layers systematically reduces the dissipation factor, although with significantly diminishing returns;
- The resonant combination of $\mathrm{TM}_{10} : \mathrm{TE}_{10}$ modes seems to give the lowest dissipation factor from all resonant current distributions, even in the multilayer scenario;
- The hypothesis from [102] that the bound on the tuned dissipation factor is presented by a resonant combination of $\mathrm{TM}_{10}$ and $\mathrm{TE}_{10}$ spherical currents distributed on a single spherical surface is not valid.

It is worth noting that the last point is strongly connected to the optimization task addressed in [198] and [96] in which it is shown that a volumetric current density with the angular distribution of the dominant spherical mode and radial dependence of the spherical Bessel function exhibits a lower dissipation factor than the purely surface current distribution of the same angular dependence.

## C.5 Conclusion

Minimum dissipation factors corresponding to current densities distributed on multiple spherical layers have been found in an analytic or semi-analytic manner and have been proven to be valid by using a full-wave numerical method. Results corresponding to one and two spherical layers were also compared with existing works.

It has been demonstrated that spherical modes can always be distributed on two spherical layers so as to lead to a smaller dissipation factor than that offered by a single spherical layer. This holds irrespective of electrical size or the ratio of the layer radii and does not depend whether a non-resonant or resonant combination of modes is formed. Moreover, the addition of more layers reduces the dissipation factor even further which indicates that a volumetric current density should be optimized in order to obtain a bound on dissipation factor. Since, however, radial currents are ineffective in producing radiation, the collection of separated spherical layers will lead to a solution close to the volumetric bound. Consequently, for a realistic antenna operating in free space environments, the surface currents can be considered as an approximate bound. However, for an antenna radiating in the presence of volumetric material objects, the volumetric current densities should be taken into account, since the surface current bound could be too pessimistic.

# D Accurate and Efficient Evaluation of Characteristic Modes

**Published as:** D. Tayli, M. Capek, L. Akrou, **V. Losenicky**, L. Jelinek, and M. Gustafsson, "Accurate and Efficient Evaluation of Characteristic Modes," *IEEE Transactions on Antennas and Propagation*, vol. 66, no. 12, pp. 7066–7075, Dec. 2018, DOI: 10.1109/TAP.2018.2869642.

**Abstract**— A new method to improve the accuracy and efficiency of characteristic mode (CM) decomposition for perfectly conducting bodies is presented. The method uses the expansion of the Green dyadic in spherical vector waves. This expansion is utilized in the method of moments (MoM) solution of the electric field integral equation (EFIE) to factorize the real part of the impedance matrix. The factorization is then employed in the computation of CMs, which improves the accuracy as well as the computational speed. An additional benefit is a rapid computation of far fields. The method can easily be integrated into existing MoM solvers. Several structures are investigated, illustrating the improved accuracy and performance of the new method.

**Index terms:** Antenna theory, convergence of numerical methods, eigenvalues and eigenfunctions, electromagnetic theory, numerical analysis

## D.1 Introduction

The method of moments (MoM) solution to electromagnetic field integral equations was introduced by Harrington [24] and has prevailed as a standard in solving open (radiating) electromagnetic problems [199]. While memory-demanding, MoM represents operators as matrices (notably the impedance matrix [24]) allowing for direct inversion and modal decompositions [200]. The latter option is becoming increasingly popular, mainly due to characteristic mode (CM) decomposition [9], a leading formalism in antenna shape and feeding synthesis [142, 157], determination of optimal currents [28, 64], and performance evaluation [155].

Utilization of CM decomposition is especially efficient when dealing with electrically small antennas [201], particularly if they are made solely of perfect electric conductor (PEC), for which only a small number of modes are needed to describe their radiation behavior. Yet, the real part of the impedance matrix is indefinite as it is computed with finite precision [75, 134]. The aforementioned deficiency is resolved

in this paper by a two-step procedure. First, the real part of the impedance matrix is constructed using spherical wave expansion of the dyadic Green function [48]. This makes it possible to decompose the real part of the impedance matrix as a product of a spherical modes projection matrix with its hermitian conjugate. The second step consists of reformulating the modal decomposition so that only the standalone spherical modes projection matrix is involved preserving the numerical dynamics[1].

The proposed method significantly accelerates the computation of CMs as well as of the real part of the impedance matrix. Moreover, it is possible to recover CMs using lower precision floating point arithmetic, which reduces memory use and speeds up arithmetic operations if hardware vectorization is exploited [200]. An added benefit is the efficient computation of far field patterns using spherical vector harmonics.

The projection on spherical waves in the proposed method introduces several appealing properties. First is an easy monitoring of the numerical dynamics of the matrix, since the different spherical waves occupy separate rows in the projection matrix. Second is the possibility to compute a positive semidefinite impedance matrix, which plays important role in an optimal design [28, 41]. A final benefit is the superposition of modes. [142].

The paper is organized as follows. The construction of the impedance matrix using classical procedure is briefly reviewed in Section D.2.1 and the proposed procedure is presented in Section D.2.2. Numerical aspects of evaluating the impedance matrix are discussed in Section D.2.3. In Section D.3, the spherical modes projection matrix is utilized to reformulate modal decomposition techniques, namely the evaluation of radiation modes in Section D.3.1 and CMs in Section D.3.2. These two applications cover both the standard and generalized eigenvalue problems. The advantages of the proposed procedure are demonstrated on a series of practical examples in this section. Various aspects of the proposed method are discussed in Section D.4 and the paper is concluded in Section D.5.

## D.2 Evaluation of Impedance Matrix

This paper investigates mode decompositions for PEC structures in free space. The time-harmonic quantities under the convention $\boldsymbol{\mathcal{J}}(\boldsymbol{r},t) = \mathrm{Re}\{\boldsymbol{J}(\boldsymbol{r},\omega)\exp(\mathrm{j}\omega t)\}$, with $\omega$ being the angular frequency, are used throughout the paper.

### D.2.1 Method of Moments Implementation of the EFIE

Let us consider the electric field integral equation (EFIE) [24] for PEC bodies, defined as

$$\mathcal{Z}(\boldsymbol{J}) = \mathcal{R}(\boldsymbol{J}) + \mathrm{j}\mathcal{X}(\boldsymbol{J}) = \hat{\boldsymbol{n}} \times (\hat{\boldsymbol{n}} \times \boldsymbol{E}), \tag{D.1}$$

with $\mathcal{Z}(\boldsymbol{J})$ being the impedance operator, $\boldsymbol{E}$ the incident electric field [180], $\boldsymbol{J}$ the current density, j the imaginary unit, and $\hat{\boldsymbol{n}}$ the unit normal vector to the PEC surface. The EFIE (D.1) is explicitly written as

$$\hat{\boldsymbol{n}} \times \boldsymbol{E}(\boldsymbol{r}_2) = \mathrm{j}kZ_0\hat{\boldsymbol{n}} \times \int_{\Omega} \mathbf{G}(\boldsymbol{r}_1,\boldsymbol{r}_2) \cdot \boldsymbol{J}(\boldsymbol{r}_1)\,\mathrm{d}A_1, \tag{D.2}$$

[1]The numerical dynamic is defined as the largest characteristic eigenvalue.

where $\boldsymbol{r}_2 \in \Omega$, $k$ is the wave number, $Z_0$ the free space impedance, and $\mathbf{G}$ the dyadic Green function for the electric field in free-space defined as [47, 48]

$$\mathbf{G}\left(\boldsymbol{r}_1, \boldsymbol{r}_2\right) = \left(\mathbf{1} + \frac{1}{k^2}\nabla\nabla\right) \frac{\mathrm{e}^{-\mathrm{j}k|\boldsymbol{r}_1 - \boldsymbol{r}_2|}}{4\pi\,|\boldsymbol{r}_1 - \boldsymbol{r}_2|} \tag{D.3}$$

where $\mathbf{1}$ is the identity dyadic, and $\boldsymbol{r}_1$, $\boldsymbol{r}_2$ are the source and observation points. The EFIE (D.2) is solved with the MoM by expanding the current density $\boldsymbol{J}\left(\boldsymbol{r}\right)$ into real-valued basis functions $\left\{\boldsymbol{\psi}_p\left(\boldsymbol{r}\right)\right\}$ as

$$\boldsymbol{J}\left(\boldsymbol{r}\right) \approx \sum_{p=1}^{N_\psi} I_p\, \boldsymbol{\psi}_p\left(\boldsymbol{r}\right) \tag{D.4}$$

and applying Galerkin testing procedure [47, 202]. The impedance operator $\mathcal{Z}\left(\boldsymbol{J}\right)$ is expressed as the impedance matrix $\mathbf{Z} = \mathbf{R} + \mathrm{j}\mathbf{X} = [Z_{pq}] \in \mathbb{C}^{N_\psi \times N_\psi}$, where $\mathbf{R}$ is the resistance matrix, and $\mathbf{X}$ the reactance matrix. The elements of the impedance matrix are

$$Z_{pq} = \mathrm{j}kZ_0 \int_\Omega \int_\Omega \boldsymbol{\psi}_p\left(\boldsymbol{r}_1\right) \cdot \mathbf{G}\left(\boldsymbol{r}_1, \boldsymbol{r}_2\right) \cdot \boldsymbol{\psi}_q\left(\boldsymbol{r}_2\right)\, \mathrm{d}A_1\, \mathrm{d}A_2. \tag{D.5}$$

### D.2.2 Spherical Wave Expansion of the Green Dyadic

The Green dyadic (D.3) that is used to compute the impedance matrix $\mathbf{Z}$ can be expanded in spherical vector waves as

$$\mathbf{G}\left(\boldsymbol{r}_1, \boldsymbol{r}_2\right) = -\mathrm{j}k \sum_\alpha \mathbf{u}_\alpha^{(1)}\left(k\boldsymbol{r}_<\right) \mathbf{u}_\alpha^{(4)}\left(k\boldsymbol{r}_>\right), \tag{D.6}$$

where $\boldsymbol{r}_< = \boldsymbol{r}_1$ and $\boldsymbol{r}_> = \boldsymbol{r}_2$ if $|\boldsymbol{r}_1| < |\boldsymbol{r}_2|$, and $\boldsymbol{r}_< = \boldsymbol{r}_2$ and $\boldsymbol{r}_> = \boldsymbol{r}_1$ if $|\boldsymbol{r}_1| > |\boldsymbol{r}_2|$. The regular and outgoing spherical vector waves [48, 183, 185, 203] are $\mathbf{u}_\alpha^{(1)}\left(k\boldsymbol{r}\right)$ and $\mathbf{u}_\alpha^{(4)}\left(k\boldsymbol{r}\right)$, see Appendix D.B. The mode index $\alpha$ for real-valued vector spherical harmonics is [185, 204]

$$\alpha\left(\tau, \sigma, m, l\right) = 2\left(l^2 + l - 1 + (-1)^s m\right) + \tau \tag{D.7}$$

with $\tau \in \{1, 2\}$, $m \in \{0, \ldots, l\}$, $l \in \{1, \ldots, L\}$, $s = 0$ for even azimuth functions ($\sigma = \mathrm{e}$), and $s = 1$ for odd azimuth functions ($\sigma = \mathrm{o}$). Inserting the expansion of the Green dyadic (D.6) into (D.5), the impedance matrix $\mathbf{Z}$ becomes

$$Z_{pq} = k^2 Z_0 \sum_\alpha \int_\Omega \int_\Omega \boldsymbol{\psi}_p\left(\boldsymbol{r}_1\right) \cdot \mathbf{u}_\alpha^{(1)}\left(k\boldsymbol{r}_<\right) \mathbf{u}_\alpha^{(4)}\left(k\boldsymbol{r}_>\right) \cdot \boldsymbol{\psi}_q\left(\boldsymbol{r}_2\right)\, \mathrm{d}A_1\, \mathrm{d}A_2. \tag{D.8}$$

For a PEC structure the resistive part of (D.8) can be factorized as

$$R_{pq} = k^2 Z_0 \sum_\alpha \int_\Omega \boldsymbol{\psi}_p\left(\boldsymbol{r}_1\right) \cdot \mathbf{u}_\alpha^{(1)}\left(k\boldsymbol{r}_1\right)\, \mathrm{d}A_1 \int_\Omega \mathbf{u}_\alpha^{(1)}\left(k\boldsymbol{r}_2\right) \cdot \boldsymbol{\psi}_q\left(\boldsymbol{r}_2\right)\, \mathrm{d}A_2, \tag{D.9}$$

where $\mathbf{u}_\alpha^{(1)}(k\boldsymbol{r}) = \mathrm{Re}\{\mathbf{u}_\alpha^{(4)}(k\boldsymbol{r})\}$ is used. Reactance matrix, $\mathbf{X}$, cannot be factorized in a similar way as two separate spherical waves occur.

The resistance matrix can be written in matrix form as

$$\mathbf{R} = \mathbf{S}^{\mathrm{T}}\mathbf{S}, \tag{D.10}$$

where $^{\mathrm{T}}$ is the matrix transpose. Individual elements of the matrix $\mathbf{S}$ are

$$S_{\alpha p} = k\sqrt{Z_0}\int_{\Omega} \boldsymbol{\psi}_p(\boldsymbol{r}) \cdot \mathbf{u}_\alpha^{(1)}(k\boldsymbol{r})\,\mathrm{d}A \tag{D.11}$$

and the size of the matrix $\mathbf{S}$ is $N_\alpha \times N_\psi$, where

$$N_\alpha = 2L(L+2) \tag{D.12}$$

is the number of spherical modes and $L$ the highest order of spherical mode (see Appendix D.B). For complex-valued vector spherical harmonics [185], the transpose $^{\mathrm{T}}$ in (D.10) is replaced with the Hermitian transpose $^{\mathrm{H}}$. The individual integrals in (D.8) are, in fact, related to the T-matrix method [25, 203], where the incident and scattered electric fields are expanded using regular and outgoing spherical vector waves, respectively. The factorization (D.6) is also used in vector fast multipole algorithm [205].

The radiated far-field $\boldsymbol{F}(\hat{\boldsymbol{r}})$ can conveniently be computed using spherical vector harmonics

$$\boldsymbol{F}(\hat{\boldsymbol{r}}) = \frac{1}{k}\sum_{\alpha} \mathrm{j}^{l-\tau+2} f_\alpha \mathbf{Y}_\alpha(\hat{\boldsymbol{r}}), \tag{D.13}$$

where $\mathbf{Y}_\alpha(\hat{\boldsymbol{r}})$ are the spherical vector harmonics, see Appendix D.B. The expansion coefficients $f_\alpha$ are given by

$$[f_\alpha] = \mathbf{SI}, \tag{D.14}$$

where the column matrix $\mathbf{I}$ contains the current density coefficients $I_p$. The total time-averaged radiated power of a lossless antenna can be expressed as a sum of expansion coefficients

$$P_{\mathrm{rad}} \approx \frac{1}{2}\mathbf{I}^{\mathrm{H}}\mathbf{RI} = \frac{1}{2}|\mathbf{SI}|^2 = \frac{1}{2}\sum_{\alpha}|f_\alpha|^2. \tag{D.15}$$

### D.2.3 Numerical Considerations

The spectrum of the matrices $\mathbf{R}$ and $\mathbf{X}$ differ considerably [28, 75]. The eigenvalues of the $\mathbf{R}$ matrix decrease exponentially and the number of eigenvalues are corrupted by numerical noise, while this is not the case for the matrix $\mathbf{X}$. As a result, if the matrix $\mathbf{R}$ is used in an eigenvalue problem, only a few modes can be extracted. This major limitation can be overcome with the use of the matrix $\mathbf{S}$ in (D.11), whose elements vary several order of magnitude, as the result of the increased order of spherical modes with increasing row number. If the matrix $\mathbf{R}$ is directly computed with the matrix product (D.10) or equivalently from matrix produced by (D.5) small values are truncated due to floating-point arithmetic[2] [206, 207]. Subsequently, the

[2] As an example to the loss of significance in double precision arithmetic consider the sum $1.0 + 1 \times 10^{-30} = 1.0$.

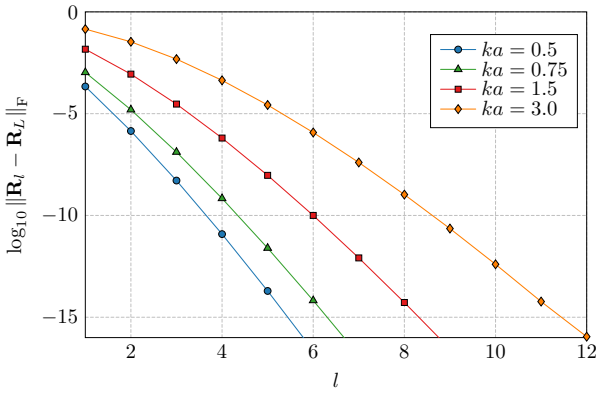


**Figure D.1:** Convergence of the matrix $\mathbf{R}_l = \mathbf{S}_l^{\mathrm{T}}\mathbf{S}_l$ to the matrix $\mathbf{R}_L = \mathbf{S}_L^{\mathrm{T}}\mathbf{S}_L$ on the rectangular plate (Example R2) for different order of spherical modes $l = \{1, \ldots, L\}$ and multiple electric sizes $ka \in \{0.5, 0.75, 1.5, 3.0\}$, with the highest spherical mode order $L = 12$. The superscript $^{\mathrm{F}}$ denotes the Frobenius norm. The convergence is computed with quadruple precision using the mpmath Python library [209].

spectrum of the matrix $\mathbf{R}$ should be computed from the matrix $\mathbf{S}$ as presented in Section D.3.

The matrix $\mathbf{S}$ also provides a low-rank approximation of the matrix $\mathbf{R}$, which is the result of the rapid convergence of regular spherical waves. In this paper, the number of used modes in (D.6) is truncated using a modified version of the expression in [208]

$$L = \lceil ka + 7\sqrt[3]{ka} + 3 \rceil, \tag{D.16}$$

where $L$ is the highest order of spherical mode, $a$ is the radius of the sphere enclosing the scatterer, and $\lceil . \rceil$ is the ceiling function. The resulting accuracy in all treated cases is satisfactory. The order of spherical modes can be modified to trade between accuracy and computational efficiency, where increasing $L$ improves the accuracy. Fig. D.1 shows the convergence of the matrix $\mathbf{R}$ for Example R2.

Substitution of the spherical vector waves, introduced in Section D.2.2, separates (D.5) into two separate surface integrals reducing computational complexity. Table D.1 presents computation times[3] of different matrices[4] $\mathbf{Z}$, $\mathbf{R}$, $\mathbf{S}$, and $\mathbf{S}^{\mathrm{T}}\mathbf{S}$ for the examples given in Table D.2. As expected, the matrix $\mathbf{Z}$ requires the most computational resources, as it includes both the matrix $\mathbf{R}$ and $\mathbf{X}$. The computation of the matrix $\mathbf{R}$ using MoM is faster than the matrix $\mathbf{Z}$ since the underlying integrals are regular. The computation of the matrix $\mathbf{R}$ using (D.10) takes the least amount of time for most of the examples. The computational gain is notable for structures with more degrees-of-freedom (d-o-f), $N_\psi$.

[3]Computations are done on a workstation with i7-3770 CPU @ 3.4 GHz and 32 GB RAM, operating under Windows 7.

[4]Computation time for the matrix $\mathbf{X}$ is omitted as it takes longer than the matrix $\mathbf{R}$, due to Green function singularity.

| Example | Time to assemble matrices in IDA (s) | | | |
|---|---|---|---|---|
| (see Table D.2) | $\mathbf{Z}$ | $\mathbf{R}$ | $\mathbf{S}$ | $\mathbf{R} = \mathbf{S}^{\mathrm{T}}\mathbf{S}$ |
| S1 | 2.58 | 0.09 | 0.009 | 0.011 |
| S4 | 14.2 | 1.78 | 0.039 | 0.083 |
| R3 | 11.1 | 1.11 | 0.035 | 0.068 |
| H1 | 200 | 54.5 | 0.236 | 1.66 |

**Table D.1:** Time to assemble matrices in IDA. Simulation setup for the examples in Table D.2, $N_q = 3$ and $L = 10$ ($N_\alpha = 240$), matrix multiplication $\mathbf{S}^{\mathrm{T}}\mathbf{S}$ is performed with dgemm from the Intel MKL library [210].

| Structure | Example | $ka$ | $N_\psi$ | $N_\alpha$ |
|---|---|---|---|---|
| Spherical shell Fig. 9 in [76] | S1 | 1/2 | 750 | 240 |
| | S2 | 1/2 | 750 | 880 |
| | S3 | 3/2 | 750 | 880 |
| | S4 | 1/2 | 3330 | 240 |
| | S5 | 1/2 | 3330 | 880 |
| Rectangular plate Fig. 10 in [76] ($L/W = 2$) | R1 | 1/2 | 199 | 510 |
| | R2 | 1/2 | 655 | 510 |
| | R3 | 1/2 | 2657 | 240 |
| | R4 | 1/2 | 2657 | 1920 |
| Helicopter | H1 | 1/2 | 18898 | 240 |
| | H2 | 7 | 18898 | 720 |

**Table D.2:** Summary of examples used throughout the paper, $ka$ is the electrical size, $N_\psi$ is the number of basis functions (D.4), and $N_\alpha$ is number of spherical modes calculated as (D.12). The order of the symmetric quadrature rule used to compute the non-singular integrals in (D.5) is $N_q = 3$ [187].

## D.3 Modal Decomposition With the Matrix S

Modal decomposition using the matrix $\mathbf{S}$ is applied to two structures; a spherical shell of radius $a$, and a rectangular plate of length $L$ and width $W = L/2$ [76], which are presented in Table D.2. Both structures are investigated for different number of d-o-f, RWG functions [44] are used as the basis functions $\boldsymbol{\psi}_p$. The matrices used in modal decomposition have been computed using in-house solvers Antenna Toolfox for MATLAB (AToM) [150] and Integrated Development toolset for Antennas (IDA) [162] (see Appendix D.A for details). Results from the commercial electromagnetic solver FEKO [152] are also presented for comparison. Computations that require a higher precision than the double precision arithmetic are performed using the mpmath Python library [209], and the Advanpix Matlab toolbox [194].

| Example | Number of properly calculated modes | | | | |
|---|---|---|---|---|---|
| | $\mathbf{RI} = \xi_n \mathbf{I}_n$ | | $\mathbf{XI}_n = \lambda_n \mathbf{RI}_n$ | | |
| (see Table D.2) | (D.17) | (D.19) | (D.20) | $\mathbf{R} = \mathbf{S}^{\mathrm{T}}\mathbf{S}$ | (D.24) |
| S2 | 59 | 284 | **70** (5) | 96 (6) | **284** (11) |
| S3 | 96 | 364 | **105** (6) | 197 (9) | **389** (13) |
| S5 | 59 | 311 | **70** (5) | 96 (6) | **306** (11) |
| R1 | 31 | 109 | **29** | 35 | **37** |
| R2 | 29 | 117 | **26** | 33 | **98** |
| R4 | 28 | 116 | **22** | 26 | **98** |

**Table D.3:** Comparison of the number of modes correctly found by the classical and the novel methods for examples listed in Table D.2. Columns 2–3 summarize the radiation modes and columns 4–6 summarize the CMs. Values in parentheses depicts the number of non-degenerated TM and TE modes found on spherical shell. The main outcome of the table, comparison of the CMs is highlighted by bold type.

### D.3.1 Radiation Modes

The eigenvalues for the radiation modes [56] are easily found using the eigenvalue problem

$$\mathbf{RI}_n = \xi_n \mathbf{I}_n, \tag{D.17}$$

where $\xi_n$ are the eigenvalues of the matrix $\mathbf{R}$, and $\mathbf{I}_n$ are the eigencurrents. The indefiniteness of the matrix $\mathbf{R}$ poses a problem in the eigenvalue decomposition (D.17) as illustrated in [28, 75]. In this paper we show that the indefiniteness caused by the numerical noise can be bypassed using the matrix $\mathbf{S}$. We start with the singular value decomposition (SVD) of the matrix $\mathbf{S}$

$$\mathbf{S} = \mathbf{U}\mathbf{\Lambda}\mathbf{V}^{\mathrm{H}}, \tag{D.18}$$

where $\mathbf{U}$ and $\mathbf{V}$ are unitary matrices, and $\mathbf{\Lambda}$ is a diagonal matrix containing singular values of matrix $\mathbf{S}$. Inserting (D.10), (D.18) into (D.17) and multiplying from the left with $\mathbf{V}^{\mathrm{H}}$ yields

$$\mathbf{\Lambda}^{\mathrm{H}}\mathbf{\Lambda}\widetilde{\mathbf{I}}_n = \xi_n \widetilde{\mathbf{I}}_n, \tag{D.19}$$

where the eigenvectors are rewritten as $\widetilde{\mathbf{I}}_n \equiv \mathbf{V}^{\mathrm{H}}\mathbf{I}_n$, and the eigenvalues are $\xi_n = \Lambda_{nn}^2$. A comparison of procedure (D.17) and (D.19) is shown in Table D.3. For high order $n$, the classical procedure (D.17) with double numerical precision yields in unphysical modes with negative eigenvalues $\xi_n$ (negative radiated power) or with incorrect current profile (as compared to the use of quadruple precision). Using double precision, the number of modes which resemble physical reality (called "properly calculated modes" in Table D.3) is much higher[5] for the new procedure (D.19). It is also worth mentioning that the new procedure, by design, always gives positive eigenvalues $\xi_n$.

[5]Quantitatively, the proper modes in Table D.3 are defined as those having less than 5% deviation in eigenvalue $\xi_n$ as compared to the computation with quadruple precision.

### D.3.2 Characteristic Modes (CMs)

The generalized eigenvalue problem (GEP) with the matrix $\mathbf{R}$ on the right hand side, *i.e.*, serving as a weighting operator [179], is much more involved as the problem cannot be completely substituted by the SVD. Yet, the SVD of the matrix $\mathbf{S}$ in (D.18) plays an important role in CM decomposition.

The CM decomposition is defined as

$$\mathbf{X}\mathbf{I}_n = \lambda_n \mathbf{R}\mathbf{I}_n, \tag{D.20}$$

which is known to suffer from the indefiniteness of the matrix $\mathbf{R}$ [75], therefore delivering only a limited number of modes. The first step is to represent the solution in a basis of singular vectors $\mathbf{V}$ by substituting the matrix $\mathbf{R}$ in (D.20) as (D.10), with (D.18) and multiplying (D.20) from the left by the matrix $\mathbf{V}^{\mathrm{H}}$

$$\mathbf{V}^{\mathrm{H}}\mathbf{X}\mathbf{V}\mathbf{V}^{\mathrm{H}}\mathbf{I}_n = \lambda_n \mathbf{\Lambda}^{\mathrm{H}}\mathbf{\Lambda}\mathbf{V}^{\mathrm{H}}\mathbf{I}_n. \tag{D.21}$$

Formulation (D.21) can formally be expressed as a GEP with an already diagonalized right hand side [211]

$$\widetilde{\mathbf{X}}\widetilde{\mathbf{I}}_n = \lambda_n \widetilde{\mathbf{R}}\widetilde{\mathbf{I}}_n. \tag{D.22}$$

That is $\widetilde{\mathbf{X}} \equiv \mathbf{V}^{\mathrm{H}}\mathbf{X}\mathbf{V}$, $\widetilde{\mathbf{R}} \equiv \mathbf{\Lambda}^{\mathrm{H}}\mathbf{\Lambda}$, and $\widetilde{\mathbf{I}}_n \equiv \mathbf{V}^{\mathrm{H}}\mathbf{I}_n$.

Since the matrix $\mathbf{S}$ is in general rectangular, it is crucial to take into account cases where $N_\alpha < N_\psi$, (D.12). This is equivalent to a situation in which there are limited number of spherical projections to recover the CMs. Consequently, only limited number of singular values $\Lambda_{nn}$ exist. In such a case, the procedure similar to the one used in [134] should be undertaken by partitioning (D.22) into two linear systems

$$\widetilde{\mathbf{X}}\widetilde{\mathbf{I}} = \begin{pmatrix} \widetilde{\mathbf{X}}_{11} & \widetilde{\mathbf{X}}_{12} \\ \widetilde{\mathbf{X}}_{21} & \widetilde{\mathbf{X}}_{22} \end{pmatrix} \begin{pmatrix} \widetilde{\mathbf{I}}_{1n} \\ \widetilde{\mathbf{I}}_{2n} \end{pmatrix} = \begin{pmatrix} \lambda_{1n}\widetilde{\mathbf{R}}_{11}\widetilde{\mathbf{I}}_{1n} \\ \mathbf{0} \end{pmatrix}, \tag{D.23}$$

where $\widetilde{\mathbf{I}}_{1n} \in \mathbb{C}^{N_\alpha}$, $\widetilde{\mathbf{I}}_{2n} \in \mathbb{C}^{N_\psi - N_\alpha}$, and $N_\alpha < N_\psi$. The Schur complement is obtained by substituting the second row of (D.23) into the first row

$$\left(\widetilde{\mathbf{X}}_{11} - \widetilde{\mathbf{X}}_{12}\widetilde{\mathbf{X}}_{22}^{-1}\widetilde{\mathbf{X}}_{21}\right)\widetilde{\mathbf{I}}_{1n} = \lambda_{1n}\widetilde{\mathbf{R}}_{11}\widetilde{\mathbf{I}}_{1n} \tag{D.24}$$

with expansion coefficients of CMs defined as

$$\widetilde{\mathbf{I}}_n = \begin{pmatrix} \widetilde{\mathbf{I}}_{1n} \\ -\widetilde{\mathbf{X}}_{22}^{-1}\widetilde{\mathbf{X}}_{21}\widetilde{\mathbf{I}}_{1n} \end{pmatrix}. \tag{D.25}$$

As far as the matrices $\mathbf{U}$ and $\mathbf{V}$ in (D.18) are unitary, the decomposition (D.22) yields CMs implicitly normalized to

$$\widetilde{\mathbf{I}}_n^{\mathrm{H}}\widetilde{\mathbf{R}}\widetilde{\mathbf{I}}_m = \delta_{nm}, \tag{D.26}$$

which is crucial since the standard normalization cannot be used without decreasing the number of significant digits. In order to demonstrate the use of (D.24), various examples from Table D.2 are calculated and compared with the conventional approach (D.20).

The CMs of the spherical shell from Example S2 are calculated and shown as absolute values in logarithmic scale in Fig. D.2. It is shown that the number of the

CMs calculated by classical procedure (FEKO, AToM) is limited to the lower modes, especially considering the degeneracy $2l+1$ of the CMs on the spherical shell [75]. The number of properly found CMs is significantly higher when using (D.24) than the conventional approach (D.20) and the numerical dynamic is doubled. Notice that even (D.20), where the matrix $\mathbf{R}$ calculated from (D.10) yields slightly better results than the conventional procedure. This fact is confirmed in Fig. D.3 dealing with Example R2, where the multiprecision package Advanpix is used as a reference. The same calculation illustrates that the matrix $\mathbf{R}$ contains all information to recover the same number of modes as (D.24), but this can be done only at the expense of higher computation time[6].

While (D.24) preserves the numerical dynamics, the computational efficiency is not improved due to the matrix multiplications to calculate the $\widetilde{\mathbf{X}}$ term in (D.23). An alternative formulation that improves the computational speed is derived by replacing the matrix $\mathbf{R}$ with (D.10) in (D.20)

$$\mathbf{X}\mathbf{I}_n = \lambda_n \mathbf{S}^{\mathrm{T}}\mathbf{S}\mathbf{I}_n, \tag{D.27}$$

and multiplying from the left with $\mathbf{S}\mathbf{X}^{-1}$

$$\mathbf{S}\mathbf{I}_n = \lambda_n \mathbf{S}\mathbf{X}^{-1}\mathbf{S}^{\mathrm{T}}\mathbf{S}\mathbf{I}_n. \tag{D.28}$$

The formulation (D.28) is a standard eigenvalue problem and can be written as

$$\mathbf{S}\mathbf{X}^{-1}\mathbf{S}^{\mathrm{T}}\widehat{\mathbf{I}}_n = \widehat{\mathbf{X}}\widehat{\mathbf{I}}_n = \xi_n \widehat{\mathbf{I}}_n, \tag{D.29}$$

where $\widehat{\mathbf{X}} = \mathbf{S}\mathbf{X}^{-1}\mathbf{S}^{\mathrm{T}}$, $\widehat{\mathbf{I}}_n = \mathbf{S}\mathbf{I}$, and $\xi_n = 1/\lambda_n$. As an intermediary step, the matrix $\mathbf{X}_{\mathrm{S}} = \mathbf{X}^{-1}\mathbf{S}^{\mathrm{T}}$ is computed, which is later used to calculate the characteristic eigenvectors $\mathbf{I}_n = \lambda_n \mathbf{X}_{\mathrm{S}}\widehat{\mathbf{I}}_n$. The eigenvalue problem (D.29) is solved in the basis of spherical vector waves, $\widehat{\mathbf{I}}_n = \mathbf{S}\mathbf{I}$, that results in a matrix $\widehat{\mathbf{X}} \in \mathbb{C}^{N_\alpha \times N_\alpha}$. For problems with $N_\alpha \ll N_\psi$ the eigenvalue problem is solved rapidly compared with (D.20) and (D.24). The computation times for various examples are presented in Table D.4 for all three formulations where a different number of CMs are compared. For Example H1 the computation time is investigated for the first 20 and 100 modes. The acceleration using (D.29) is approximately 4.7 and 14 times when compared with the conventional method (D.20). The firstCM of Example H1 is illustrated in Fig. D.4.

Two tests proposed in [75] are performed to validate the conformity of characteristic current densities and the characteristic far fields with the analytically known values. The results of the former test are depicted in Fig. D.5 for Example S2 and S5 that are spherical shells with two different d-o-f. Similarity coefficients $\chi_{\tau n}$ are depicted both for the CMs using the matrix $\mathbf{R}$ (D.20) and for the CMs calculated by (D.24). The number of valid modes correlates well with Table D.3 and the same dependence on the quality and size of the mesh grid as in [75] is observed.

Qualitatively the same behavior is also observed in the latter test, depicted in Fig. D.6, where similarity of characteristic far fields is expressed by coefficient $\zeta_{\tau n}$ [75]. These coefficients read

$$\zeta_{\tau n} = \max_{l} \sum_{\sigma m} \left| \tilde{f}_{\tau\sigma mln} \right|^2, \tag{D.30}$$

[6]For Example S2 the computation time of CMs with quadruple precision is approximately 15 hours.

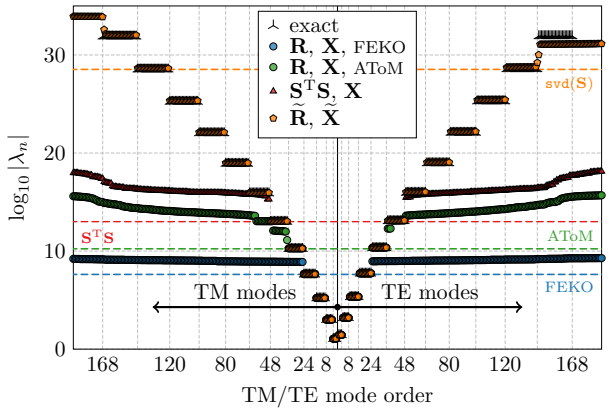


**Figure D.2:** Absolute values of the CMs of spherical shell with electrical size $ka = 0.5$ (Example S2). Data calculated with classical procedure (D.20) are compared with techniques from this paper, (D.21), (D.24), and with the analytical results valid for the spherical shell [75].

| Example | | Time to calculate $N_\lambda$ CMs (s) | | |
|---|---|---|---|---|
| (see Table D.2) | $N_\lambda$ | (D.20) | (D.24) | (D.29) |
| S1 | 10 | 0.36 | 0.18 | 0.12 |
| S2 | 300 | 3.3 | 2.0 | 1.1 |
| S4 | 10 | 2.8 | 2.5 | 0.78 |
| S4 | 100 | 13 | 2.1 | 0.72 |
| R1 | 100 | 0.29 | 0.28 | 0.42 |
| R3 | 50 | 7.2 | 1.3 | 0.49 |
| H1 | 20 | 130 | 150 | 28 |
| H1 | 100 | 500 | 150 | 35 |
| H2 | 100 | 350 | 160 | 35 |

**Table D.4:** Comparison of computation time required by various methods capable to calculate first $N_\lambda$ CMs. The calculations were done on Windows Server 2012 with 2×Xeon E5-2665 CPU @ 2.4 GHz and 72 GB RAM.

where $\tilde{f}_{\tau\sigma mln}$ has been evaluated using (D.14).

The results for characteristic far fields computed from the conventional procedure (D.20) and the procedure presented in this paper (D.24) are illustrated in Fig. D.6.

Finally, the improved accuracy of using (D.24) over (D.20), is demonstrated in the Fig. D.7 which shows current profiles, corresponding to a rectangular plate (Example R2), of a selected high order mode (a collection of the first 30 modes is presented in [76]). It can be seen that for modes with high eigenvalues (numerically

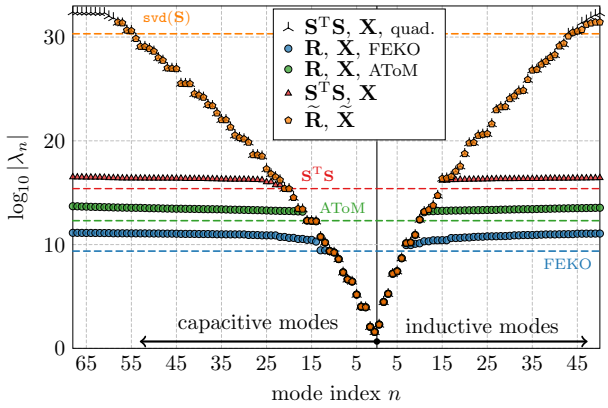


**Figure D.3:** Absolute values of the CMs of rectangular plate (Example R2). Since unknown analytical results, the multiprecision package Advanpix has been used instead to calculate the first 150 modes from impedance matrix in quadruple precision.

saturated regions in Fig. D.3) the surface current density in left panel, calculated via (D.20), shows numerical noise, while the evaluation via (D.24) still yields a correct current profile.

### D.3.3 Restriction to TM/TE modes

Matrix **S**, described in Section D.2.2, contains projections onto TE and TM spherical waves in its odd ($\tau = 1$) and even rows ($\tau = 2$), respectively. The separation of TE and TM spherical waves can be used to construct resistance matrices $\mathbf{R}^{\mathrm{TE}}$ and $\mathbf{R}^{\mathrm{TM}}$, where only odd and even rows of matrix **S** are used to evaluate (D.10).

Matrices $\mathbf{R}^{\mathrm{TM}}$ and $\mathbf{R}^{\mathrm{TE}}$ can be used in optimization, *e.g.*, in such a case, when the antennas have to radiate TM-modes only [104]. With this feature, CMs consisting of only TM (or TE) modes can easily be found. This is shown in Fig. D.8, in which the spherical shell (Example S2) and rectangular plate (Example R2) are used to find only TM (capacitive) and TE (inductive) modes, respectively. In case of a spherical shell, this separation could have been done during the post-processing. For a generally shaped body this separation however represents a unique feature of the proposed method.

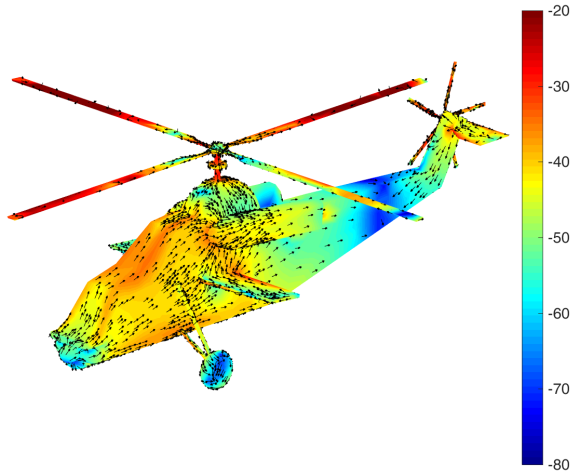


**Figure D.4:** Current density of the first CM of a helicopter at $ka = 7$ (Example H2), mesh grid has been taken from [152].

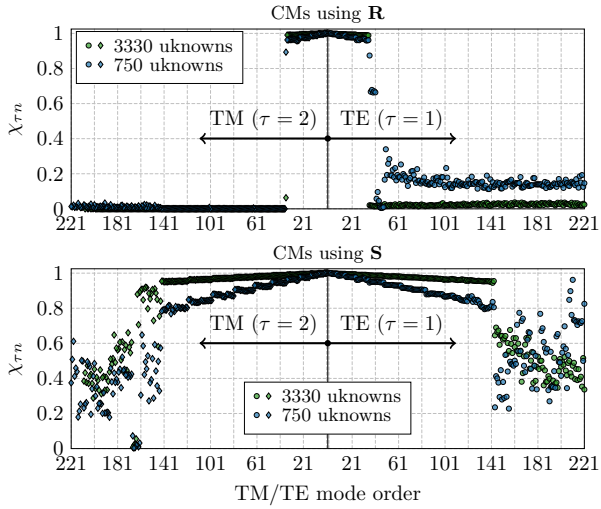


**Figure D.5:** Similarity of numerically evaluated characteristic currents for a spherical shell of two different discretizations (Example S2 and S5) and the analytically known currents [75]. The coefficients $\chi_{\tau n}$ were calculated according to [75], top panel depicts results for the conventional procedure (D.20), bottom panel for the procedure from this paper (D.24).

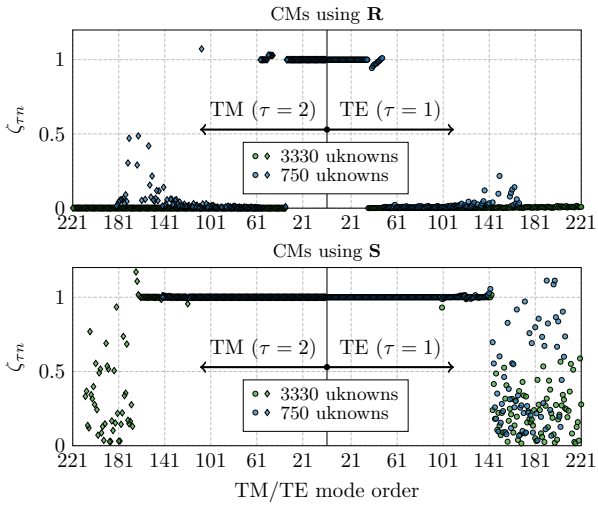


**Figure D.6:** Similarity of numerically and analytically evaluated characteristic far fields for a spherical shell of two different discretizations (Example S2 and S5) and analytically known far fields [75]. The coefficients $\zeta_{\tau n}$ were calculated by (D.30) (see [75] for more details). Top panel depicts results for the conventional procedure (D.20), bottom panel for the procedure from this paper (D.24).

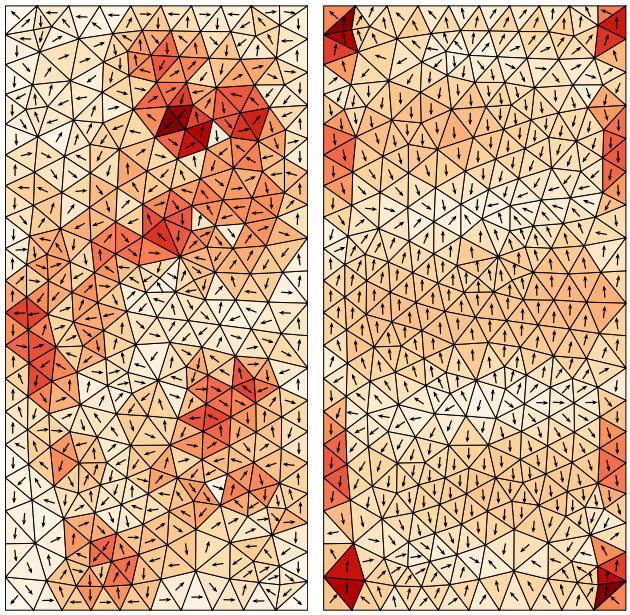

**Figure D.7:** Comparison of the higher-order CMs of the rectangular plate (Example R2) with the most similar characteristic number, Left: conventional procedure (D.20), Right: procedure from this paper (D.24). The first 30 modes evaluated via both procedures are available as interactive collection in [76] (see Fig. D.3).

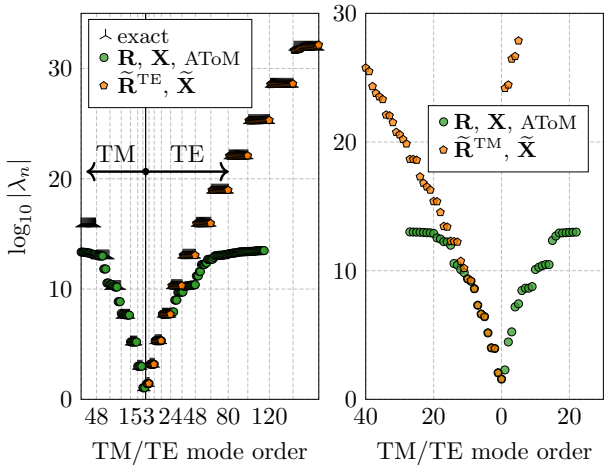


**Figure D.8:** Left: absolute values of the CMs of a spherical shell (Example S2) if only odd rows of the matrix **S** are kept. Right: absolute values of the CMs of a rectangular plate (Example R2) if only even rows of the matrix **S** are kept.

## D.4 Discussion

Important aspects of the utilization of the matrix $\mathbf{S}$ are discussed under the headings implementation aspects, computational aspects, and potential improvements.

### D.4.1 Implementation Aspects

Unlike the reactance matrix $\mathbf{X}$, the resistance matrix $\mathbf{R}$ suffers from high condition number. Therefore, the combined approach to evaluate the impedance matrix (matrix $\mathbf{R}$ using matrix $\mathbf{S}$, matrix $\mathbf{X}$ using conventional Green function technique with double integration) takes advantage of both methods and is optimal for, *e.g.*, modal decomposition techniques dealing with the matrix $\mathbf{R}$ (radiation modes [56], CMs, energy modes [56, 101], and solution of optimization problems [104]). Evaluation and the SVD of the matrix $\mathbf{S}$ are also used to estimate number of modes (see number of modes of the matrix $\mathbf{S}$ found by (D.18) and number of CMs found by (D.24) in Table D.3).

### D.4.2 Computational Aspects

Computational gains of the proposed method are seen in Table D.1 for the matrix $\mathbf{R}$ and Table D.4 for the CMs. The formulation (D.29) significantly accelerates CMs computation when compared with the classical GEP formulation (D.20). Moreover, it is possible to employ lower precision floating point arithmetic, *e.g.* float, to compute as many modes as the conventional method that employs higher precision floating point arithmetic, *e.g.* double. In modern hardware, this can provide additional performance boosts if vectorization is used.

An advantage of the proposed method is that the matrix $\mathbf{S}$ is rectangular for $N_\alpha < N_\psi$, allowing independent selection of the parameters $N_\psi$ and $N_\alpha$. While the parameter $N_\psi$ controls the details in the model, the parameter $N_\alpha$ (or alternatively $L$) controls the convergence of the matrix $\mathbf{S}$ and the number of modes to be found. In this paper (D.16) is used to determine the highest spherical wave order $L$ for a given electrical size $ka$. The parameter $L$ can be increased for improved accuracy or decreased for computational gain depending on the requirements of the problem. Notice that the parameter $N_\alpha$ is limited from below by the convergence and the number of desired modes, but also from above since the spherical Bessel function in $\mathbf{u}_\alpha^{(1)}(k\boldsymbol{r})$ decays rapidly with $l$ as

$$\mathrm{j}_l(ka) \approx \frac{2^l l!}{(2l+1)!}(ka)^l, \quad ka \ll l. \tag{D.31}$$

The rapid decay can be observed in Fig. D.1, where the convergence of the matrix $\mathbf{R}$ to double precision for $ka = 3$ requires only $L = 12$ while (16) gives a conservative number of $L = 17$.

### D.4.3 Potential Improvements

Even though the numerical dynamic is increased, it is strictly limited and it presents an inevitable, thus fundamental, bottleneck of all modal methods involving radiation properties. The true technical limitation is, in fact, the SVD of the matrix $\mathbf{S}$. A possible remedy is the use of high-precision packages that come at the expense of

markedly longer computation times and the necessity of performing all subsequent operations in the same package to preserve high numerical precision.

The second potential improvement relies on higher-order basis functions, which can compensate a poor-meshing scheme (that is sometimes unavoidable for complex or electrically large models). It can also reduce the number of basis function $N_\psi$ so that the evaluation of CMs is further accelerated.

## D.5 Conclusion

Evaluation of the discretized form of the EFIE impedance operator, the impedance matrix, has been reformulated using projection of vector spherical harmonics onto a set of basis functions. The key feature of the proposed method is the fact that the real part of the impedance matrix can be written as a multiplication of the spherical modes projection matrix with itself. This feature accelerates modal decomposition techniques and doubles the achievable numerical dynamics. The results obtained by the method can also be used as a reference for validation and benchmarking.

It has been shown that the method has notable advantages, namely the number of available modes can be estimated prior to the decomposition and the convergence can be controlled via the number of basis functions and the number of projections. The normalization of GEPs with respect to the product of the spherical modes projection matrix on the right hand side are implicitly done. The presented procedure finds its use in various optimization techniques as well. It allows for example to prescribe the radiation pattern of optimized current by restricting the set of the spherical harmonics used for construction of the matrix.

The method can be straightforwardly implemented into both in-house and commercial solvers, improving thus their performance and providing antenna designers with more accurate and larger sets of modes.

## D.A Used Computational Electromagnetics Packages

### D.A.1 FEKO

FEKO (ver. 14.0-273612, [152]) has been used with a mesh structure that was imported in NASTRAN file format [186]: CMs and far fields were chosen from the model tree under *requests* for the FEKO solver. Data from FEKO were acquired using *.out, *.os, *.mat and *.ffe files. The impedance matrices were imported using an in-house wrapper [162]. Double precision was enabled for data storage in solver settings.

### D.A.2 AToM

AToM (pre-product ver., CTU in Prague, [150]) has been used with a mesh grid that was imported in NASTRAN file format [186], and simulation parameters were set to comply with the data in Table D.2. AToM uses RWG basis functions with the Galerkin procedure [44]. The Gaussian quadrature is implemented according to [187] and singularity treatment is implemented from [174]. Built-in Matlab functions are utilized for matrix inversion and decomposition. Multiprecision package Advanpix [194] is used for comparison purposes.

### D.A.3 IDA

IDA (in-house, Lund University, [162]) has been used with the NASTRAN mesh and processed with the IDA geometry interpreter. IDA solver is a Galerkin type MoM implementation. RWG basis functions are used for the current densities. Numerical integrals are performed using Gaussian quadrature [187] for non-singular terms and the DEMCEM library [212–215] for singular terms. Intel MKL library [210] is used for linear algebra routines. The matrix computation routines are parallelized using OpenMP 2.0 [216]. Multiprecision computations were done with the mpmath Python library [209].

## D.B Spherical Vector Waves

General expression of the (scalar) spherical modes is [48]

$$\mathrm{u}_{\sigma ml}^{(p)}(k\boldsymbol{r}) = \mathrm{z}_l^{(p)}(kr)\mathrm{Y}_{\sigma ml}\left(\hat{\boldsymbol{r}}\right), \tag{D.32}$$

with $\hat{\boldsymbol{r}} = \boldsymbol{r}/|\boldsymbol{r}|$ and $k$ being the wavenumber. The indices are $m \in \{0, \ldots, l\}$, $\sigma \in \{\mathrm{e}, \mathrm{o}\}$ and $l \in \{1, \ldots, L\}$ [185, 204]. For regular waves $\mathrm{z}_l^{(1)} = \mathrm{j}_l$ is a spherical Bessel function of order $l$, irregular waves $\mathrm{z}_l^{(2)} = \mathrm{n}_l$ is a spherical Neumann function, and $\mathrm{z}_l^{(3,4)} = \mathrm{h}_l^{(1,2)}$ are spherical Hankel functions for the ingoing and outgoing waves, respectively. Spherical harmonics are defined as [48]

$$\mathrm{Y}_{\sigma ml}\left(\hat{\boldsymbol{r}}\right) = \sqrt{\frac{\varepsilon_m}{2\pi}}\widetilde{P}_l^m\left(\cos\vartheta\right)\begin{Bmatrix}\cos m\varphi \\ \sin m\varphi\end{Bmatrix}, \quad \sigma = \begin{Bmatrix}\mathrm{e} \\ \mathrm{o}\end{Bmatrix} \tag{D.33}$$

with $\varepsilon_m = 2 - \delta_{m0}$ the Neumann factor, $\delta_{ij}$ the Kronecker delta function and $\tilde{\mathrm{P}}_l^m\left(\cos\vartheta\right)$ the normalized associated Legendre functions [217].

The spherical vector waves are [48, 185]

$$\mathbf{u}_{1\sigma ml}^{(p)}\left(k\boldsymbol{r}\right) = \mathrm{R}_{1l}^{(p)}\left(kr\right)\mathbf{Y}_{1\sigma ml}\left(\hat{\boldsymbol{r}}\right), \tag{D.34a}$$

$$\mathbf{u}_{2\sigma ml}^{(p)}\left(k\boldsymbol{r}\right) = \mathrm{R}_{2l}^{(p)}\left(kr\right)\mathbf{Y}_{2\sigma ml}\left(\hat{\boldsymbol{r}}\right) + \mathrm{R}_{3l}^{(p)}\left(kr\right)\mathrm{Y}_{\sigma ml}\left(\hat{\boldsymbol{r}}\right)\hat{\boldsymbol{r}}, \tag{D.34b}$$

where $\mathrm{R}_{\tau l}^{(p)}\left(kr\right)$ are the radial function of order $l$ defined as

$$\mathrm{R}_{\tau l}^{(p)}\left(\kappa\right) = \begin{cases} \mathrm{z}_l^{(p)}(\kappa), & \tau = 1, \quad \text{(D.35a)} \\ \dfrac{1}{\kappa}\dfrac{\partial}{\partial\kappa}\left(\kappa\mathrm{z}_l^{(p)}\left(\kappa\right)\right), & \tau = 2, \quad \text{(D.35b)} \\ \dfrac{b_l}{\kappa}\mathrm{z}_l^{(p)}(\kappa), & \tau = 3, \quad \text{(D.35c)} \end{cases}$$

with $b_l = \sqrt{l\left(l+1\right)}$. The real-valued vector spherical harmonics $\mathbf{Y}_{\tau\sigma ml}\left(\hat{\boldsymbol{r}}\right)$ are defined as

$$\mathbf{Y}_{1\sigma ml}\left(\hat{\boldsymbol{r}}\right) = \frac{1}{b_l}\nabla \times \left(\boldsymbol{r}\mathrm{Y}_{\sigma ml}\left(\hat{\boldsymbol{r}}\right)\right), \tag{D.36a}$$

$$\mathbf{Y}_{2\sigma ml}\left(\hat{\boldsymbol{r}}\right) = \hat{\boldsymbol{r}} \times \mathbf{Y}_{1\sigma ml}\left(\hat{\boldsymbol{r}}\right), \tag{D.36b}$$

where $\mathrm{Y}_{\sigma ml}$ denotes the ordinary spherical harmonics [48]. The radial functions can be separated into real and imaginary parts as

$$\mathrm{R}_{\tau l}^{(3)}(\kappa) = \mathrm{R}_{\tau l}^{(1)}(\kappa) + \mathrm{j}\mathrm{R}_{\tau l}^{(2)}(\kappa), \tag{D.37}$$

$$\mathrm{R}_{\tau l}^{(4)}(\kappa) = \mathrm{R}_{\tau l}^{(1)}(\kappa) - \mathrm{j}\mathrm{R}_{\tau l}^{(2)}(\kappa). \tag{D.38}$$

## D.C Associated Legendre Polynomials

The associated Legendre functions are defined [181] as

$$P_l^m(x) = \left(1-x^2\right)^{m/2} \frac{\mathrm{d}^m}{\mathrm{d}x^m} P_l(x), \quad l \geq m \geq 0, \tag{D.39}$$

with

$$P_l(x) = \frac{1}{2^l l!} \frac{\mathrm{d}^l}{\mathrm{d}x^l} \left(x^2-1\right)^l \tag{D.40}$$

being the associated Legendre polynomials of degree $l$ and $x \in [-1, 1]$. One useful limit when computing the vector spherical harmonics is [48]

$$\lim_{x\to 1} \frac{P_l^m(x)}{\sqrt{1-x^2}} = \delta_{m1} \frac{l(l+1)}{2}. \tag{D.41}$$

The normalized associated Legendre function $\tilde{P}_l^m$, is defined as follows

$$\widetilde{P}_l^m(x) = \sqrt{\frac{2l+1}{2}\frac{(l-m)!}{(l+m)!}} P_l^m(x). \tag{D.42}$$

The derivative of the normalized associated Legendre function is required when computing the spherical harmonics and is given by the following recursion relation

$$\frac{\partial}{\partial\vartheta}\widetilde{P}_l^m(\cos\vartheta) = \frac{1}{2}\sqrt{(l+m)(l-m+1)}\widetilde{P}_l^{m-1}(\cos\vartheta) - \frac{1}{2}\sqrt{(l-m)(l+m+1)}\widetilde{P}_l^{m+1}(\cos\vartheta) \tag{D.43}$$

where $x \equiv \cos\vartheta$, $\vartheta \in [0, \pi]$.

# E Method of Moments and T-matrix Hybrid

**Published as:** **V. Losenicky**, L. Jelinek, M. Capek, and M. Gustafsson, "Method of Moments and T-matrix Hybrid," *IEEE Transactions on Antennas and Propagation*, vol. 70, no. 5, pp. 3560–3574, May 2022, DOI: 10.1109/TAP.2021.3138265.

**Abstract**— Hybrid computational schemes combining the advantages of a method of moments formulation of a field integral equation and T-matrix method are developed in this paper. The hybrid methods are particularly efficient when describing the interaction of electrically small complex objects and electrically large objects of canonical shapes such as spherical multi-layered bodies where the T-matrix method is reduced to the Mie series making the method an interesting alternative in the design of implantable antennas or exposure evaluations. Method performance is tested on a spherical multi-layer model of the human head. Along with the hybrid method, an evaluation of the transition matrix of an arbitrarily shaped object is presented and the characteristic mode decomposition is performed, exhibiting fourfold numerical precision as compared to conventional approaches.

**Index terms:** Antennas, scattering, numerical analysis, method of moments, T-matrix method, eigenvalue problems.

## E.1 Introduction

Numerical evaluation of electromagnetic (EM) fields is inevitable in virtually every feasible electromagnetic design and is a driving force for the development of various computational schemes in the field of computational electromagnetism [218]. This paper focuses on one part of this immensely vast topic, specifically on time-harmonic and full-wave descriptions of open multi-scale problems where several objects of varying electrical size interact in otherwise open space.

One of the basic, full-wave numerical techniques for solving open boundary electromagnetic problems is the method of moments (MoM) formulation of field integral equations [24]. This method is most popular in its surface version [44] which assumes highly conducting bodies or surface equivalence treatment [180]. In these cases, the method reveals its greatest advantages: accuracy, low number of unknowns and computational efficiency all of which are associated with the discretization of

surface current densities. The major weakness of this method is the use of a fully populated system matrix which leads to an undesirable increase in memory and computational requirements with increasing complexity and electrical size of the problem[219].

The aforementioned difficulties are most commonly mitigated via the multilevel fast multipole algorithm (MLFMA) [220], the adaptive cross approximation algorithm (ACAA) [221], and the characteristic basis functions method (CBFM) [222]. The MLFMA mitigates memory and computational requirements while maintaining accuracy using interaction via multi-pole expansion. The ACAA reduces the computational complexity and memory requirements like the MLFMA while remaining independent of the integration kernel. The CBFM deals with the weaknesses from a different prospective and uses high-level basis functions defined on macro domains leading to matrix size reduction. An alternative is to implement piecewise-defined high-order basis functions [223] which can significantly reduce the number of unknowns [219].

The description via volume integral equations can also be used in cases of complex material distributions, but, with the exception of bodies of revolution[224] and translation symmetries [225, 226], the memory and computational requirements forbid its use in realistic scenarios. In such cases, the finite element method (FEM) [22] operating over differential equations is typically used instead. Unfortunately, there is no universal method, and the FEM has its problems, the major ones being the accurate treatment of open boundaries and electrically large objects [22].

When multi-scale objects interact, the leading approach is the use of hybrid methods attempting to use particular evaluation schemes only in situations when they are effective. In the case of open electromagnetic problems with only medium electric size, the hybrid combining the FEM for regions of high material complexity and the integral equation method for treating highly conducting objects and open boundaries is common [227–231] and is a part of several commercial [232, 233] as well as in-house[234] implementations.

Despite the great versatility of the aforementioned hybrid method, the description of the interaction of electrically small and electrically large material objects is nevertheless problematic. However, in many cases, the electrically large object can be approximated by a spheroidal geometry, a situation when the T-matrix method [25] can be advantageously used. The most important property in this respect is the use of spherical vector waves as entire domain basis functions. This allows for the compressed description of spheroidal-like bodies [184, 235] or even a description by a diagonal matrix in the case of a spherical multi-layer, which is a common approximation used in electromagnetism.

The purpose of this paper is to approach the multi-scale problem by combining the MoM formulation of the electric field integral equation and the T-matrix method in which the T-matrix method is used to describe interacting electrically large objects of simple shape efficiently. The coupling between the two methods is described by spherical vector waves [185]. The major advantage of the proposed computational scheme is its ability to provide a full system matrix of the electrically small object in the otherwise multi-scale scenario.

The paper is organized as follows. The MoM formulation of the electric field integral equation and the T-matrix method are briefly recapitulated in Sections E.2.1 and E.2.2, respectively, and the “external” and “internal” formulations of their hybrid method are afterwards developed in Sections E.3.1 and E.3.2. Section E.4 provides the numerical verification of the hybrid method. The unification of “external” and “internal” formulation is presented in Section E.5 and is later verified in Section E.6.

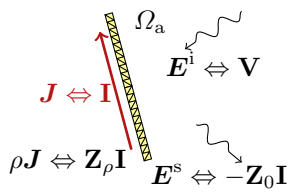


**Figure E.1:** An illustration of the MoM formulation for the electric field integral equation where the underlying scatterer is discretized into a set of elementary cells. The figure also interrelates field variables $\boldsymbol{J}$, $\rho\boldsymbol{J}$, $\boldsymbol{E}^s$, and $\boldsymbol{E}^i$ with their discretized counter parts $\mathbf{I}, \mathbf{Z}_\rho\mathbf{I}$, $-\mathbf{Z}_0\mathbf{I}$, and $\mathbf{V}$, respectively.

Various aspects of the hybrid method are discussed in Section E.8 and the paper is concluded with Section E.9.

## E.2 Basic Constituents of the Hybrid Method

This section briefly reviews the MoM formulation of field integral equations [24] and the T-matrix method [25], the basic constituents of which are subsequently hybridized.

### E.2.1 Method of Moments Formulation to Electric Field Integral Equation

The electric field integral equation[1] is formed by relating the polarization (or conduction) current density in a material object to the total electric field as

$$\boldsymbol{E}^s(\boldsymbol{J}) + \boldsymbol{E}^i = \rho\boldsymbol{J}, \tag{E.1}$$

with

$$\boldsymbol{E}^s(\boldsymbol{J}) = -\mathrm{j}kZ\langle \boldsymbol{G}_e, \boldsymbol{J}\rangle \tag{E.2}$$

being the scattered field produced by current distribution $\boldsymbol{J}$, $\boldsymbol{E}^i$ being the incident field, $k$ being the background wavenumber[2], $Z$ being the background wave impedance, $\boldsymbol{G}_e$ being the dyadic Green's function for electric fields, and $\rho(\boldsymbol{r})$ being the complex resistivity of the underlying material. The relation (E.2) also utilizes a symmetric product (reaction) [236], which is, for volume distributions, defined as

$$\langle \boldsymbol{A}, \boldsymbol{B}\rangle \equiv \int_V \boldsymbol{A}\cdot\boldsymbol{B}\,\mathrm{d}V \tag{E.3}$$

with $V$ indicating the support of fields $\boldsymbol{A}$ and $\boldsymbol{B}$. An analogous symmetry product can be defined for surface current distribution by integration over the corresponding

[1] Time-harmonic steady state of convention $\exp\{\mathrm{j}\omega t\}$, where $\omega$ is the angular frequency and j the imaginary unit, is assumed throughout the paper.

[2] Any homogeneous lossless dielectric material can be considered as background in this formulation.

surface. A similar distinction should be made over complex resistivity $\rho$, which typically refers to a volumetric case, while for surface current distribution is the resistivity commonly substituted by a surface impedance [85, 237].

To solve (E.1) numerically, the original material object is decomposed into a set of elementary cells (*e.g.*, triangles, tetrahedrons), see Fig. E.1, together with the current density which is rewritten as a weighted sum of basis functions $\{\boldsymbol{\psi}_n\}$

$$\boldsymbol{J}(\boldsymbol{r}) \approx \sum_{n=1}^{N} I_n \boldsymbol{\psi}_n(\boldsymbol{r}). \tag{E.4}$$

Substituting (E.4) into (E.1) and employing the Galerkin testing technique [47] results in a linear system of equations

$$-\Big[\big\langle \boldsymbol{\psi}_m, \boldsymbol{E}^{\mathrm{s}}(\boldsymbol{\psi}_n)\big\rangle\Big]\mathbf{I} + \Big[\big\langle \boldsymbol{\psi}_m, \rho\boldsymbol{\psi}_n\big\rangle\Big]\mathbf{I} = \Big[\big\langle \boldsymbol{\psi}_m, \boldsymbol{E}^{\mathrm{i}}\big\rangle\Big], \tag{E.5}$$

which can be rewritten as

$$(\mathbf{Z}_0 + \mathbf{Z}_\rho)\,\mathbf{I} = \mathbf{V}, \tag{E.6}$$

with $\mathbf{Z}_0$ being the impedance matrix of the radiation part of the system, $\mathbf{Z}_\rho$ being the impedance matrix of the material part of the system, $\mathbf{V}$ being the excitation vector, and $\mathbf{I}$ being the unknown vector of current expansion coefficients.

Field integral equations are part of many commercial [232, 238–240] and academic [150] electromagnetic simulators with the major advantage being the implicit incorporation of boundary conditions into Green's function [241], which renders the MoM formulation of field integral equations as an excellent method for open problems. The resulting operator matrices are dense but typically much smaller as compared to, *e.g.*, FEM, yet fully describe the EM properties of the radiator. This allows eigenvalue problems to be formulated, such as characteristic mode decomposition [9] or the optimal current densities representing fundamental bounds on EM metrics [28] to be found. The disadvantage is an undesired sextic growth of memory requirements with the electrical size of a radiator. With radiation being the dominating interaction, memory requirement can be reduced and a solution can be accelerated via the MLFMA [220] or ACAA [221], which lead to linearithmic time and cubic storage, but forbids the direct evaluation of the fundamental bounds. Instead, the individual obstacles can be decoupled and treated independently, for example, by combining MoM with piecewise defined basis functions [43] and the T-matrix method for spherical waves [48] into one system of equations which are still compatible with mode decomposition techniques, convex optimization, and other methods explicitly requiring the impedance matrix.

### E.2.2 T-matrix Method

The T-matrix method is used to solve a similar scenario as in (E.1) using spherical harmonics as entire-domain basis functions making it extremely effective in solving scattering from spheroidal particles [242]. The T-matrix method [25] starts with an expansion of the incident and scattered electric field external to the material object, see Fig. E.2, into a set of spherical vector waves as [185]

$$\boldsymbol{E}^{\mathrm{i}}(\boldsymbol{r}) = k\sqrt{Z}\sum_{\alpha} a_{1,\alpha}\,\mathbf{u}_{\alpha}^{(1)}(k\boldsymbol{r}), \tag{E.7}$$

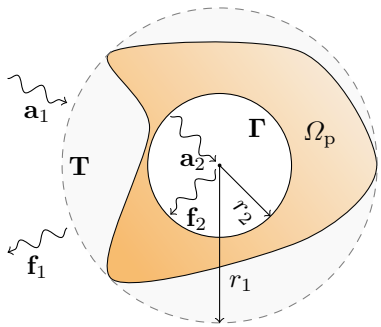


**Figure E.2:** Scattering properties of object $\Omega_\mathrm{p}$ are described by scattering operator $\mathbf{T}$ for external problems and by operator $\mathbf{\Gamma}$ for internal problems. Since both operators are based on the expansion of the dyadic Green's function into spherical vector waves, all field quantities are valid only in the region $r < r_1$ and $r > r_2$.

$$\boldsymbol{E}^\mathrm{s}(\boldsymbol{r}) = k\sqrt{Z}\sum_\alpha f_{1,\alpha}\,\mathbf{u}_\alpha^{(4)}(k\boldsymbol{r})\,, \tag{E.8}$$

where $\mathbf{a}_1$ is a vector of expansion coefficients of the incident field into regular spherical vector waves, $\mathbf{f}_1$ is a vector of expansion coefficients of the scattered field into a set of out-going spherical vector waves, and $\mathbf{u}_\alpha^{(p)}(k\boldsymbol{r})$ are the spherical vector waves defined in Appendix E.A. Note that such an expansion is only valid outside a sphere circumscribing the material object, see Fig. E.2. Since a homogeneous background material is assumed outside the circumscribing sphere, it is possible to define transition matrix $\mathbf{T}$ via

$$\mathbf{f}_1 = \mathbf{T}\mathbf{a}_1, \tag{E.9}$$

forming a linear system analogous to (E.6). For spherical objects, matrix $\mathbf{T}$ can be obtained analytically, see Appendix E.B. For material objects of a general shape matrix $\mathbf{T}$ can be evaluated using the Null-field method [25, 243] or using matrix $\mathbf{Z}$ as described later, see Appendix E.C for final formulas.

The internal scattering problem defined via the expansion coefficients $\mathbf{a}_2$ and $\mathbf{f}_2$, see Fig. E.2, can also be solved by this methodology with the only change being that the incident field is formed by spherical waves outgoing from the origin while the scattered field is represented by regular spherical waves. With this change, the internal scattering problem can be described via

$$\mathbf{a}_2 = \mathbf{\Gamma}\mathbf{f}_2. \tag{E.10}$$

A major distinction between matrices $\mathbf{T}$ or $\mathbf{\Gamma}$ and matrix $\mathbf{Z}$ is the fact that neither $\mathbf{T}$ nor $\mathbf{\Gamma}$ are invertible and that a distinction must be made between external and internal problems.

The description via matrix $\mathbf{T}$ is widely used in the field of electromagnetic scattering [242] and, unlike the impedance matrix from the previous section, matrix $\mathbf{T}$ only accounts for the scattering reaction on the incident field produced externally to the scatterer. This method is especially efficient for scatterers of spheroidal shape when the system matrix can be evaluated analytically [48]. On the other hand, this simplification prohibits near fields within the sphere circumscribing the scatterer to

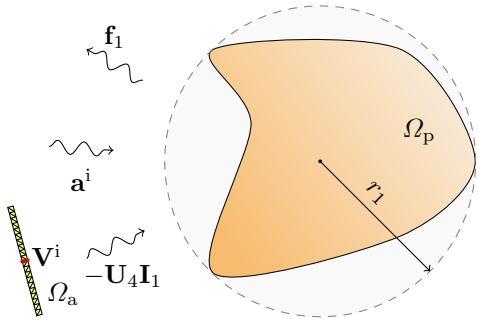


**Figure E.3:** An illustration of the hybrid method for the exterior of object $\Omega_{\mathrm{p}}$. The interaction between objects $\Omega_{\mathrm{p}}$ and $\Omega_{\mathrm{a}}$ is realized via spherical vector waves weighted by coefficients collected in vectors $\mathbf{f}_{1,2}$ and $\mathbf{a}_{1,2}$. Note that the complete vector $\mathbf{a}_1$ that excites object $\Omega_{\mathrm{p}}$ is given by (E.13), while the complete vector $\mathbf{V}$ exciting object $\Omega_{\mathrm{a}}$ is given by (E.11).

be studied or localized feeding ports on antennas to be defined since no sources can be present in region $\Omega_{\mathrm{p}}$. It is also not known how to evaluate fundamental bounds in such a description as there is no direct access to the internal degrees of freedom describing contrast current density within the scatterer.

## E.3 Hybrid Method

To characterize scattering from a complex-shaped object of electrical size not exceeding a few wavelengths or containing discrete feeding ports, the impedance matrix based on triangular or tetrahedral elements is the tool of choice mostly for numerical stability of this scheme regardless of the shape's complexity. On the contrary, when dealing with an electrically large regular-shaped and passive scatterer, the description via matrix $\mathbf{T}$ offers many advantages, such as a great model order reduction due to the use of appropriate entire domain basis functions. The purpose of this section is to combine the strengths of both methods. The resulting technique is shown to be especially fast and flexible for problems where canonical models of obstacles (described by matrix $\mathbf{T}$) are sufficient to grasp the most important interactions with radiator described by matrix $\mathbf{Z}$ such as those appearing in the study of implantable antennas. The resulting formulation still allows for modal decomposition or the evaluation of fundamental bounds via the convex optimization of current density [28].

### E.3.1 External Formulation

Let us assume two objects $\Omega_{\mathrm{p}}$ and $\Omega_{\mathrm{a}}$ depicted in Fig. E.3. Object $\Omega_{\mathrm{p}}$ is situated around the origin of the coordinate system and represented by matrix $\mathbf{T}$. Object $\Omega_{\mathrm{a}}$ is characterized by the matrix $\mathbf{Z} = \mathbf{Z}_0 + \mathbf{Z}_\rho$ and placed so that it does not intersect the sphere circumscribing object $\Omega_{\mathrm{p}}$. Assume further an impressed excitation $\boldsymbol{V}^{\mathrm{i}}$ (impressed electric field on object $\Omega_{\mathrm{a}}$ via, *e.g.*, a delta gap source) and $\mathbf{a}^{\mathrm{i}}$ (a set of impinging spherical waves).

To describe the problem in full, it is convenient to form a complete vector $\mathbf{V}$ exciting object $\Omega_\mathrm{a}$ from impressed field $\mathbf{V}^\mathrm{i}$, impressed field $\mathbf{a}^\mathrm{i}$, and field vector $\mathbf{f}_1$ produced by object $\Omega_\mathrm{p}$. Analogously, it is convenient to form a complete vector $\mathbf{a}_1$ from impressed field $\mathbf{a}^\mathrm{i}$ and from spherical waves $\mathbf{a}$ produced by object $\Omega_\mathrm{a}$.

Let us first focus on the complete vector $\mathbf{V}$. The field produced by object $\Omega_\mathrm{p}$ is given by (E.8). The impressed field $\boldsymbol{a}^\mathrm{i}$ is formed by a relation equivalent to (E.7). Adding these two fields, substituting into the right-hand side of (E.5) and subsequently adding $\mathbf{V}^\mathrm{i}$ leads to

$$\mathbf{V} = \mathbf{V}^\mathrm{i} + \mathbf{U}_1^\mathrm{T}\mathbf{a}^\mathrm{i} + \mathbf{U}_4^\mathrm{T}\mathbf{f}_1, \tag{E.11}$$

where matrices $\mathbf{U}_p$, $p \in \{1, \ldots, 4\}$, defined as

$$\mathbf{U}_p = k\sqrt{Z}\left[\left\langle \mathbf{u}_\alpha^{(p)}, \boldsymbol{\psi}_n \right\rangle\right], \tag{E.12}$$

project spherical waves onto basis functions $\boldsymbol{\psi}_n$, see Appendix E.A for details. Notice that matrices analogous to (E.12) are used in the null field method [48] and[3] in[244, (10-11)] [245, (11)].

The second relation is obtained expanding the field (E.2) produced by object $\Omega_\mathrm{a}$ into spherical expansion (E.7) and adding an impressed field $\mathbf{a}^\mathrm{i}$, which results in

$$\mathbf{a}_1 = \mathbf{a}^\mathrm{i} - \mathbf{U}_4\mathbf{I}. \tag{E.13}$$

Notice that the relation (E.13) uses the spherical expansion of the dyadic Green's function into spherical vector waves, see Appendix E.A. Combining (E.6), (E.9), (E.11) and (E.13) together, an equation system

$$\begin{bmatrix} \mathbf{Z} & -\mathbf{U}_4^\mathrm{T} & \mathbf{0} \\ -\mathbf{U}_4 & \mathbf{0} & -\mathbf{1} \\ \mathbf{0} & -\mathbf{1} & \mathbf{T} \end{bmatrix} \begin{bmatrix} \mathbf{I} \\ \mathbf{f}_1 \\ \mathbf{a}_1 \end{bmatrix} = \begin{bmatrix} \mathbf{V}^\mathrm{i} + \mathbf{U}_1^\mathrm{T}\mathbf{a}^\mathrm{i} \\ -\mathbf{a}^\mathrm{i} \\ \mathbf{0} \end{bmatrix} \tag{E.14}$$

is formed providing a direct solution to all unknown quantities.

It might be advantageous to partially resolve the system (E.14) for a particular unknown variable in many cases. A typical scenario might be object $\Omega_\mathrm{a}$ being studied in the presence of parasitic scatterer $\Omega_\mathrm{p}$. Eliminating unknowns $\mathbf{a}_1$ and $\mathbf{f}_1$ from (E.14) then gives

$$\left(\mathbf{Z} + \mathbf{U}_4^\mathrm{T}\mathbf{T}\mathbf{U}_4\right)\mathbf{I} = \mathbf{V}^\mathrm{i} + \left(\mathbf{U}_1^\mathrm{T} + \mathbf{U}_4^\mathrm{T}\mathbf{T}\right)\mathbf{a}^\mathrm{i}, \tag{E.15}$$

where the only unknown is current $\mathbf{I}$ on object $\Omega_\mathrm{a}$. Notice that this last equation is equivalent to applying the MoM to the electric field integral equation for scatterer $\Omega_\mathrm{a}$ using a Green's function accounting for object $\Omega_\mathrm{p}$. This last formulation is also prepared for the development of fundamental bounds based on a controllable current [41] supported in region $\Omega_\mathrm{a}$ in the presence of an uncontrollable scatterer residing in region $\Omega_\mathrm{p}$.

### E.3.2 Internal Formulation

A dual scenario, depicted in Fig. E.4, where an impressed spherical excitation has been omitted for clarity, can be solved analogously. For this arrangement, object $\Omega_\mathrm{a}$

[3] Note the use of normalization of spherical waves used in this paper.

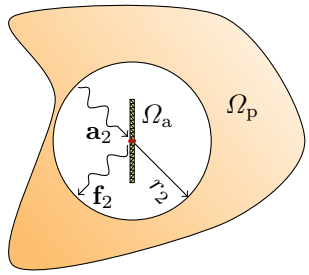


**Figure E.4:** An internal definition of the hybrid method involves an electromagnetic radiator (object $\Omega_\mathrm{a}$) inserted into the cavity of radius $r_2$ immersed in object $\Omega_\mathrm{p}$. The interaction between the radiator and the scatterer is provided by two vectors that stand for the weighting coefficients of regular $\mathbf{a}_2$ and out-going $\mathbf{f}_2$ spherical vector waves.

is centered at the origin of the coordinate system, while object $\Omega_\mathrm{p}$ contains a cavity surrounding it meeting the requirement that a circumscribing sphere of object $\Omega_\mathrm{a}$ fits inside the cavity. The total excitation of object $\Omega_\mathrm{p}$ reads

$$\mathbf{f}_2 = -\mathbf{U}_1\mathbf{I}, \tag{E.16}$$

while the total excitation of object $\Omega_\mathrm{a}$ reads

$$\mathbf{V} = \mathbf{V}^\mathrm{i} + \mathbf{U}_1^\mathrm{T}\mathbf{a}_2. \tag{E.17}$$

The algebraic expression for the problem defined in this way can therefore be written as

$$\begin{bmatrix} \mathbf{Z} & -\mathbf{U}_1^\mathrm{T} & \mathbf{0} \\ -\mathbf{U}_1 & \mathbf{0} & -\mathbf{1} \\ \mathbf{0} & -\mathbf{1} & \mathbf{\Gamma} \end{bmatrix} \begin{bmatrix} \mathbf{I} \\ \mathbf{a}_2 \\ \mathbf{f}_2 \end{bmatrix} = \begin{bmatrix} \mathbf{V}^\mathrm{i} \\ \mathbf{0} \\ \mathbf{0} \end{bmatrix}. \tag{E.18}$$

An equation analogous to (E.15), with the sole unknown being current $\mathbf{I}$, is given by

$$\left(\mathbf{Z} + \mathbf{U}_1^\mathrm{T}\mathbf{\Gamma}\mathbf{U}_1\right)\mathbf{I} = \mathbf{V}^\mathrm{i}. \tag{E.19}$$

It is important to note that even though the internal scattering operator $\mathbf{\Gamma}$ has a lot of common features with the transition matrix, it is not possible to find matrix $\mathbf{\Gamma}$ simply by the inversion of the transition matrix.

## E.4 Results: Numerical Validation

In this section, an evaluation of the transition matrix based on the impedance matrix, as well as the hybrid method combining MoM and the T-matrix method, are used for the analysis of several canonical problems. The results are compared with previously published results [76] or with the outcomes of the commercially available electromagnetic solvers FEKO [232] and CST [238].

### E.4.1 Characteristic Modes

Evaluation of matrix $\mathbf{T}$ is validated first. The test is based on the comparison of eigenvalues of matrix $\mathbf{T}$ and characteristic numbers obtained by characteristic mode decomposition [9] for a perfect electric conductor (PEC) shell for which characteristic numbers are known analytically [75]. Matrix $\mathbf{T}$ is known analytically as well in this case, see (E.37). Nevertheless, in order to prove the validity of the theory presented in the previous section, matrix $\mathbf{T}$ is evaluated numerically according to Appendix E.C.

The characteristic mode decomposition [9, 246] is for a lossless scatterer[4] defined by the generalized eigenvalue problem

$$\mathbf{X}\mathbf{I}_n = \lambda_n \mathbf{R}\mathbf{I}_n \tag{E.20}$$

in which matrices $\mathbf{R} = \mathrm{Re}\{\mathbf{Z}\}$ and $\mathbf{X} = \mathrm{Im}\{\mathbf{Z}\}$ are the real and imaginary parts of the impedance matrix respectively, $\lambda_n$ is the characteristic number, and $\mathbf{I}_n$ is a characteristic mode. The relation between the characteristic numbers and eigenvalues of matrix $\mathbf{T}$ can be expressed as

$$t_n = -\frac{1}{1 + \mathrm{j}\lambda_n} \tag{E.21}$$

with $t_n$ being the eigenvalues of matrix $\mathbf{T}$. The derivation of relation (E.21) is detailed in Appendix E.D. Notice that the identification of characteristic numbers with eigenvalues of matrix $\mathbf{T}$ has also been provided in [8, (18)].

The result of this first test is depicted in Fig. E.5 for a spherical shell with electrical size $ka = 0.5$, $a$ being the radius of the sphere. The spherical shell is discretized into 1376 triangles and Rao-Wilton-Glisson (RWG) basis functions [44] from (E.4) are used as a basis $\{\boldsymbol{\psi}_n(\boldsymbol{r})\}$. The characteristic numbers are computed in three different ways. First is the classical procedure of a generalized eigenvalue problem (E.20). Second is the improved approach using a modified impedance matrix and singular value decomposition [76] to enhance numerical precision. Finally, characteristic numbers are evaluated using an eigenvalue decomposition of matrix $\mathbf{T}$ (E.45) and its relation to characteristic numbers (E.21). Analytically known characteristic numbers (E.46) further supplement these three numerical solutions.

The results depicted in Fig. E.5 not only prove the validity of the matrix $\mathbf{T}$ evaluation but also show a superior accuracy of the third method, *i.e.*, of evaluating characteristic numbers from eigenvalues of matrix $\mathbf{T}$. The precision enhancement is immense, reaching a dynamic range of $10^{70}$ and doubling the dynamic range of the second-best numerical procedure.

The second numerical test uses the evaluation of characteristic numbers of a PEC cube discretized into 912 triangles and circumscribed by a sphere of radius $a$. In this case, characteristic numbers are not known analytically. The evaluation of matrix $\mathbf{T}$ is based on Appendix E.C. The results obtained from the second test are depicted in Fig. E.6. The numerical precision of characteristic numbers evaluated via (E.21) is once more superior and does not saturate as with the other methods.

### E.4.2 Hybrid Method

This section aims to verify the hybrid method described in Section E.3. The two scenarios, "external" in Fig. E.3 and "internal" in Fig. E.4, are tested separately.

[4] For a lossy scatterer, the right-hand side of (E.20) might be changed to $\mathbf{R}_0$, but in such a case the relation to eigensolutions of matrix $\mathbf{T}$ is lost.

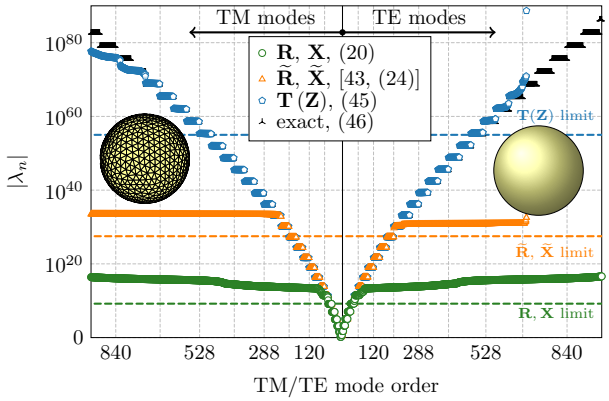


**Figure E.5:** Magnitudes of the characteristic numbers of a spherical shell ($ka = 0.5$). Presented results were obtained using four different methods: the classic procedure (E.20) depicted by green circles, the method presented in [76] depicted by orange triangles, the method presented in this paper (E.45) with transformation by (E.21) depicted by blue circles, and the analytic prescription [75] depicted by black stars.

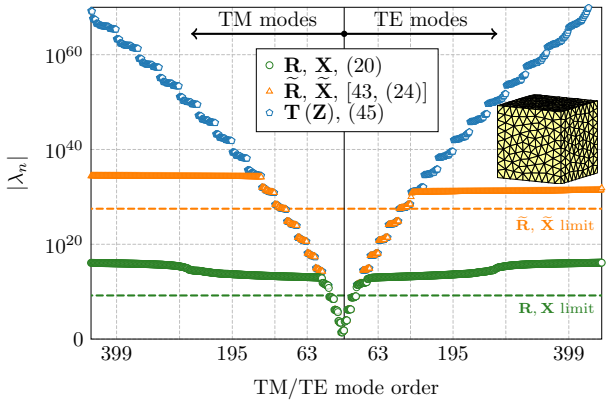


**Figure E.6:** Characteristic numbers of a PEC cube ($ka = 0.5$). The data traces are the same as in Fig. E.5.

The "external" case describing the relation between a passive body and an active radiator in its exterior is validated first. The test is built on the analysis of the interaction between a spherical shell and a dipole antenna. The spherical shell is centered at the origin, has outer radius $r$, thickness $d$, and is made of a material with relative permittivity $\varepsilon_\mathrm{r}$. At distance $g$ from the surface of the shell, a strip dipole antenna of length $\ell$ and width $w$ is located. For the sake of simplicity, the dipole antenna is modeled as a PEC strip fed in the middle by a delta-gap feed.

The verification is based on two quantities relevant for antenna performance: input

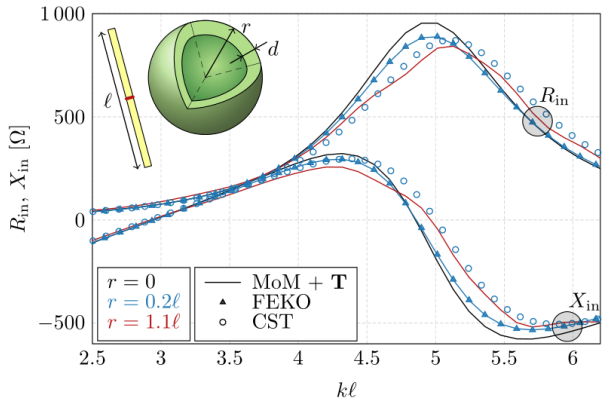


**Figure E.7:** Input impedance $Z_{\text{in}} = R_{\text{in}} + \text{j}X_{\text{in}}$ of a dipole with length $\ell$ and width $w = \ell/50$ discretized into 396 triangles. The geometric center of the dipole is located at distance $g = \ell/20$ from the surface of a spherical shell with outer radius $r$ and thickness $d/\ell = 0.05$ made of a material with relative permittivity $\varepsilon_{\text{r}} = 5 - 0.5\text{j}$. The black line represents input impedance for the dipole in vacuum. The blue line corresponds to a spherical shell with outer radius $r = 0.2\ell$ and evaluation via (E.14). This result is compared with the solution supplied by the combination of MoM and FEM solver of FEKO [232] and time-domain solver of CST [238]. Additionally, a result of (E.14) for the spherical shell with radius $r = 1.1\ell$ is shown (red lines).

impedance and radiation efficiency. The results depicted in Figs. E.7 and E.8 verify the method by comparing results of (E.14) with results obtained by the combination of MoM and FEM in FEKO [232] and the time-domain solver of CST [238]. Both figures suggest perfect agreement with the FEKO solver. A small deviation in the case of the input impedance evaluated by the CST solver can be attributed to a different model of the feed which consists of a physical gap in the CST solver. More details about solver settings can be found in Appendix E.F. The part of the hybrid method corresponding to the T-matrix method is based on the Mie series solution, see [247] and the references therein, and it is, hence, numerically inexpensive to modify the size of the lossy sphere as depicted in Fig. E.8.

Figure E.7 indicates that the input impedance in the vicinity of the resonance of the dipole is relatively stable and it is not significantly affected by its environment. For this reason, in addition to input impedance, radiation efficiency was also evaluated[5]. Since the dipole is lossless, any deviation of radiation efficiency from unity is induced by the spherical shell. The results are depicted in Fig. E.8 where perfect agreement between the solution via (E.14) and via the FEM solver of FEKO can once more be seen. Unlike input impedance, which does not depend much on the radius of the absorbing shell, the radiation efficiency of the system decreases significantly with the increasing ratio of $r/l$. This is caused by the increasing efficiency of thicker shells to absorb radiation.

[5]See Appendix E.E for details on power balance in the hybrid scenario described in this paper.

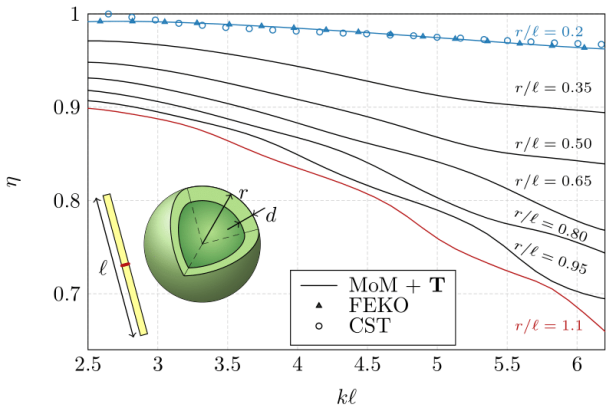


**Figure E.8:** The radiation efficiency of the dipole in the vicinity of the spherical shell of varying radius $r$. The setup is identical to Fig. E.7. In the case of a spherical shell of outer radius $r = 0.2\ell$, the result is compared with the FEKO and CST. Red and blue lines are the same as in Fig. E.7.

An essential aspect of the calculation using the hybrid method is to correctly determine the necessary number of spherical waves used to reach a given precision. The number of spherical waves is defined as $L$ representing the maximal degree of spherical waves taken into account. In the numerical results above, the number of spherical waves used was [76]

$$L = L_{\max} = \lceil ka + 7\sqrt[3]{ka} + 3 \rceil \tag{E.22}$$

with $a$ being the radius of a the smallest sphere centered at origin surrounding both objects. The effect of using smaller values $L < L_{\max}$ is shown in Fig. E.9 illustrating the convergence of the radiation efficiency based on the number of spherical waves used.

The above-defined test case can also be adapted to verify the results of the dual definition solution (E.18), *i.e.*, of the "internal" setup. To this point, the dipole antenna is moved to the center of the spherical shell. The size of the dipole is adjusted so that the radius of its smallest circumscribing sphere does not exceed the inner radius of the spherical shell. For the purpose of a comparison of the results with the time-domain solver of the CST Microwave Studio [238], the dielectric material forming the spherical body is, in this case, characterized by the real-valued relative permittivity $\varepsilon_{\mathrm{r}}$ and electric conductivity $\sigma$. The compared quantity is reflection coefficient $\Gamma$ (with reference impedance equal to $50\,\Omega$) and radiation efficiency.

Figure E.10 shows a comparison of the reflection coefficient $\Gamma$. As in the previous case, the results of two different numerical schemes are in satisfactory agreement, verifying the method presented in this paper.

The second comparison is the same as in the "external" case, namely the comparison of radiation efficiency, depending, in this case, on the thickness of $d/\ell$ of the spherical shell. It can be seen in Fig. E.11 that the radiation efficiency decreases with the increase of the thickness of the shell. The results were verified against CST

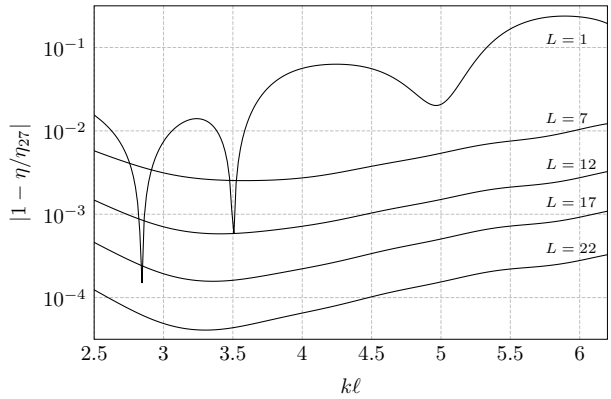


**Figure E.9:** Relative error in radiation efficiency of a dipole in the vicinity of a spherical shell with outer radius $r = 0.8\ell$. Individual lines are computed with a different value of $L$ and compared to the reference $\eta_{27}$ computed with $L = L_{\max} = 27$ determined from (E.22) for the electric size $ka \approx 31.4$.

for $d/\ell = 0.2$, with good agreement being observed considering the fact that two very different numerical methods were used.

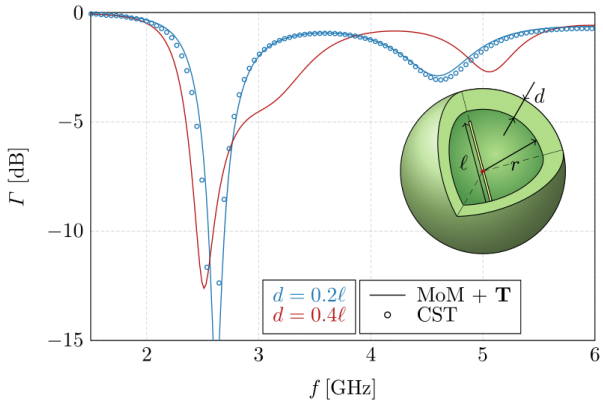


**Figure E.10:** Comparison of reflection coefficient $\Gamma$ seen at the delta-gap feed placed in the middle of the dipole with length $\ell = 0.05\,\mathrm{m}$ and an aspect ratio of $\ell/w = 50$, which is encapsulated inside a spherical shell of thickness $d$ made of a material with relative permittivity $\varepsilon_\mathrm{r} = 5$ and conductivity $\sigma = 0.1\,\mathrm{S}\cdot\mathrm{m}^{-1}$. The inner radius of the shell is $r = 0.6\ell$. Results for the spherical shell of thickness $d = 0.2\ell$ are displayed in blue and compared with the solution from the time-domain solver of the CST Studio Suite. The red line represents the solution for a shell of thickness $d = 0.4\ell$.

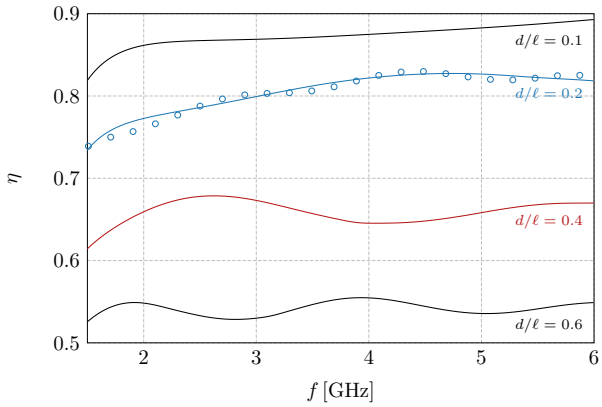


**Figure E.11:** Radiation efficiency $\eta$ of the dipole inside a spherical shell of various thickness $d$ made of the material with relative permittivity $\varepsilon_\mathrm{r} = 5$ and conductivity $\sigma = 0.1\,\mathrm{S}\cdot\mathrm{m}^{-1}$. Blue and red lines correspond to the same lines from Fig. E.10.

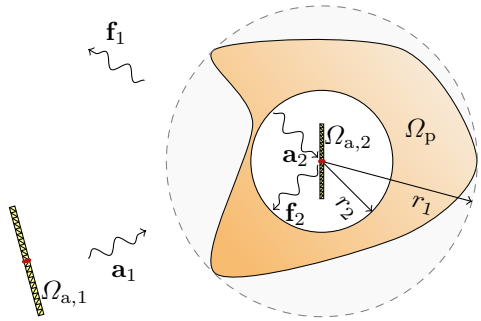


**Figure E.12:** The unified case of the hybrid method that involves a pair of objects described by the MoM ($\Omega_{\mathrm{a},1}$ and $\Omega_{\mathrm{a},2}$) and one object described with the T-matrix method ($\Omega_{\mathrm{p}}$).

## E.5 Unification of the External and Internal Formulation

Section E.3 describes in detail the derivation of the hybrid method for two different cases, the first one with object $\Omega_{\mathrm{a}}$ in the exterior of object $\Omega_{\mathrm{p}}$ and the second with object $\Omega_{\mathrm{a}}$ in the interior cavity carved in object $\Omega_{\mathrm{p}}$. This section combines these two cases. The scenario is depicted in Fig. E.12 and resembles the communication between two antennas, $\Omega_{\mathrm{a},1}$ and $\Omega_{\mathrm{a},2}$, one being in the exterior of a material body, while the second is in its interior, *e.g.*, a communication between a reader and an implanted antenna. As in the previous cases, the location of individual objects must fulfill the requirements, specifically that object $\Omega_{\mathrm{a},2}$ must fit within a sphere inscribed in object $\Omega_{\mathrm{p}}$ and object $\Omega_{\mathrm{a},1}$ cannot enter the circumscribing sphere of object $\Omega_{\mathrm{p}}$.

In order to describe this general scenario, objects $\Omega_{\mathrm{a},1}$ and $\Omega_{\mathrm{a},2}$ are described by impedance matrices $\mathbf{Z}_1$ and $\mathbf{Z}_2$, respectively, and the spherical wave description of object $\Omega_{\mathrm{p}}$ is generalized to

$$\begin{bmatrix}\mathbf{f}_1\\ \mathbf{a}_2\end{bmatrix} = \begin{bmatrix}\mathbf{T} & \boldsymbol{\Psi}\\ \boldsymbol{\Psi}^{\mathrm{T}} & \boldsymbol{\Gamma}\end{bmatrix}\begin{bmatrix}\mathbf{a}_1\\ \mathbf{f}_2\end{bmatrix}, \tag{E.23}$$

where matrix $\boldsymbol{\Psi}$ accounts for the field penetrating from inside of object $\Omega_{\mathrm{p}}$ outwards, while matrix $\boldsymbol{\Psi}^{\mathrm{T}}$ accounts for the field penetrating from outside of object $\Omega_{\mathrm{p}}$ inwards.

The interactions between all three objects $\Omega_{\mathrm{a},1}$, $\Omega_{\mathrm{a},2}$, and $\Omega_{\mathrm{p}}$ from Fig. E.12 are described by a system of equations

$$\begin{bmatrix}
\mathbf{Z}_1 & \mathbf{0} & \mathbf{0} & -\mathbf{U}_4^{\mathrm{T}} & \mathbf{0} & \mathbf{0}\\
\mathbf{0} & \mathbf{Z}_2 & -\mathbf{U}_1^{\mathrm{T}} & \mathbf{0} & \mathbf{0} & \mathbf{0}\\
\mathbf{0} & -\mathbf{U}_1 & \mathbf{0} & \mathbf{0} & \mathbf{0} & -\mathbf{1}\\
-\mathbf{U}_4 & \mathbf{0} & \mathbf{0} & \mathbf{0} & -\mathbf{1} & \mathbf{0}\\
\mathbf{0} & \mathbf{0} & \mathbf{0} & -\mathbf{1} & \mathbf{T} & \boldsymbol{\Psi}\\
\mathbf{0} & \mathbf{0} & -\mathbf{1} & \mathbf{0} & \boldsymbol{\Psi}^{\mathrm{T}} & \boldsymbol{\Gamma}
\end{bmatrix}\begin{bmatrix}\mathbf{I}_1\\ \mathbf{I}_2\\ \mathbf{a}_2\\ \mathbf{f}_1\\ \mathbf{a}_1\\ \mathbf{f}_2\end{bmatrix} = \begin{bmatrix}\widetilde{\mathbf{V}}_1^{\mathrm{i}}\\ \mathbf{V}_2^{\mathrm{i}}\\ \mathbf{0}\\ -\mathbf{a}^{\mathrm{i}}\\ \mathbf{0}\\ \mathbf{0}\end{bmatrix}, \tag{E.24}$$

where $\widetilde{\mathbf{V}}_1^{\mathrm{i}} = \mathbf{V}_1^{\mathrm{i}} + \mathbf{U}_1^{\mathrm{T}}\mathbf{a}^{\mathrm{i}}$. The definitions (E.14) and (E.18) are then only the special cases of this unified definition. When only the interaction of currents $\mathbf{I}_1$ and $\mathbf{I}_2$ is

| Layer | Thickness | Density |
|---|---|---|
| Brain white matter | 71.0 mm | $1041\,\mathrm{kg}\cdot\mathrm{m}^{-3}$ |
| Brain grey matter | 10.0 mm | $1045\,\mathrm{kg}\cdot\mathrm{m}^{-3}$ |
| Bone | 6.6 mm | $1908\,\mathrm{kg}\cdot\mathrm{m}^{-3}$ |
| Fat | 1.4 mm | $911\,\mathrm{kg}\cdot\mathrm{m}^{-3}$ |
| Skin | 1 mm | $1109\,\mathrm{kg}\cdot\mathrm{m}^{-3}$ |

**Table E.1:** Structure of the layer model of the human head [249].

required, the system (E.24) can partially be resolved, leading to the equation system

$$\begin{bmatrix} \mathbf{Z}_1 + \mathbf{U}_4^{\mathrm{T}}\mathbf{T}\mathbf{U}_4 & \mathbf{U}_4^{\mathrm{T}}\boldsymbol{\Psi}\mathbf{U}_1 \\ \mathbf{U}_1^{\mathrm{T}}\boldsymbol{\Psi}^{\mathrm{T}}\mathbf{U}_4 & \mathbf{Z}_2 + \mathbf{U}_1^{\mathrm{T}}\boldsymbol{\Gamma}\mathbf{U}_1 \end{bmatrix} \begin{bmatrix} \mathbf{I}_1 \\ \mathbf{I}_2 \end{bmatrix} = \begin{bmatrix} \widetilde{\mathbf{V}}_1^{\mathrm{i}} + \mathbf{U}_4^{\mathrm{T}}\mathbf{T}\mathbf{a}^{\mathrm{i}} \\ \mathbf{V}_2^{\mathrm{i}} + \mathbf{U}_1^{\mathrm{T}}\boldsymbol{\Psi}^{\mathrm{T}}\mathbf{a}^{\mathrm{i}} \end{bmatrix}. \tag{E.25}$$

## E.6 Results: Application

The previous section revealed how the external (E.14) and internal (E.18) formulation can be interlinked forming a general formulation (E.24). This section builds on this definition and shows its use in a simplified electromagnetic problem representing communication between two antennas, one of them being implanted in the human head and the second in its exterior. Models of this kind have previously been employed in the evaluation of fundamental bounds on implantable antennas [13] which is a field of research where the presented hybrid method can offer substantial advantages.

To highlight the benefits of the presented method, the human head is modeled as a spherical multi-layer, the parameters of which are specified in Table E.1. Material properties of different human tissues are obtained from [248].

The spherical multi-layer is centered at the origin and has a spherical cavity of radius 14.5 mm in which a PEC strip dipole antenna with length $\ell = 25\,\mathrm{mm}$ and aspect ratio of $\ell/w = 50$ is placed. Another PEC strip dipole antenna of the same dimensions is placed in the exterior of the multi-layer model at distance 20 mm from the outer surface of the head (the normal distance to the surface of the dipole). Both dipole antennas are fed in their geometric center by a delta-gap feed and their spatial orientation is the same. Both antennas are further supplemented with L-shaped impedance matching circuits [250] consisting of ideal lumped capacitors and inductors. Two sets of results presented in this section differ only in the matching frequency, which is 5 GHz or 7 GHz. Matching is realized with respect to terminal impedance $50\,\Omega$.

Communication of two antennas in a complex environment can be represented as a two-port network [250], in which delta-gap feeds of both antennas, together with matching circuits, form the ports. Scattering parameters [250] are used to describe the network.

Mismatch loss $\mathrm{ML} = -10\log_{10}\left(1 - |S_{ii}|^2\right)$ and reflectances $|S_{ii}|^2$ are shown in Fig. E.13 and Fig. E.14, respectively, assuming ports with a characteristic impedance of $50\,\Omega$.

The effect of matching on the transmittance of the system is shown in Fig. E.15. It can be observed that the frequency dependence of transmittance differs qualitatively

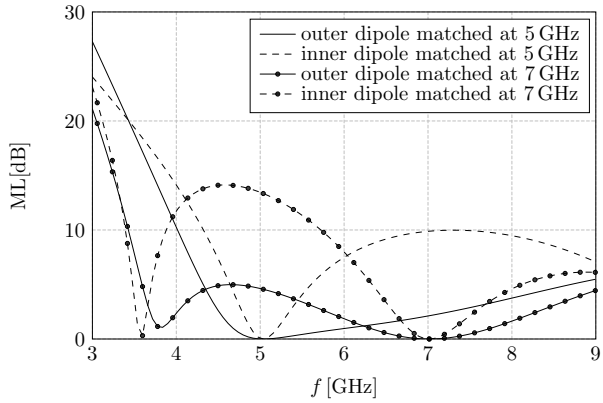


**Figure E.13:** The mismatch loss ML at the ports of the two-dipole system. Bare lines correspond to the matching at a frequency equal to 5 GHz. Lines with markers belong to the second case with impedance matching at a frequency equal to 7 GHz. Matching is performed with respect to an impedance of 50 Ω.

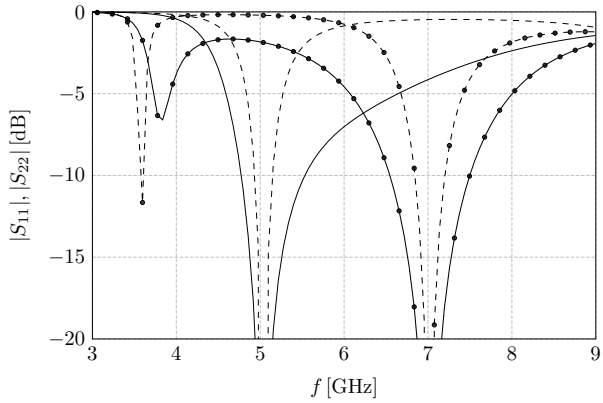


**Figure E.14:** Reflectances seen at ports of the system for the same setup as in Fig. E.13.

before and after the matching frequency. At frequencies below the matching frequency, the impedance mismatch, seen in Fig. E.13, highly affects the transmittance between the antennas. On the contrary, at higher frequencies, the effect of the impedance mismatch is weaker. In this frequency region, the transmittance is mostly dictated by the lossy multi-layer (human head model). This claim is supported by the dashed curve in Fig. E.15, which shows transmittance for the case of perfect matching at every frequency.

When the human body is exposed to a radio frequency electromagnetic field, the

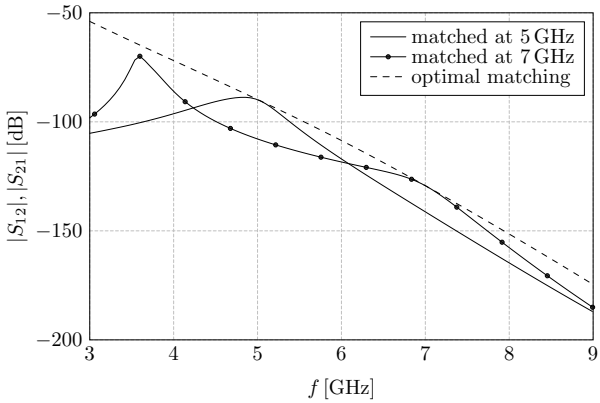


**Figure E.15:** Trasmittances $|S_{12}|^2$ and $|S_{21}|^2$ as a function of frequency in the system used in Fig. E.14. Full lines represent matching at a frequency of 5 GHz or 7 GHz. The dashed line corresponds to transmittance when perfect matching is provided at every frequency.

specific absorption rate (SAR)

$$\mathrm{SAR} = \frac{\sigma \left|\boldsymbol{E}\right|^2}{2\rho}, \tag{E.26}$$

where $\sigma$ is conductivity and $\rho$ is the mass density, becomes another metric of interest [251]. In the spherical multi-layer scenario described in this section, the evaluation of this quantity is a straightforward task the result of which is shown in Fig. E.16 for the case when both dipoles are excited by the same voltage across the delta-gap feed. The cycle mean input power to the system has been set to 1 W.

Another quantity of interest is the radiation pattern. The most important one being the radiation pattern of the outer radiator which will be greatly affected by the presence of the conducting spherical multi-layer. In order to evaluate the electric far field

$$\boldsymbol{F}\left(\vartheta,\varphi\right) = \lim_{r\to\infty}\{r\mathrm{e}^{\mathrm{j}kr}\boldsymbol{E}\left(\boldsymbol{r}\right)\}, \tag{E.27}$$

it is important to realize that the total the electric field is produced by waves $\mathbf{f}_1$ emanating from object $\Omega_\mathrm{p}$ and field (E.2) produced by object $\Omega_\mathrm{a}$. Since spherical wave decomposition is already employed in the formulation, it can also be advantageously used to express the electric far field. Notably, the field (E.2) is transformed into out-going spherical waves $\mathbf{f}_{\boldsymbol{J}} = -\mathbf{U}_1\mathbf{I}$ and is afterwards summed with waves $\mathbf{f}_1$. The resulting electric far field is written as

$$\boldsymbol{F}\left(\vartheta,\varphi\right) = \sqrt{Z}\sum_\alpha \left(f_{\boldsymbol{J}\alpha} + f_{1\alpha}\right)\mathrm{j}^{l+2-\tau}\mathbf{Y}_\alpha\left(\widehat{\boldsymbol{r}}\right), \tag{E.28}$$

where $\mathbf{Y}_\alpha$ are the vector spherical harmonics described in Appendix E.A. The radiation pattern generated by the studied setup, when only the external dipole is excited, is presented in Fig. E.17.

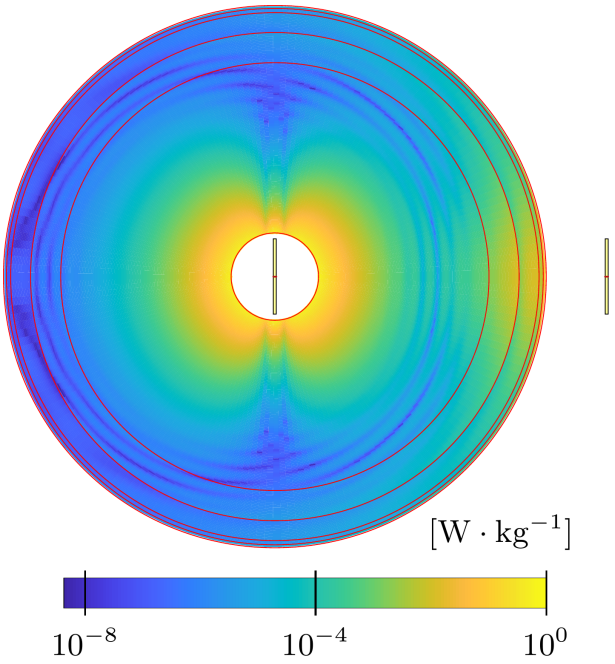


**Figure E.16:** Specific absorption rate at frequency $f = 5\,\mathrm{GHz}$ computed for the multi-layer model of the human head. The cycle mean input power to the system is set to 10 mW, where 8.1 mW belongs to the internal dipole and the rest to the external dipole.

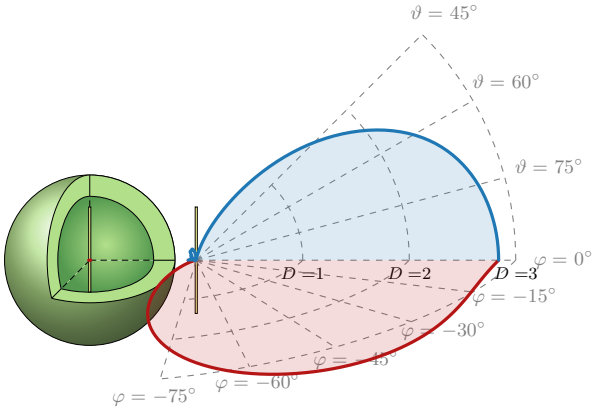


**Figure E.17:** Two principal cuts of a directivity radiation pattern at 5 GHz for the spherical multi-layer setup excited solely by the external dipole antenna. Partial directivity with polarization along $\vartheta$ direction is shown.

**Table E.2:** Computational times for a dipole inside a spherical shell

| evaluated task | computational time | |
|---|---|---|
| CST time-domain solver | 1700 s | |
| hybrid | $L_{\max} = 11$ ($ka = 0.79$) | $L_{\max} = 17$ ($ka = 3.14$) |
| • dipole $\mathbf{Z}$ | 1.8 s | |
| • dipole $\mathbf{U}_1$ | 1.2 s | 2.1 s |
| • spherical shell $\mathbf{\Gamma}$ | 0.32 s | 0.80 s |
| • hybrid solution | 0.024 s | 0.035 s |
| hybrid total time | 3.4 s | 4.8 s |

## E.7 Results: Computational Efficiency

Computational efficiency is an important aspect of every numerical method and is detailed in this section for the proposed hybrid. Two scenarios are addressed. The first scenario consists of a dipole inside a spherical shell that was already used in Section E.4.2. The second is a demanding setup of two dipoles communicating through a dielectric cube.

The computational times for the case of a dipole inside a spherical shell are shown in Table E.2. The table shows a comparison of total computation time with CST time-domain solver and also presents evaluation times for different parts of the hybrid scheme. Concerning the hybrid scheme, it can be stated that the time needed for the build-up and solution of the equation system (E.19) is negligible as compared to the previous stages. In this particular and favorable scenario, it can also be stated that the construction of matrix $\mathbf{\Gamma}$ is a minor burden even for the very high number of spherical waves $L_{\max} = 17$ since the evaluation of matrix $\mathbf{\Gamma}$ is analytical for a spherical multi-layer. The computation time is therefore dominated by the construction of matrix $\mathbf{Z}$ of the internal dipole and by the construction of coupling matrices $\mathbf{U}$, the evaluation time of which also scales with the number of spherical waves. The solution of the total system is equivalent to a few solutions to the dipole radiating in free space. When frequency sweep in the range from 1.5 GHz to 6 GHz is demanded, the evaluation time using CST solver is equivalent to approximately 500 runs of the hybrid method for $L_{\max} = 11$ (corresponding to the lowest frequency) and 350 runs for $L_{\max} = 17$ (corresponding to the highest frequency). This can be considered as great computational efficiency realizing that the computational time is almost independent of the material composition of the spherical multi-layer.

The scenario of two dipoles and a cube is sketched in Fig. E.18 and represents a computationally demanding setup for the hybrid method. This non-trivial scenario is used to analyze the convergence and computational complexity of the calculations depending on the value of $L$.

As can be seen from Table E.3 and Fig. E.19, the major computational burden here is the construction of matrices $\mathbf{T}$, $\mathbf{\Gamma}$, and $\mathbf{\Psi}$ which requires the construction of the impedance matrix of the cube and its LU decomposition for the evaluation of (E.41). For homogeneous obstacles, this burden can be reduced by the use of formulation based on surface equivalence [252] but will still be considerable realizing that the electrical size of the cube is $ka \approx 1$ at the lowest frequency and $ka \approx 12$ at the highest frequency and that the cube is made of a dielectric with relative

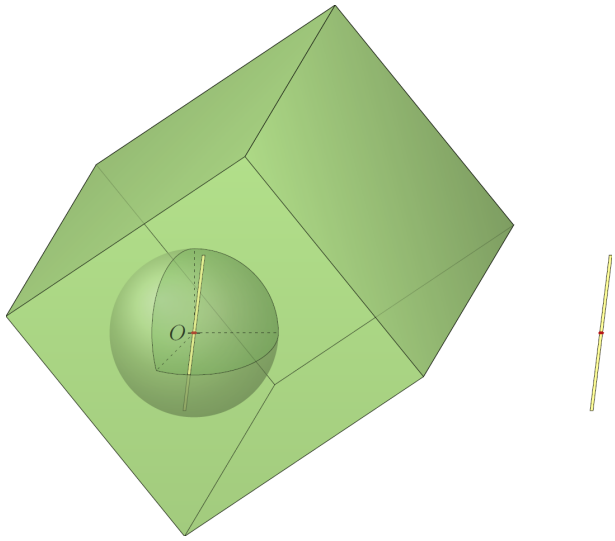


**Figure E.18:** Spatial arrangement of the two dipoles, one of which is placed in a vacuum bubble inside a dielectric cube.

permittivity $\varepsilon_r = 2$. Figure. E.19 also shows that even using only the dominant modes ($L = 1$) it is possible to obtain relative error of $10^{-1}$ and that the use of a larger number of spherical waves does not lead to a significant increase in computational cost.

For a single evaluation of this challenging scenario, the proposed hybrid method cannot compete with computational schemes offered by CST time-domain solved or by FEM+MoM hybrid offered by FEKO. The hybrid method can nevertheless be advantageous in scenarios when different positions/orientations of the dipoles are to be studied. In such case, only the coupling matrices $\mathbf{U}$ and the final hybrid solution must be recalculated for every new position/orientation of the dipoles unlike in the case of the used commercial solvers.

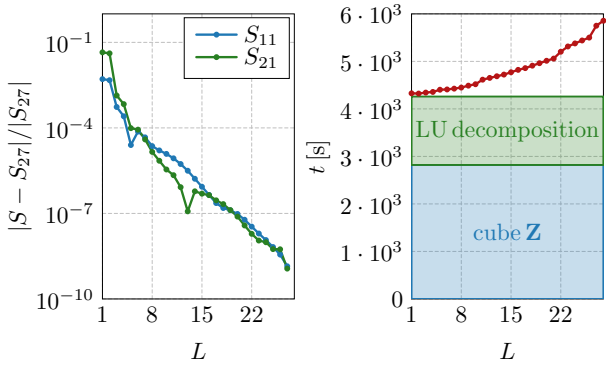


**Figure E.19:** Relative error in scattering parameters as seen from the two delta-gap ports placed at the center of each dipole from Fig. E.18 and the corresponding computational times. The electrical size of the cube is $ka \approx 6.7$. The individual points are calculated with different values of $L$ and their relative deviation is then determined by comparison with $S_{27}$ calculated with $L_{\max} = 27$, which was determined using (E.22). The main component of the calculation time is the determination of the impedance matrix and its LU decomposition. The scaling with the number of spherical waves is not significant.

**Table E.3:** Computational times for the setup sketched in Fig. E.18

| evaluated task | computation times | |
|---|---|---|
| CST time-domain solver | 310 s | total time |
| FEKO FEM+MoM | 470 s | one frequency point |
| hybrid | $L_{\max} = 14$ ($ka = 1.72$) | $L_{\max} = 39$ ($ka = 17.29$) |
| • dipole MoM | 3.2 s | 3.2 s |
| • dipole ext. $\mathbf{U}_1/\mathbf{U}_4$ | 1.9 s/2.6 s | 12 s/16 s |
| • dipole int. $\mathbf{U}_1/\mathbf{U}_4$ | 1.6 s/2.7 s | 9.7 s/14 s |
| • cube MoM3D | 2500 s | 2500 s |
| • cube $\mathbf{U}_1/\mathbf{U}_4$ | 78.0 s/180 s | 580 s/1000 s |
| • cube $\mathbf{T}$ | 1400 s | 1524 s |
| • cube $\mathbf{\Gamma} + \mathbf{\Psi}$ | 1400 s | 1500 s |
| • hybrid solution | 0.15 s | 0.54 s |
| hybrid total time | 5500 s | 7200 s |

## E.8 Discussion

Sections E.4 and E.6 illustrate the numerical performance of the method and the agreement of the results with solutions given by state-of-the-art commercial simulators. This section intends to discuss the strengths and weaknesses of the technique.

The major strength of the proposed computational scheme is the separated

treatment of a complex, but electrically small object, represented by the MoM matrix $\mathbf{Z}$ and of a typically simple, but electrically large body, described by its matrix $\mathbf{T}$. An essential feature connected with this separation is independence, in terms of how matrix $\mathbf{T}$ is determined. This, in many cases, allows the scatterer $\Omega_\mathrm{p}$ to be described using an analytic formula, which is, for example, the case of generic spherical, cylindrical, and planar multi-layer obstacles [48, 81] speeding up the entire hybrid method. The second essential property emanating from the separation of two interacting objects is the favorable scaling with the electrical size of object $\Omega_\mathrm{p}$. The computational complexity depends on the number of spherical waves used which is equal to $2L\,(L+2)$ which, for large electric sizes, is proportional to $(ka)^2$. In contrast, classical computational schemes using the segmentation of the body into mesh cells typically operate with $(ka)^3$ scaling. In that respect, the internal scenario described in Sec. E.3.2 with matrix $\mathbf{T}$ given analytically is the most favorable as there the necessary number of spherical waves is dictated by object $\Omega_\mathrm{a}$. The computational burden is then independent of the electrical size of object $\Omega_\mathrm{p}$. Finally, the method excels in scenarios when object $\Omega_\mathrm{p}$ is fixed and the various positioning of object $\Omega_\mathrm{a}$ are investigated. In such a case, the computationally demanding parts, matrices $\mathbf{Z}$ and $\mathbf{T}$, are calculated once and only the coupling matrix $\mathbf{U}_1$ is iteratively recalculated.

One of the important outcomes of this paper are relations (E.15), (E.19), and (E.25) containing the reduced description of the treated setup taking the point of view of object $\Omega_\mathrm{a}$ and resembling the use of Green's function in the presence of boundary conditions induced by object $\Omega_\mathrm{p}$ [241]. This leads to a reduction of memory and inversion demands but still leaves the possibility of operating with the complete system matrix allowing for the formulation of fundamental bounds on antenna and scattering metrics in the presence of parasitic scatterer residing in region $\Omega_\mathrm{p}$. This reduced description also removes the unpleasant numerical dynamics of transition matrix components corresponding to high-order spherical waves via the favorable multiplication by matrix $\mathbf{U}_4$. This last step can, in many cases, be pre-calculated, straightening even more the numerical robustness.

An important side product of the development of the hybrid method is an explicit formula to evaluate matrix $\mathbf{T}$ from matrix $\mathbf{Z}$ via relations (E.41), which generalizes previously published results [244, (12)] and [245, (20)]. Though this method is computationally intensive, it is numerically stable, even in cases when null-field exhibits instabilities [243]. The versatility of this approach was documented on an example of the PEC cube. it might be the only possibility for complex shaped objects. An important outcome of this connection is also a possibility to evaluate characteristic numbers of arbitrarily shaped objects with fourfold numerical dynamics as opposed to the classical approach [134, 246]. Considering these advantages and readily available codes based on the method of moments formulation of field integral equations, relations (E.41) should become a standard way to evaluate matrices $\mathbf{T}$, $\mathbf{\Psi}$, and $\mathbf{\Gamma}$.

As is the case of every numerical technique, the proposed method also exhibits weaknesses. An important one is the assumption that matrix $\mathbf{T}$ of an electrically large object can be obtained in a numerically effective way. This might be problematic for complex material objects since it requires solution to a linear equation system, see (E.41), in cases when analytical solution is not available. Another weakness is the assumption that the number of necessary spherical waves to achieve satisfactory precision is not exceedingly high. This forbids scenarios when near field interaction between the object $\Omega_\mathrm{p}$ and object $\Omega_\mathrm{a}$ dominates, as is the case of an antenna put in contact with a human head, or scenarios in which the object $\Omega_\mathrm{p}$ is considerably

off-centered as compared to the wavelength. Another limitation is the assumption that object $\Omega_{\rm a}$ must lie entirely outside a circumscribed sphere or inside an inscribed sphere of object $\Omega_{\rm p}$. This prevents us from studying situations in which object $\Omega_{\rm a}$ is positioned in protrusions of object $\Omega_{\rm p}$ as in, for example, the case of antennas mounted on electrically large carriers.

## E.9 Conclusion

A hybrid of the MoM and the T-matrix method was introduced combining the piecewise-defined basis functions approximating electrically small, however, potentially highly irregular objects, and spherical waves representing the scattering properties of a potentially electrically large obstacle of a regular shape. The presence of an inhomogeneous material is taken into account. The resulting system matrix, of numerically tractable size, is in most cases, suitable for finding a direct solution. As long as the electrically large object remains unchanged, the method allows for the efficient recalculation of only a low-rank coupling matrix when the positioning of small objects is of interest.

The method is based on a set of projection matrices which interconnect piecewise-defined and entire-domain representations. The side-product of the method is a simple formula for the determination of the transition matrix from the impedance matrix describing an arbitrary object. The projection matrices used can be utilized for characteristic mode decomposition quadruplicating the numerical dynamics of the conventional methods.

The hybrid method has been constructed for scenarios such as communication of an implanted antenna with an external reader including the exposure evaluation. Since the system matrix is explicitly determined and stored in a computer's memory, the method makes it possible to employ eigenvalue methods and determine fundamental bounds on a variety of physical phenomena. This is a subject of ongoing research.

## E.A Spherical Vector Waves Expansions

The spherical vector waves are defined as triplets ($\tau = 1, 2, 3$) of functions $\mathbf{u}^{(p)}_{\tau\sigma ml}(k\boldsymbol{r}) = \mathbf{u}^{(p)}_{\tau\beta}(k\boldsymbol{r})$ [48], where only two of these are needed for the purpose of this paper. Namely,

$$\begin{aligned} \mathbf{u}^{(p)}_{1\beta}(k\boldsymbol{r}) &= \mathrm{R}^{(p)}_{1l}(kr)\,\mathbf{Y}_{1\beta}(\widehat{\boldsymbol{r}}), \\ \mathbf{u}^{(p)}_{2\beta}(k\boldsymbol{r}) &= \mathrm{R}^{(p)}_{2l}(kr)\,\mathbf{Y}_{2\beta}(\widehat{\boldsymbol{r}}) + \mathrm{R}^{(p)}_{3l}(kr)\,\mathbf{Y}_{3\beta}(\widehat{\boldsymbol{r}}), \end{aligned} \tag{E.29}$$

where $\boldsymbol{r}$ is the radius vector with relations $\widehat{\boldsymbol{r}} = \boldsymbol{r}/r$ and $r = |\boldsymbol{r}|$. Multi-index $\beta$ combines indices $l \in \{1, \ldots, L\}$ (degree), $m \in \{0, \ldots, l\}$ (order) and $\sigma = \{\text{even}, \text{odd}\}$ (parity). Function $\mathrm{R}^{(p)}_{\tau l}$ specifies the radial function [185] as

$$\begin{aligned} \mathrm{R}^{(p)}_{1l}(kr) &= \mathrm{z}^{(p)}_{l}(kr), \\ \mathrm{R}^{(p)}_{2l}(kr) &= \frac{\left(kr\,\mathrm{z}^{(p)}_{l}(kr)\right)'}{kr}, \\ \mathrm{R}^{(p)}_{3l}(kr) &= \sqrt{l(l+1)}\,\frac{\mathrm{z}^{(p)}_{l}(kr)}{kr}, \end{aligned} \tag{E.30}$$

in which $\mathrm{z}_l^{(p)}$ represents a spherical Bessel function of degree $l$ and the choice of its variation by superscript $p$ determines the type of the wave. Regular waves $\mathrm{z}_l^{(1)} = \mathrm{j}_l$ are given by the spherical Bessel function of the first kind, and out-going waves $\mathrm{z}_l^{(4)} = \mathrm{h}_l^{(2)}$ are given by the spherical Hankel function of the second kind. The vector spherical harmonics $\mathbf{Y}_\beta$ are defined as

$$\begin{array}{lcl} \mathbf{Y}_{1\beta}\left(\widehat{\boldsymbol{r}}\right) & = & \dfrac{1}{\sqrt{l\left(l+1\right)}}\nabla\times\left(\boldsymbol{r}\mathrm{Y}_\beta\left(\widehat{\boldsymbol{r}}\right)\right), \\ \mathbf{Y}_{2\beta}\left(\widehat{\boldsymbol{r}}\right) & = & \widehat{\boldsymbol{r}}\times\mathbf{Y}_{1\beta}\left(\widehat{\boldsymbol{r}}\right), \\ \mathbf{Y}_{3\beta}\left(\widehat{\boldsymbol{r}}\right) & = & \widehat{\boldsymbol{r}}\mathrm{Y}_\beta\left(\widehat{\boldsymbol{r}}\right), \end{array} \tag{E.31}$$

in which $\mathrm{Y}_\beta$ stands for the spherical harmonic

$$\mathrm{Y}_{\sigma lm} = \sqrt{\frac{2-\delta_{m0}}{2\pi}}\widetilde{\mathrm{P}}_l^m\left(\cos\vartheta\right)\left\{\begin{array}{c}\cos\left(m\varphi\right)\\ \sin\left(m\varphi\right)\end{array}\right\} \tag{E.32}$$

with $\widetilde{\mathrm{P}}_l^m$ being the normalized associated Legendre polynomial of degree $l$ and $\delta_{mn}$ being the Kronecker delta.

The spherical vector waves can be used to expand the dyadic Green's function for an electric field [48, 185] as

$$\boldsymbol{G}_{\mathrm{e}}\left(\boldsymbol{r}_1,\boldsymbol{r}_2\right) = -\mathrm{j}k\sum_\alpha \mathbf{u}_\alpha^{(1)}\left(k\boldsymbol{r}_<\right)\mathbf{u}_\alpha^{(4)}\left(k\boldsymbol{r}_>\right), \tag{E.33}$$

where $\boldsymbol{r}_{</>} = \boldsymbol{r}_{1/2}$ if $r_1 < r_2$ and $\boldsymbol{r}_{</>} = \boldsymbol{r}_{2/1}$ if $r_1 > r_2$ and multi-index $\alpha$ combines indices $\tau$ and $\beta$. A possible ordering for the multi-index $\alpha$ can be found in[76, (7)]. Substituting expansion (E.33) into (E.2) leads to

$$\boldsymbol{E}^{\mathrm{s}}\left(\boldsymbol{r}_1\right) = -k^2 Z\left\langle\sum_\alpha \mathbf{u}_\alpha^{(1)}\left(k\boldsymbol{r}_<\right)\mathbf{u}_\alpha^{(4)}\left(k\boldsymbol{r}_>\right), \boldsymbol{J}\left(\boldsymbol{r}_2\right)\right\rangle. \tag{E.34}$$

Assuming that observation point $\boldsymbol{r}_1$ is outside of a sphere circumscribing source $\boldsymbol{J}$ and substituting (E.4), the relation is simplified to

$$\boldsymbol{E}^{\mathrm{s}}\left(\boldsymbol{r}_1\right) = -k\sqrt{Z}\sum_\alpha \left[\mathbf{U}_1\mathbf{I}\right]_\alpha \mathbf{u}_\alpha^{(4)}\left(k\boldsymbol{r}_1\right), \tag{E.35}$$

where projector $\mathbf{U}_p$ is defined in Section E.3. If, on contrary, there is a spherical cavity centered at origin and inscribed to source $\boldsymbol{J}$, and if the observation point is in the interior of this cavity, the analogous relation reads

$$\boldsymbol{E}^{\mathrm{s}}\left(\boldsymbol{r}_1\right) = -k\sqrt{Z}\sum_\alpha \left[\mathbf{U}_4\mathbf{I}\right]_\alpha \mathbf{u}_\alpha^{(1)}\left(k\boldsymbol{r}_1\right). \tag{E.36}$$

## E.B Transition Matrix for a Spherical Shell

There are several ways to determine the transition matrix, the core operator of the T-matrix method. Originally the solution was presented in [25] using the Null-field method which represents an efficient method of solving the scattering in terms of

surface integrals in the basis of spherical vector waves. Just as it is possible to determine the transition matrix, it is also possible to apply the same procedure to determine other scattering operators.

The transition matrix of a PEC spherical shell forms a diagonal matrix with elements

$$T_\alpha = -\frac{\mathrm{R}_\alpha^{(1)}(ka)}{\mathrm{R}_\alpha^{(4)}(ka)}, \tag{E.37}$$

while the internal scattering matrix $\mathbf{\Gamma}$ contains diagonal elements

$$\Gamma_\alpha = -\frac{\mathrm{R}_\alpha^{(4)}(ka)}{\mathrm{R}_\alpha^{(1)}(ka)}, \tag{E.38}$$

with $a$ being the radius of the shell. Notice that all the relations in this section are derived from the equality of tangent components of the fields at the interface and for this reason only $\alpha = \{\tau\sigma ml\}$ for $\tau = 1, 2$ should be used.

As with (E.37), the transition matrix of a sphere made of a homogeneous and isotropic dielectric can be determined as

$$T_\alpha = -\frac{\mathrm{R}_\alpha^{(1)}(ka)}{\mathrm{R}_\alpha^{(4)}(ka)} \frac{1 - \dfrac{Z_\odot}{Z} \dfrac{\mathrm{R}_\alpha^{(1)}(k_\odot a)\,\mathrm{R}_{\bar\alpha}^{(1)}(ka)}{\mathrm{R}_{\bar\alpha}^{(1)}(k_\odot a)\,\mathrm{R}_\alpha^{(1)}(ka)}}{1 - \dfrac{Z_\odot}{Z} \dfrac{\mathrm{R}_\alpha^{(1)}(k_\odot a)\,\mathrm{R}_{\bar\alpha}^{(4)}(ka)}{\mathrm{R}_{\bar\alpha}^{(1)}(k_\odot a)\,\mathrm{R}_\alpha^{(4)}(ka)}}, \tag{E.39}$$

where quantities with the subscript $_\odot$ belong to the material of the sphere and $\bar\alpha = \bar\tau\sigma ml$ is the index dual to index $\alpha$, where $\bar 1 = 2$ and $\bar 2 = 1$.

In addition to the transition matrix of the material sphere, it is also possible to determine matrix $\mathbf{\Gamma}$ of a spherical cavity inside a homogeneous isotropic dielectric as

$$\Gamma_\alpha = -\frac{\mathrm{R}_\alpha^{(4)}(k_\odot a)}{\mathrm{R}_\alpha^{(1)}(k_\odot a)} \frac{1 - \dfrac{Z}{Z_\odot} \dfrac{\mathrm{R}_\alpha^{(4)}(ka)\,\mathrm{R}_{\bar\alpha}^{(4)}(k_\odot a)}{\mathrm{R}_{\bar\alpha}^{(4)}(ka)\,\mathrm{R}_\alpha^{(4)}(k_\odot a)}}{1 - \dfrac{Z}{Z_\odot} \dfrac{\mathrm{R}_\alpha^{(4)}(ka)\,\mathrm{R}_{\bar\alpha}^{(1)}(k_\odot a)}{\mathrm{R}_{\bar\alpha}^{(4)}(ka)\,\mathrm{R}_\alpha^{(1)}(k_\odot a)}} \tag{E.40}$$

where $_\odot$ indicates quantities that pertain to the cavity. Notice that if the absolute value of the wavenumber in the material of the background medium approaches infinity, then relations (E.39) and (E.40) approach those for the PEC shell (E.37) and PEC cavity (E.38), respectively.

## E.C Relation Between MoM and Spherical Matrices

Consider a generalized description (E.23) of a scatterer from Fig. E.2. Consider that this scatterer is also described by matrix $\mathbf{Z}$. Projector $\mathbf{U}_p$ introduced in Sec. E.3 can then be used to interlink these two descriptions as

$$\begin{bmatrix} \mathbf{T} & \mathbf{\Psi} \\ \mathbf{\Psi}^{\mathrm{T}} & \mathbf{\Gamma} \end{bmatrix} = \begin{bmatrix} -\mathbf{U}_1\mathbf{Z}^{-1}\mathbf{U}_1^{\mathrm{T}} & -\mathbf{U}_1\mathbf{Z}^{-1}\mathbf{U}_4^{\mathrm{T}} + \mathbf{1} \\ -\mathbf{U}_4\mathbf{Z}^{-1}\mathbf{U}_1^{\mathrm{T}} + \mathbf{1} & -\mathbf{U}_4\mathbf{Z}^{-1}\mathbf{U}_4^{\mathrm{T}} \end{bmatrix}, \tag{E.41}$$

which can be deduced from relations between vectors $\mathbf{a}, \mathbf{f}$ and $\mathbf{I}, \mathbf{V}$. In this way the spherical wave matrices can be numerically evaluated for an arbitrarily shaped object. Relations (E.41) generalize those published in [244, (12)] and [245, (20)] by matrices $\mathbf{\Psi}$ and $\mathbf{\Psi}^{\mathrm{T}}$.

For a volumetric PEC obstacle, relation (E.41) is also tightly connected to the Null-field method [25, 48]. There, relation $\mathbf{T}\mathbf{U}_4 = -\mathbf{U}_1$ is proposed [48, (Chap. 9.1)] as an algebraic possibility to obtain matrix $\mathbf{T}$ (In [48], matrices $\mathbf{U}_1, \mathbf{U}_4$ are, apart from multiplicative constant, denoted as $\mathbf{R}, \mathbf{Q}$.). For spheroidal objects this method gives acceptable results. For object of complex shape, however, the relation $\mathbf{T}\mathbf{U}_4 = -\mathbf{U}_1$ cannot be precisely inverted, since necessary high order spherical waves make the pseudo-inversion of matrix $\mathbf{U}_4$ imprecise. For complex shaped objects, the prescription (E.41) is therefore a preferred way to obtain matrix $\mathbf{T}$. Unlike Null-field method, a matrix $\mathbf{T}$ can in this way be obtained also for planar objects.

## E.D Relation Between Transition Matrix and Characteristic Modes

Let us assume a lossless scatterer from Fig. E.2. On its external side, the characteristic mode decomposition is defined by (E.20), which can be generally rewritten as

$$\mathbf{Z}\mathbf{I}_n = (1 + \mathrm{j}\lambda_n)\,\mathbf{R}\mathbf{I}_n \tag{E.42}$$

in which $\mathbf{Z}$ represents the impedance matrix. Multiplying (E.42) from the left by $\mathbf{Z}^{-1}$ and using relation[6] $\mathbf{R} = \mathbf{U}_1^{\mathrm{T}}\mathbf{U}_1$, which was derived in [76], it is possible to deduce that

$$\mathbf{I}_n = (1 + \mathrm{j}\lambda_n)\,\mathbf{Z}^{-1}\mathbf{U}_1^{\mathrm{T}}\mathbf{U}_1\mathbf{I}_n. \tag{E.43}$$

Further multiplication from the left by projector $\mathbf{U}_1$ and the usage of relation (E.41) between matrices $\mathbf{Z}$ and $\mathbf{T}$ leads to

$$-\mathbf{U}_1\mathbf{I}_n = (1 + \mathrm{j}\lambda_n)\,\mathbf{T}\mathbf{U}_1\mathbf{I}_n. \tag{E.44}$$

Since $\mathbf{f}_{1,n} = -\mathbf{U}_1\mathbf{I}_n$ is an eigenvector of expansion coefficients corresponding to spherical waves propagating outwards, the characteristic modes might also be understood as eigenvectors of matrix $\mathbf{T}$

$$\mathbf{T}\mathbf{f}_{1,n} = -\frac{1}{1 + \mathrm{j}\lambda_n}\mathbf{f}_{1,n}, \tag{E.45}$$

which is consistent with [8], [9]. This relation also shows that characteristic modes of a spherical scatterer are spherical vector waves, since, in that case, matrix $\mathbf{T}$ is diagonal. As an example, characteristic modes of a PEC spherical shell can be evaluated by combining (E.45) and (E.37), which leads to

$$\lambda_\alpha = \mathrm{j}\left(1 - \frac{\mathrm{R}_\alpha^{(4)}(kr)}{\mathrm{R}_\alpha^{(1)}(kr)}\right). \tag{E.46}$$

Employing (E.30), this relation is identical to [97, (16) and (17)].

[6] This relation is only valid for a lossless scatterer.

For lossy scatterers, the decomposition (E.45) loses its relation to characteristic modes since definition (E.20) will not be equivalent to (E.42). It is also worth mentioning that, as opposed to (E.20) or (E.42), taking (E.45) as the defining relation of characteristic modes[7] can solve the long-lasting issues with characteristic modes of dielectric bodies [254]. This treatment only demands the knowledge of the transition matrix obtained from volume [246] or surface integral equations [255] unifying thus both approaches. The eigenmodes of matrix $\mathbf{T}$ can also shed new light on the connection between characteristic modes and natural modes [256].

## E.E Power Balance

Within a time harmonic steady state of convention $\exp\{\mathrm{j}\omega t\}$, where $\omega$ is the angular frequency, the balance of a cycle mean electromagnetic power is described as $P_{\boldsymbol{J}} = P_S + P_{\mathrm{lost}}$, where

$$P_{\boldsymbol{J}} = -\frac{1}{2}\mathrm{Re}\int\limits_V \boldsymbol{E}\cdot\boldsymbol{J}_{\mathrm{i}}^{*}\mathrm{d}V \tag{E.47}$$

is the power supplied by current source $\boldsymbol{J}_{\mathrm{i}}$ in volume $V$,

$$P_S = \frac{1}{2}\mathrm{Re}\oint\limits_S (\boldsymbol{E}\times\boldsymbol{H}^{*})\cdot\mathrm{d}\boldsymbol{S} \tag{E.48}$$

is the net power passing surface $S$, and $P_{\mathrm{lost}}$ is the power lost in volume $V$.

Imagine that surface $S$ is a spherical shell centered at origin and passing solely through material background. For the setup treated in this paper, the only source of power (E.47) is object $\Omega_{\mathrm{a}}$, which, when being within volume $V$, generates

$$P_{\boldsymbol{J}} = \frac{1}{2}\mathrm{Re}\left\{\mathbf{I}^{\mathrm{H}}\mathbf{V}^{\mathrm{i}}\right\}. \tag{E.49}$$

Assuming that the spherical wave decomposition

$$\boldsymbol{E}(\boldsymbol{r}) = k\sqrt{Z}\sum_{\alpha} a_\alpha\,\mathbf{u}_\alpha^{(1)}(k\boldsymbol{r}) + f_\alpha\,\mathbf{u}_\alpha^{(4)}(k\boldsymbol{r}) \tag{E.50}$$

is known on surface $S$, the net power passing the surface might be evaluated as [48]

$$P_S = \frac{1}{2}\left(|\mathbf{f}|^2 + \mathrm{Re}\left\{\mathbf{a}^{\mathrm{H}}\mathbf{f}\right\}\right), \tag{E.51}$$

where the outward and inward fluxes are naturally separated.

The power lost within object $\Omega_{\mathrm{a}}$ is evaluated as

$$P_{\mathrm{lost}}^{\mathrm{a}} = \frac{1}{2}\mathbf{I}^{\mathrm{H}}\mathrm{Re}\{\mathbf{Z}_\rho\}\,\mathbf{I}. \tag{E.52}$$

The evaluation of loss in object $\Omega_{\mathrm{p}}$ is most easily approached via (E.51).

[7] It seems to be their original definition, see [253] and [8].

With the above knowledge, it might be stated that the total radiated power in the scenario of Fig. E.3 reads

$$\begin{aligned} P_{\mathrm{rad}} &= \frac{1}{2}\left|\mathbf{f}_1 - \mathbf{U}_1\mathbf{I}\right|^2 = \\ &= \frac{1}{2}\left|\mathbf{f}_1\right|^2 + \frac{1}{2}\mathbf{I}^{\mathrm{H}}\mathrm{Re}\left\{\mathbf{Z}_0\right\}\mathbf{I} - \mathrm{Re}\left\{\mathbf{f}_1^{\mathrm{H}}\mathbf{U}_1\mathbf{I}\right\}, \end{aligned} \tag{E.53}$$

where the term $-\mathbf{U}_1\mathbf{I}$ represents the outgoing spherical waves generated by object $\Omega_{\mathrm{a}}$, see (E.16). The total lost power reads

$$\begin{aligned} P_{\mathrm{lost}} &= \frac{1}{2}\mathbf{I}^{\mathrm{H}}\mathrm{Re}\left\{\mathbf{Z}_\rho\right\}\mathbf{I} \\ &\quad - \frac{1}{2}\left(\left|\mathbf{f}_1\right|^2 + \mathrm{Re}\left\{\left(\mathbf{a}^{\mathrm{i}} - \mathbf{U}_4\mathbf{I}\right)^{\mathrm{H}}\mathbf{f}_1\right\}\right). \end{aligned} \tag{E.54}$$

Summing the lost and radiated power gives the total cycle mean power supplied by all sources which reads

$$P_{\mathrm{rad}} + P_{\mathrm{lost}} = P_{\boldsymbol{J}} - \frac{1}{2}\mathrm{Re}\left\{\mathbf{a}^{\mathrm{i},\mathrm{H}}\left(\mathbf{f}_1 - \mathbf{U}_1\mathbf{I}\right)\right\}, \tag{E.55}$$

where the last term (including the minus sign) is the cycle mean power supplied by spherical waves $\mathbf{a}^{\mathrm{i}}$.

The total power supplied by the sources can also be evaluated from (E.14) as

$$P_{\mathrm{rad}} + P_{\mathrm{lost}} = \frac{1}{2}\mathrm{Re}\left\{\begin{bmatrix}\mathbf{I}\\ \mathbf{f}_1\\ \mathbf{a}_1\end{bmatrix}^{\mathrm{H}}\begin{bmatrix}\mathbf{U}_1^{\mathrm{T}}\mathbf{a}^{\mathrm{i}} + \mathbf{V}^{\mathrm{i}}\\ -\mathbf{a}^{\mathrm{i}}\\ \mathbf{0}\end{bmatrix}\right\}. \tag{E.56}$$

The power balance in the scenarios of Fig. E.4 and Fig. E.12 can be obtained analogously.

## E.F Solver Settings

This appendix summarizes the setup of commercial solvers that were used for comparison with the proposed method.

- FEKO (ver. 2021.0.1, [232]) has been used with mesh structure of the dipole imported using NASTRAN data format [186] and dielectric spherical shell modeled using built-in CAD tools. The mesh structure of the dipole consisted of 396 triangles, and its excitation was realized by a delta-gap feed (mesh port). The spherical shell was discretized into 35390 tetrahedra. Analysis of the antenna was done using MoM solver, and the spherical shell was analyzed using FEM solver. The cube scenario, the same dipole models were used, and the material cube was described by a mesh structure made of 51800 tetrahedrons.
- CST (ver. 2021.01, [238]) has been used with all objects modeled using build-in CAD tools. The dipole was modeled as a strip with a centered physical gap of length $w/5$. The excitation of this structure was realized using a discrete s-parametric port with terminal impedance $Z_0 = 50\,\Omega$. The model was, in this case, discretized into $5.96 \cdot 10^6$ cells, and its analysis was performed using a

time-domain solver. In the case of the cube scenario, the same approach as in previous cases have been used, resulting in a model discretized into $1.6 \cdot 10^6$ cells.

# F About the Author

## F.1 Personal Information

**Name:** Vít Losenický
**Date of birth:** April 9, 1992
**Address:** Sukova třída 1935, 530 02, Pardubice, the Czech Republic
**Telephone:** + 420 605 322 416
**E-mail:** v.losenicky@gmail.com

## F.2 Education

**Czech Technical University in Prague**
Department of Electromagnetic Field
Faculty of Electrical Engineering
Technická 2, 166 27, Prague 6
Czech Republic

since 9/2016 **Doctoral studies**
Dissertation topic: Prospective methods for optimal design of electrically small antennas

**Czech Technical University in Prague**
Department of Electric Drives and Traction
Faculty of Electrical Engineering
Technická 2, 166 27, Prague 6
Czech Republic

9/2014 – 6/2016 **Master studies**
Program studied: Electrical Engineering, Power Engineering and Management
Specialization: Electrical Machines, Devices, and Drives
Thesis topic: Characteristic mode decomposition of a spherical shell

9/2011 – 6/2014 **Bachelor studies**
Program studied: Electrical Engineering, Power Engineering and Management
Thesis topic: Measurement and data processing with the Microblaze soft processor

## F.3 Work Experience

since July 2021 **Development Engineer** Porsche Engineering Services s.r.o., Prague
Development of software architecture design tool based on RFLP approach to system engineering.

Jan. 2019 – June 2021 **Researcher** Czech Technical University in Prague
Participation in the project *Fundamental bounds on electromagnetic radiation and scattering phenomena and associated realizable subforms* – implementation of the hybrid computational method.

Aug. 2014 – Dec. 2017 **Researcher** Czech Technical University in Prague
Developing the toolbox for antenna design and simulations in Matlab under the project *Tools for synthesis of antennas and sensors*. Responsible for the triangulation package and results visualisation.
More information at `antennatoolbox.com`.

## F.4 International Internships

Feb. 2019 **Lund University, Sweden**
Electrical and Information Technology, Faculty of Engineering LTH
prof. Mats Gustafsson – 1-month stay
Development of a hybrid numerical method combining the method of moments and the T-matrix method.

Jan. 2017 – Feb. 2018 **Polytechnic University of Valencia, Spain**
The Institute of Telecommunications and Multimedia Applications (iTEAM)
prof. Eva Antonino Daviu – 6-month stay
Study of the theory of characteristic modes and its use for antenna design.

## F.5 Publications

Unless explicitly noted, the authorship is divided equally among the listed authors.

### F.5.1 Journal Papers with Impact Factor Related to the Thesis

[1] M. Capek, P. Hazdra, M. Masek, and **V. Losenicky**, "Analytical Representation of Characteristic Mode Decomposition," *IEEE Transactions on Antennas and Propagation*, vol. 65, no. 2, pp. 713–720, Feb. 2017, DOI: 10.1109/TAP.2016.2632725.

[2] M. Capek, **V. Losenicky**, L. Jelinek, and M. Gustafsson, "Validating the Characteristic Modes Solvers," *IEEE Transactions on Antennas and Propagation*, vol. 65, no. 8, pp. 4134–4145, Aug. 2017, DOI: 10.1109/TAP.2017.2708094.

[3] **V. Losenicky**, L. Jelinek, M. Capek, and M. Gustafsson, "Dissipation Factors of Spherical Current Modes on Multiple Spherical Layers," *IEEE Transactions on Antennas and Propagation*, vol. 66, no. 9, pp. 4948–4952, Sept. 2018, DOI: 10.1109/TAP.2018.2841408.

[4] D. Tayli, M. Capek, L. Akrou, **V. Losenicky**, L. Jelinek, and M. Gustafsson, "Accurate and Efficient Evaluation of Characteristic Modes," *IEEE Transactions on Antennas and Propagation*, vol. 66, no. 12, pp. 7066–7075, Dec. 2018, DOI: 10.1109/TAP.2018.2869642.

[5] **V. Losenicky**, L. Jelinek, M. Capek, and M. Gustafsson, "Method of Moments and T-matrix Hybrid," *IEEE Transactions on Antennas and Propagation*, vol. 70, no. 5, pp. 3560–3574, May 2022, DOI: 10.1109/TAP.2021.3138265.

### F.5.2 Conference Papers Related to the Thesis

[1] M. Capek, L. Jelinek, **V. Losenicky**, M. Gustafsson, and K. Schab, "Unified Approach to Characteristic Modes," *International Symposium on Antennas and Propagation (APS)*, Singapore, Singapore, 2021.

[2] L. Jelinek, J. Liska, M. Capek, **V. Losenicky**, and M. Gustafsson, "Maximum Radiation Efficiency of Implanted Antennas Employing a Novel Hybrid Method," *International Symposium on Antennas and Propagation (APS)*, Singapore, Singapore, 2021.

[3] **V. Losenicky**, M. Capek, L. Jelinek, and M. Gustafsson, "Hybrid MoM/T-Matrix Method for Analysis of Interaction Between Objects," *the 14th European Conference on Antennas and Propagation (EuCAP)*, Copenhagen, Denmark, 2020.

[4] **V. Losenicky**, M. Capek, and L. Jelinek, "Approaching Q-Factor Bounds by Combining TM and TE Modes on a Cylindrical Shell," *the 13th European Conference on Antennas and Propagation (EuCAP)*, Krakow, Poland, 2019.

[5] M. Capek, D. Tayli, L. Akrou, **V. Losenicky**, L. Jelinek, and M. Gustafsson, "Accurate Evaluation of Characteristic Modes," *the 12th European Conference on Antennas and Propagation (EuCAP)*, London, United Kingdom, 2018.

[6] M. Capek, **V. Losenicky**, L. Jelinek, M. Gustafsson, and D. Tayli, "Numerical benchmark based on characteristic modes of a spherical shell," *International Symposium on Antennas and Propagation (APS)*, San Diego, California, USA, 2017.

### F.5.3 Conference Papers not Related to the Thesis

[1] M. Capek, L. Jelinek, M. Gustafsson, and **V. Losenicky**, "Topology Sensitivity in Method of Moments," *the 13th European Conference on Antennas and Propagation (EuCAP)*, Krakow, Poland, 2019.

[2] M. Capek, P. Hazdra, V. Adler, P. Kadlec, V. Sedenka, M. Marek, M. Masek,**V. Losenicky**, M. Strambach, M. Mazanek, and J. Rymus, "AToM: A Versatile MATLAB Tool for Antenna Synthesis," *the 12th European Conference on Antennas and Propagation (EuCAP)*, London, United Kingdom, 2018.

## F.6 Software

[1] M. Capek, V. Adler, P. Kadlec, V. Sedenka, M. Masek, **V. Losenicky**, M. Strambach, and P. Hazdra: AToM - Antenna Toolbox for MATLAB, [Software] 2017, `http://antennatoolbox.com`.

## F.7 Foundation Acknowledgment

The following projects supported the author's research:

- SGS19/168/OHK3/3T/13 – Electromagnetic structures and waves
- GA19-06049S – Fundamental bounds on electromagnetic radiation and scattering phenomena and associated realizable subforms
- TA04010457 – Tools for the synthesis of antennas and sensors
- SGS16/226/OHK3/3T/13 – Investigation of high frequency electromagnetic structures
- GJ15-10280Y – Source concept of electrically small antenna synthesis

# Bibliography


[1] S. A. Schelkunoff and H. T. Friis, *Antennas: Theory and Practice*. Wiley, 1952.

[2] J. D. Kraus, *Antennas*. McGraw-Hill, 1988.

[3] C. A. Balanis, *Modern Antenna Handbook*. Wiley, 2008.

[4] T. Pratt, *Satellite Communications Third Edition*, 3rd ed. Hoboken, NJ: Wiley-Blackwell, 2019.

[5] K. Fujimoto and K. Itoh, *Antennas for small mobile terminals*, 2nd ed. Norwood, MA: Artech House, Oct. 2018.

[6] C. A. Balanis, *Antenna Theory Analysis and Design*, 3rd ed. Wiley, 2005.

[7] M. Ohsaki, *Optimization of Finite Dimensional Structures*. CRC Press, 2011.

[8] R. J. Garbacz, "A generalized expansion for radiated and scattered fields," Ph.D. dissertation, The Ohio State Univ., 1968.

[9] R. F. Harrington and J. R. Mautz, "Theory of characteristic modes for conducting bodies," *IEEE Trans. Antennas Propag.*, vol. 19, no. 5, pp. 622–628, Sept. 1971.

[10] M. Cabedo-Fabres, E. Antonino-Daviu, A. Valero-Nogueira, and M. F. Bataller, "The theory of characteristic modes revisited: A contribution to the design of antennas for modern applications," *IEEE Antennas Propag. Mag.*, vol. 49, no. 5, pp. 52–68, Oct. 2007.

[11] C. W. Oseen, "Die einsteinsche nadelstichstrahlung und die maxwellschen gleichungen," *Ann. Phys.*, vol. 69, no. 19, pp. 202–204, 1922.

[12] M. Gustafsson, M. Cismasu, and B. L. G. Jonsson, "Physical bounds and optimal currents on antennas," *IEEE Trans. Antennas Propag.*, vol. 60, no. 6, pp. 2672–2681, June 2012.

[13] A. K. Skrivervik, M. Bosiljevac, and Z. Sipus, "Fundamental limits for implanted antennas: Maximum power density reaching free space," *IEEE Trans. Antennas Propag.*, vol. 67, no. 8, pp. 4978 – 4988, Aug. 2019.

[14] N. Peitzmeier and D. Manteuffel, "Upper bounds and design guidelines for realizing uncorrelated ports on multimode antennas based on symmetry analysis of characteristic modes," *IEEE Trans. Antennas Propag.*, vol. 67, no. 6, pp. 3902–3914, June 2019.

[15] S. Molesky, W. Jin, P. S. Venkataram, and A. W. Rodriguez, "T operator bounds on angle-integrated absorption and thermal radiation for arbitrary objects," *Physical Review Letters*, vol. 123, no. 257401, Dec. 2019.

[16] M. Gustafsson, K. Schab, L. Jelinek, and M. Capek, "Upper bounds on absorption and scattering," *New Journal of Physics*, vol. 22, p. 073013, July 2020.

[17] F. Monticone and A. Alù, "Physical bounds on electromagnetic invisibility and the potential of superconducting cloaks," *Photonics and Nanostructures - Fundamentals and Applications*, vol. 12, no. 4, pp. 330–339, Aug. 2014.

[18] ——, "Invisibility exposed: physical bounds on passive cloaking," *Optica*, vol. 3, no. 7, p. 718, 2016.

[19] C. Ehrenborg and M. Gustafsson, "Fundamental bounds on MIMO antennas," *IEEE Antennas and Wireless Propagation Letters*, vol. 17, no. 1, pp. 21–24, Jan. 2018.

[20] S. Molesky, P. Chao, W. Jin, and A. W. Rodriguez, "Global T operator bounds on electromagnetic scattering: Upper bounds on far-field cross sections," *Physical Review Research*, vol. 2, no. 3, July 2020.

[21] OpenAI. (2023, Nov.) Chatgpt-3.5. [Large language model]. [Online]. Available: https://chat.openai.com

[22] J. L. Volakis, A. Chatterjee, and L. C. Kempel, *Finite Element Method Electromagnetics: Antennas, Microwave Circuits, and Scattering Applications*. Wiley – IEEE Press, 1998.

[23] A. Taflove and S. C. Hagness, *Computational Electrodynamics: The Finite-Difference Time-Domain Method*. Artech House, 2004.

[24] R. F. Harrington, *Field Computation by Moment Methods*. Piscataway, New Jersey, United States: Wiley – IEEE Press, 1993.

[25] P. C. Waterman, "Matrix formulation of electromagnetic scattering," *Proceedings of the IEEE*, vol. 53, no. 8, pp. 805 – 812, Aug. 1965.

[26] G. Arfken, *Mathematical Methods for Physicists*, 3rd ed. San Diego: Academic Press, Inc., 1985.

[27] G. H. Golub and C. F. Van Loan, *Matrix Computations (3rd Ed.)*. USA: Johns Hopkins University Press, 1996.

[28] M. Gustafsson, D. Tayli, C. Ehrenborg, M. Cismasu, and S. Norbedo, "Antenna current optimization using MATLAB and CVX," *FERMAT*, vol. 15, no. 5, pp. 1–29, May–June 2016. [Online]. Available: http://www.e-fermat.org/articles/gustafsson-art-2016-vol15-may-jun-005/

[29] Y. Chen and C.-F. Wang, *Characteristic Modes – Theory and Applications In Antenna Engineering*. Wiley, 2015.

[30] J. Eichler, P. Hazdra, and M. Capek, "Aspects of mesh generation for characteristic mode analysis," *IEEE Antennas Propag. Mag.*, vol. 56, no. 6, pp. 172–183, June 2014.

[31] K. F. Warnick and W. C. Chew, "Error analysis of the moment method," *IEEE Antennas Propag. Mag.*, vol. 46, no. 6, pp. 38–53, Dec. 2004.

[32] T. Bernabeu-Jiménez, A. Valero-Nogueira, F. Vico-Bondia, and A. A. Kishk, "A comparison between natural resonances and characteristic mode resonances of an infinite circular cylinder," *IEEE Trans. Antennas Propag.*, vol. 65, no. 5, pp. 2759–2763, Feb. 2017.

[33] K. R. Schab, J. M. Outwater Jr., M. W. Young, and J. T. Bernhard, "Eigenvalue crossing avoidance in characteristic modes," *IEEE Trans. Antennas Propag.*, vol. 64, no. 7, pp. 2617–2627, July 2016.

[34] H. A. Wheeler, "Small antennas," *IEEE Trans. Antennas Propag.*, vol. 23, no. 4, pp. 462–469, July 1975.

[35] R. W. P. King, *The Theory of Linear Antennas.* Massachusetts, United States: Harvard University Press, 1956.

[36] J. L. Volakis, C. Chen, and K. Fujimoto, *Small Antennas: Miniaturization Techniques & Applications.* McGraw-Hill, 2010.

[37] K. Fujimoto and H. Morishita, *Modern Small Antennas.* Cambridge, Great Britain: Cambridge University Press, 2013.

[38] *145-2013 – IEEE Standard for Definitions of Terms for Antennas*, IEEE Std., Mar. 2014.

[39] A. D. Yaghjian, M. Gustafsson, and B. L. G. Jonsson, "Minimum Q for lossy and lossless electrically small dipole antenna," *Prog. Electromagn. Res.*, vol. 143, pp. 641–673, Dec. 2013.

[40] R. C. Hansen, *Electrically Small, Superdirective, and Superconductive Antennas.* Wiley, 2006.

[41] M. Gustafsson and S. Nordebo, "Optimal antenna currents for Q, superdirectivity, and radiation patterns using convex optimization," *IEEE Trans. Antennas Propag.*, vol. 61, no. 3, pp. 1109–1118, Mar. 2013.

[42] M. Gustafsson, C. Sohl, and G. Kristensson, "Illustrations of new physical bounds on linearly polarized antennas," *IEEE Trans. Antennas Propag.*, vol. 57, no. 5, pp. 1319–1327, May 2009.

[43] A. F. Peterson, S. L. Ray, and R. Mittra, *Computational Methods for Electromagnetics.* Wiley – IEEE Press, 1998.

[44] S. M. Rao, D. R. Wilton, and A. W. Glisson, "Electromagnetic scattering by surfaces of arbitrary shape," *IEEE Trans. Antennas Propag.*, vol. 30, no. 3, pp. 409–418, May 1982.

[45] B. N. Delaunay, "Sur la sphère vide," *Bull. Acad. Sci. URSS*, vol. 1934, no. 6, pp. 793–800, 1934.

[46] B. Galerkin, "On electrical circuits for the approximate solution of the laplace equation," *Vestnik Inzh*, vol. 19, pp. 897–908, 1915.

[47] W. C. Chew, M. S. Tong, and B. Hu, *Integral Equation Methods for Electromagnetic and Elastic Waves*. Morgan & Claypool, 2009.

[48] G. Kristensson, *Scattering of Electromagnetic Waves by Obstacles*. Edison, NJ: SciTech Publishing, an imprint of the IET, 2016.

[49] Z.-F. Fu and J. He, *Modal Analysis*. Oxford, England: Butterworth-Heinemann, Sep. 2001.

[50] L. D. Landau and L. M. Lifshitz, *Quantum Mechanics: Vol. 3 Nonrelativistic theory*, 3rd ed. Butterworth-Heinemann, 1981.

[51] A. D. Pierce, *Acoustics: An Introduction to Its Physical Principles and Applications*, 3rd ed. Cham, Switzerland: Springer Nature, July 2019.

[52] W. Geyi, *Foundations of antenna radiation theory: Eigenmode analysis*. Hoboken, NJ: Wiley-Blackwell, Mar. 2023.

[53] W. E. Arnoldi, "The principle of minimized iterations in the soluton of the matrix eigenvalue problem," *Appl. Math*, vol. 9, no. 17, pp. 17–29, 1951.

[54] C. Baum, "On the eigenmode expansion method for electromagnetic scattering and antenna problems, part i: some basic relations for eigenmode expansions and their relation to the singularity expansion," *Interaction Note*, vol. 229, p. 13, 1975.

[55] K. Schab, "Modal analysis of radiation and energy storage mechanisms on conducting scatterers," Ph.D. dissertation, University of Illinois at Urbana-Champaign, 2016.

[56] K. R. Schab and J. T. Bernhard, "Radiation and energy storage current modes on conducting structures," *IEEE Trans. Antennas Propag.*, vol. 63, no. 12, pp. 5601–5611, Dec. 2015.

[57] M. Gustafsson and M. Capek, "Maximum gain, effective area, and directivity," *IEEE Trans. Antennas Propag.*, vol. 67, no. 8, pp. 5282 – 5293, Aug. 2019.

[58] J. Liska, "Fundamental bounds on magnetic levitation and magnetic confinement," mathesis, diploma thesis, Czech Technical University in Prague, Czech Republic, 2021. [Online]. Available: https://dspace.cvut.cz/handle/10467/94783

[59] R. Garbacz, "Modal expansions for resonance scattering phenomena," *Proc. IEEE*, vol. 53, no. 8, pp. 856–864, Aug. 1965.

[60] V. Losenicky, L. Jelinek, M. Capek, and M. Gustafsson, "Method of moments and t-matrix hybrid," *IEEE Transactions on Antennas and Propagation*, vol. 70, no. 5, pp. 3560–3574, May 2022.

[61] M. Gustafsson, L. Jelinek, K. Schab, and M. Capek, "Unified theory of characteristic modes—Part I: Fundamentals," *IEEE Transactions on Antennas and Propagation*, vol. 70, no. 12, pp. 11 801–11 813, Dec. 2022.

[62] P. Dirac, *The principles of quantum mechanics*, 4th ed., ser. International Series of Monographs on Physics. Oxford, England: Clarendon Press, Jan. 1981.

[63] M. Capek, L. Jelinek, and M. Masek, "Finding optimal total active reflection coefficient and realized gain for multiport lossy antennas," *IEEE Transactions on Antennas and Propagation*, vol. 69, no. 5, pp. 2481–2493, May 2021.

[64] M. Capek and L. Jelinek, "Optimal composition of modal currents for minimal quality factor Q," *IEEE Trans. Antennas Propag.*, vol. 64, no. 12, pp. 5230–5242, Dec. 2016.

[65] (2022) Altair Feko. Altair. [Online]. Available: https://altairhyperworks.com/product/Feko

[66] (2023) CST Studio Suite. Dassault Systems. [Online]. Available: https://www.3ds.com/products-services/simulia/products/cst-studio-suite

[67] P. Ylä-Oijala and H. Wallén, "PMCHWT-based characteristic mode formulations for material bodies," *IEEE Trans. Antennas Propag.*, vol. 68, no. 3, pp. 2158–2165, Mar. 2020.

[68] P. Ylä-Oijala, M. Kuosmanen, and H. Wallén, "Integral operator-based characteristic mode theory for conducting, material, and lossy structures," *IEEE Trans. Antennas Propag.*, pp. 1–1, June 2023, early access.

[69] M. Capek, P. Hazdra, P. Hamouz, and J. Eichler, "A method for tracking characteristic numbers and vectors," *Prog. Electromagn. Res. B*, vol. 33, pp. 115–134, July 2011.

[70] E. Safin and D. Manteuffel, "Advanced eigenvalue tracking of characteristic modes," *IEEE Trans. Antennas Propag.*, vol. 64, no. 7, pp. 2628–2636, July 2016.

[71] Z. Miers and B. K. Lau, "Wide band characteristic mode tracking utilizing far-field patterns," *IEEE Antennas Wireless Propag. Lett.*, vol. 14, pp. 1658–1661, Jan. 2015.

[72] M. Masek, M. Capek, L. Jelinek, and K. Schab, "Modal tracking based on group theory," *IEEE Transactions on Antennas and Propagation*, vol. 68, no. 2, pp. 927–937, Feb. 2020.

[73] *1597.1-2008 – IEEE Standard for Validation of Computational Electromagnetics Computer Modeling and Simulations*, IEEE Std., 2008.

[74] *1597.2-2010 – IEEE Recommended Practice for Validation of Computational Electromagnetics Computer Modeling and Simulations*, IEEE Std., 2011.

[75] M. Capek, V. Losenicky, L. Jelinek, and M. Gustafsson, "Validating the characteristic modes solvers," *IEEE Trans. Antennas Propag.*, vol. 65, no. 8, pp. 4134–4145, Aug. 2017.

[76] D. Tayli, M. Capek, L. Akrou, V. Losenicky, L. Jelinek, and M. Gustafsson, "Accurate and efficient evaluation of characteristic modes," *IEEE Trans. Antennas Propag.*, vol. 66, no. 12, pp. 7066–7075, Dec. 2018.

[77] A. Einstein, "Zur elektrodynamik bewegter körper," *Annalen der Physik*, vol. 322, no. 10, pp. 891–921, 1905.

[78] W. Heisenberg, "Über den anschaulichen inhalt der quantentheoretischen kinematik und mechanik," *Zeitschrift für Physik*, vol. 43, no. 3-4, pp. 172–198, Mar. 1927.

[79] C. E. Shannon, "A mathematical theory of communication," *Bell System Technical Journal*, vol. 27, no. 3, pp. 379–423, July 1948.

[80] L. J. Chu, "Physical limitations of omni-directional antennas," *J. Appl. Phys.*, vol. 19, pp. 1163–1175, Dec. 1948.

[81] J. A. Stratton, *Electromagnetic Theory*. Wiley – IEEE Press, 2007.

[82] H. L. Thal, "Exact circuit analysis of spherical waves," *IEEE Trans. Antennas Propag.*, vol. 26, no. 2, pp. 282–287, Mar. 1978.

[83] ——, "New radiation Q limits for spherical wire antennas," *IEEE Trans. Antennas Propag.*, vol. 54, no. 10, pp. 2757–2763, Oct. 2006.

[84] R. E. Collin and S. Rothschild, "Evaluation of antenna Q," *IEEE Trans. Antennas Propag.*, vol. 12, no. 1, pp. 23–27, Jan. 1964.

[85] J. D. Jackson, *Classical Electrodynamics*, 3rd ed. Wiley, 1998.

[86] R. L. Fante, "Quality factor of general ideal antennas," *IEEE Trans. Antennas Propag.*, vol. 17, no. 2, pp. 151–157, Mar. 1969.

[87] J. S. McLean, "A re-examination of the fundamental limits on the radiation Q of electrically small antennas," *IEEE Trans. Antennas Propag.*, vol. 44, no. 5, pp. 672–675, May 1996.

[88] R. F. Harrington, "Antenna excitation for maximum gain," *IEEE Trans. Antennas Propag.*, vol. 13, no. 6, pp. 896–903, Nov. 1965.

[89] R. F. Harrington and J. R. Mautz, "Control of radar scattering by reactive loading," *IEEE Trans. Antennas Propag.*, vol. 20, no. 4, pp. 446–454, July 1972.

[90] W. Geyi, "A method for the evaluation of small antenna Q," *IEEE Trans. Antennas Propag.*, vol. 51, no. 8, pp. 2124–2129, Aug. 2003.

[91] G. A. E. Vandenbosch, "Reactive energies, impedance, and Q factor of radiating structures," *IEEE Trans. Antennas Propag.*, vol. 58, no. 4, pp. 1112–1127, Apr. 2010.

[92] ——, "Simple procedure to derive lower bounds for radiation Q of electrically small devices of arbitrary topology," *IEEE Trans. Antennas Propag.*, vol. 59, no. 6, pp. 2217–2225, June 2011.

[93] S. Boyd and L. Vandenberghe, *Convex Optimization*. Cambridge, Great Britain: Cambridge University Press, 2004.

[94] M. Shahpari and D. V. Thiel, "Fundamental limitations for antenna radiation efficiency," *IEEE Trans. Antennas Propag.*, vol. 66, no. 8, pp. 3894–3901, 2018.

[95] R. F. Harrington, "Effect of antenna size on gain, bandwidth, and efficiency," *J. Res. Nat. Bur. Stand.*, vol. 64-D, pp. 1–12, Jan.–Feb. 1960.

[96] K. Fujita and H. Shirai, "Theoretical limitation of the radiation efficiency for homogenous electrically small antennas," *IEICE T. Electron.*, vol. E98C, pp. 2–7, 2015.

[97] V. Losenicky, L. Jelinek, M. Capek, and M. Gustafsson, "Dissipation factors of spherical current modes on multiple spherical layers," *IEEE Trans. Antennas and Propag.*, vol. 66, no. 9, pp. 4948–4952, Sept. 2018.

[98] M. Gustafsson, "Efficiency and Q for small antennas using pareto optimality," in *IEEE International Symposium on Antennas and Propagation and USNC-URSI Radio Science Meeting*, 2013, pp. 2203–2204.

[99] F. Sarrazin, S. Pflaum, and C. Delaveaud, "Radiation efficiency optimization of electrically small antennas: Application to 3D folded dipole," in *International Workshop on Antenna Technology (iWAT)*, 2016, pp. 29–32.

[100] M. Capek, J. Eichler, and P. Hazdra, "Evaluating radiation efficiency from characteristic currents," *IET Microw. Antenna P.*, vol. 9, no. 1, pp. 10–15, Jan. 2015.

[101] L. Jelinek and M. Capek, "Optimal currents on arbitrarily shaped surfaces," *IEEE Trans. Antennas Propag.*, vol. 65, no. 1, pp. 329–341, Jan. 2017.

[102] C. Pfeiffer, "Fundamental efficiency limits for small metallic antennas," *IEEE Trans. Antennas Propag.*, vol. 65, pp. 1642–1650, Apr. 2017.

[103] H. L. Thal, "Radiation efficiency limits for elementary antenna shapes," *IEEE Trans. Antennas Propag.*, vol. 66, no. 5, pp. 2179–2187, May 2018.

[104] M. Capek, M. Gustafsson, and K. Schab, "Minimization of antenna quality factor," *IEEE Trans. Antennas Propag.*, vol. 65, no. 8, pp. 4115–4123, Aug. 2017.

[105] M. Capek, L. Jelinek, K. Schab, M. Gustafsson, B. L. G. Jonsson, F. Ferrero, and C. Ehrenborg, "Optimal planar electric dipole antennas: Searching for antennas reaching the fundamental bounds on selected metrics," *IEEE Antennas and Propagation Magazine*, vol. 61, no. 4, pp. 19–29, Aug. 2019.

[106] L. Jelinek, K. Schab, and M. Capek, "Radiation efficiency cost of resonance tuning," *IEEE Transactions on Antennas and Propagation*, vol. 66, no. 12, pp. 6716–6723, Dec. 2018.

[107] M. Gustafsson, M. Capek, and K. Schab, "Trade-off between antenna efficiency and Q-factor," Electromagnetic Theory Department of Electrical and Information Technology Lund University Sweden, Tech. Rep., 2017. [Online]. Available: http://lup.lub.lu.se/record/48c12514-eba2-4493-b8a6-c8777051a002

[108] ——, "Tradeoff between antenna efficiency and Q-factor," *IEEE Trans. Antennas Propag.*, vol. 67, no. 4, pp. 2482–2493, Apr. 2019.

[109] S. R. Best, "Low Q electrically small linear and elliptical polarized spherical dipole antennas," *IEEE Trans. Antennas Propag.*, vol. 53, no. 3, pp. 1047–1053, Mar. 2005.

[110] ——, "A discussion on the quality factor of impedance matched electrically small wire antennas," *IEEE Trans. Antennas Propag.*, vol. 53, no. 1, pp. 502–508, Jan. 2005.

[111] S. R. Best and D. L. Hanna, "A performance comparison of fundamental small-antenna designs," *IEEE Antennas Propag. Mag.*, vol. 52, no. 1, pp. 47–70, Feb. 2010.

[112] S. R. Best, "Electrically small resonant planar antennas," *IEEE Antennas Propag. Mag.*, vol. 57, no. 3, pp. 38–47, June 2015.

[113] D. F. Sievenpiper, D. C. Dawson, M. M. Jacob, T. Kanar, K. Sanghoon, L. Jiang, and R. G. Quarfoth, "Experimental validation of performance limits and design guidelines for small antennas," *IEEE Trans. Antennas Propag.*, vol. 60, no. 1, pp. 8–19, Jan. 2012.

[114] (2023) The Matlab. The MathWorks. [Online]. Available: www.mathworks.com

[115] A. D. Yaghjian and H. R. Stuart, "Lower bounds on the Q of electrically small dipole antennas," *IEEE Trans. Antennas Propag.*, vol. 58, no. 10, pp. 3114–3121, Oct. 2010.

[116] "Materials for characteristic modes benchmarking," 2017. [Online]. Available: https://elmag.fel.cvut.cz/CMbenchmark

[117] Y. Chen, K. Schab, M. Čapek, M. Mašek, B. K. Lau, H. Aliakbari, Y. Haykir, Q. Wu, W. Strydom, N. Peitzmeier, M. Jovicic, S. Genovesi, and F. A. Dicandia, "Benchmark problem definition and cross-validation for characteristic mode solvers," in *12th European Conference on Antennas and Propagation (EuCAP 2018)*, 2018, pp. 1–5.

[118] R. Shankar, *Principles of quantum mechanics*, 2nd ed. New York, NY: Springer, Dec. 2012.

[119] L. Jelinek, K. Schab, and M. Capek, "The radiation efficiency cost of resonance tuning," *IEEE Trans. Antennas Propag.*, vol. 66, no. 12, pp. 6716 – 6723, 2018.

[120] J. Liska, L. Jelinek, and M. Capek, "Fundamental bounds to time-harmonic quadratic metrics in electromagnetism: Overview and implementation," 2021.

[121] M. Alian and N. Noori, "A domain decomposition method for the analysis of mutual interactions between antenna and arbitrary scatterer using generalized scattering matrix and translation addition theorem of swfs," *IEEE Trans. Antennas Propag.*, pp. 1–1, 2023, early access.

[122] M. Capek, P. Hazdra, M. Mazanek, Z. Raida, and J. Rymus, "The antenna toolbox for MATLAB (AToM)," in *Proceedings of the 9th European Conference on Antennas and Propagation (EUCAP)*, Lisbon, Portugal, July 2015.

[123] M. Capek, L. Jelinek, and M. Masek, "A role of symmetries in evaluation of fundamental bounds," *IEEE Trans. Antennas Propag.*, vol. 69, no. 11, pp. 7729–7742, Nov. 2021.

[124] M. Capek and K. Schab, "Computational aspects of characteristic mode decomposition: An overview," *IEEE Antennas and Propag. Mag.*, vol. 64, no. 2, pp. 23–31, Apr. 2022.

[125] M. Capek, J. Lundgren, M. Gustafsson, K. Schab, and L. Jelinek, "Characteristic mode decomposition using the scattering dyadic in arbitrary full-wave solvers," *IEEE Trans. Antennas Propag.*, vol. 71, no. 1, pp. 830–839, Jan. 2023.

[126] E. Antonino-Daviu, M. Cabedo-Fabres, M. Gallo, M. F. Bataller, and M. Bozzetti, "Design of a multimode MIMO antenna using characteristic modes," in *Proceedings of the 3rd European Conference on Antennas and Propagation (EUCAP)*, Berlin, Germany, Mar. 2009, pp. 1840–1844.

[127] K. A. Obeidat, "Design methodology for wideband electrically small antennas based on the theory of characteristic modes," Ph.D. dissertation, The Ohio State University, 2010.

[128] J. J. Adams, "Characteristic modes for impedance matching and broadbanding of electrically small antennas," Ph.D. dissertation, Univ. of Illinois, 2011.

[129] J. G. Van Bladel, *Electromagnetic Fields*, 2nd ed. Wiley – IEEE Press, 2007.

[130] R. Mittra, Ed., *Numerical and Asymptotic Techniques in Electromagnetics*, ser. Topics in Applied Physics. Springer, 1975, vol. 3.

[131] M. Capek, L. Jelinek, P. Hazdra, and J. Eichler, "The measurable Q factor and observable energies of radiating structures," *IEEE Trans. Antennas Propag.*, vol. 62, no. 1, pp. 311–318, Jan. 2014.

[132] Q. Wu and D. Su, "A broadband model of the characteristic currents for rectangular plates," *IEEE Transactions on Electromagnetic Compatibility*, vol. 55, no. 4, pp. 725–732, Aug. 2013.

[133] H. Sagan, *Boundary and Eigenvalue Problems in Mathematical Physics*. Dover, 1989.

[134] R. F. Harrington and J. R. Mautz, "Computation of characteristic modes for conducting bodies," *IEEE Trans. Antennas Propag.*, vol. 19, no. 5, pp. 629–639, Sept. 1971.

[135] C. J. Carpenter, "Electromagnetic energy and power in terms of charges and potentials instead of fields," *Proc. IEE A*, vol. 136, no. 2, pp. 55–65, Mar. 1989.

[136] G. W. Stewart and J. Sun, *Matrix Perturbation Theory*. Academic Press, 1990.

[137] P. Hazdra, M. Capek, and J. Eichler, "Comments to 'Reactive Energies, Impedance, and Q Factor of Radiating Structures' by G. Vandenbosch," *IEEE Trans. Antennas Propag.*, vol. 61, no. 12, pp. 6266–6267, Dec. 2013.

[138] G. A. E. Vandenbosch, "Reply to "Comments on 'Reactive energies, impedance, and Q factor of radiating structures'"," *IEEE Trans. Antennas Propag.*, vol. 61, no. 12, p. 6268, Dec. 2013.

[139] M. Gustafsson and B. L. G. Jonsson, "Stored electromagnetic energy and antenna Q," *Prog. Electromagn. Res.*, vol. 150, pp. 13–27, Dec. 2014.

[140] E. Antonino-Daviu, "Analysis and design of antennas for wireless communications using modal methods," Ph.D. dissertation, UPV, Feb. 2008.

[141] M. Cismasu and M. Gustafsson, "Antenna bandwidth optimization with single frequency simulation," *IEEE Trans. Antennas Propag.*, vol. 62, no. 3, pp. 1304–1311, Mar. 2014.

[142] M. Capek, P. Hazdra, and J. Eichler, "A method for the evaluation of radiation Q based on modal approach," *IEEE Trans. Antennas Propag.*, vol. 60, no. 10, pp. 4556–4567, Oct. 2012.

[143] E. C. Jordan and K. G. Balmain, *Electromagnetic Waves and Radiating Systems.* Englewood Cliffs: Prentice-Hall, Inc., 1968.

[144] (2018) The Matlab. The MathWorks. [Online]. Available: www.mathworks.com

[145] (2016) CST Computer Simulation Technology. Dassault Systemes. [Online]. Available: http://www.cst.com/

[146] C.-H. Papas, *Theory of Electromagnetic Wave Propagation.* Dover, 1965.

[147] P. Hazdra, M. Capek, and J. Eichler, "Radiation Q-factors of thin-wire dipole arrangements," *IEEE Antennas Wireless Propag. Lett.*, vol. 10, pp. 556–560, May 2011.

[148] P. Hazdra, M. Capek, J. Eichler, and M. Mazanek, "The radiation Q-factor of a horizontal $\lambda/2$ dipole above ground plane," *IEEE Antennas Wireless Propag. Lett.*, vol. 13, pp. 1073–1075, June 2014.

[149] E. Newman, "Small antenna location synthesis using characteristic modes," *IEEE Trans. Antennas Propag.*, vol. 27, no. 4, pp. 530–531, July 1979.

[150] (2019) Antenna Toolbox for MATLAB (AToM). Czech Technical University in Prague. www.antennatoolbox.com. [Online]. Available: www.antennatoolbox.com

[151] N. N. Lebedev, *Special Functions & Their Applications.* Dover, 1972.

[152] (2016) FEKO. Altair. [Online]. Available: www.feko.info

[153] E. Group. Cem one. [Online]. Available: https://www.esi-group.com/software-services/virtual-environment/electromagnetics

[154] S. N. Makarov, *Antenna and EM Modeling with Matlab.* Wiley, 2002.

[155] M. Vogel, G. Gampala, D. Ludick, U. Jakobus, and C. Reddy, "Characteristic mode analysis: Putting physics back into simulation," *IEEE Antennas Propag. Mag.*, vol. 57, no. 2, pp. 307–317, Apr. 2015.

[156] R. Martens, J. Holopainen, E. Safin, J. Ilvonen, and D. Manteuffel, "Optimal dual-antenna design in a small terminal multiantenna system," *IEEE Antennas Wireless Propag. Lett.*, vol. 12, pp. 1700–1703, Dec. 2013.

[157] B. Yang and J. J. Adams, "Systematic shape optimization of symmetric MIMO antennas using characteristic modes," *IEEE Trans. Antennas Propag.*, vol. 64, no. 7, pp. 2668–2678, July 2016.

[158] J. Eichler, P. Hazdra, M. Capek, T. Korinek, and P. Hamouz, "Design of a dual-band orthogonally polarized L-probe-fed fractal patch antenna using modal methods," *IEEE Antennas Wireless Propag. Lett.*, vol. 10, pp. 1389–1392, Dec. 2011.

[159] WIPL-D d.o.o. (2016) WIPL-D. [Online]. Available: http://www.wipl-d.com/

[160] (2016) CST MWS. CST Computer Simulation Technology. [Online]. Available: http://www.cst.com/

[161] E. Safin and D. Manteuffel. (2017) CMC (Characteristc Mode Calculator). Leibniz Universitaet.

[162] D. Tayli. (2017) IDA (Integrated Development toolset for Antennas). Lund University.

[163] J. Mautz and R. Harrington, "Computer programs for characteristic modes of bodies of revolution," Syracuse University, Tech. Rep., 1971.

[164] K. F. Warnick and W. C. Chew, "Accuracy of the method of moments for scattering by a cylinder," *IEEE Trans. Microw. Theory Techn.*, vol. 48, no. 10, pp. 1652–1660, Oct. 2000.

[165] M. Capek, P. Hazdra, M. Masek, and V. Losenicky, "Analytical representation of characteristic modes decomposition," *IEEE Trans. Antennas Propag.*, vol. 65, no. 2, pp. 713–720, Feb. 2017.

[166] A. Sihvola, P. Yla-Oijala, S. Jarvenpaa, and J. Avelin, "Polarizabilities of platonic solids," *IEEE Trans. Antennas Propag.*, vol. 52, pp. 2226–2233, Sept. 2004.

[167] J. Helsing and K. Perfekt, "On the polarizability and capacitance of the cube," *Appl. Comput. Harmon. Anal.*, vol. 34, pp. 445–468, May 2013.

[168] J. Helsing and A. Karlsson, "Determination of normalized magnetic eigenfields in microwave cavities," *IEEE Trans. Antennas Propag.*, vol. 63, no. 5, pp. 1457–1467, May 2015.

[169] A. C. Woo, H. T. G. Wang, M. J. Schuh, and M. L. Sanders, "Benchmark plate radar targets for the validation of computational electromagnetics programs," *IEEE Antennas Propag. Mag.*, vol. 34, no. 6, pp. 52–56, Aug. 1992.

[170] M. D. Deshpande, C. R. Cockrell, F. B. Beck, and T. X. Nguyen, "Benchmarks of simple, generic, shaped plates for validation of low-frequency electromagnetic computational codes," *IEEE Antennas Propag. Mag.*, vol. 35, no. 4, pp. 58–63, Aug. 1993.

[171] G. A. E. Vandenbosch, "State-of-the-art in antenna software benchmarking: Are we there yet?" *IEEE Antennas and Propagation Magazine*, vol. 56, no. 4, pp. 300–308, Aug. 2014.

[172] K. F. Warnick, *Numerical Analysis for Electromagnetic Integral Equations*. Artech House, 2008.

[173] K. A. S. N. Jayasekera and I. R. Ciric, "Benchmark computations of the fields, losses, and forces for conducting spheroids in the proximity of current-carrying turns," *IEEE Trans. Magnetics*, vol. 42, no. 7, pp. 1802–1811, July 2006.

[174] T. F. Eibert and V. Hansen, "On the calculation of potential integrals for linear source distributions on triangular domains," *IEEE Trans. Antennas Propag.*, vol. 43, no. 12, pp. 1499–1502, Dec. 1995.

[175] D. Sievers, T. F. Eibert, and V. Hansen, "Correction to 'On the Calculation of Potential Integrals for Linear Source Distributions on Triangular Domains'," *IEEE Trans. Antennas Propag.*, vol. 53, no. 9, p. 3113, Sept. 2005.

[176] K. R. Schab and J. T. Bernhard, "A group theory rule for predicting eigenvalue crossings in characteristic mode analyses," *IEEE Antennas Wireless Propag. Lett.*, no. 16, pp. 944–947, Oct. 2017.

[177] D. J. Ludick, U. Jakobus, and M. Vogel, "A tracking algorithm for the eigenvectors calculated with characteristic mode analysis," in *Proceedings of the 8th European Conference on Antennas and Propagation (EUCAP)*, 2014, pp. 569–572.

[178] B. D. Raines and R. G. Rojas, "Wideband characteristic mode tracking," *IEEE Trans. Antennas Propag.*, vol. 60, no. 7, pp. 3537–3541, July 2012.

[179] J. H. Wilkinson, *The Algebraic Eigenvalue Problem.* Oxford University Press, 1988.

[180] R. F. Harrington, *Time-Harmonic Electromagnetic Fields*, 2nd ed. Wiley – IEEE Press, 2001.

[181] A. Jeffrey and H.-H. Dai, *Handbook of Mathematical Formulas and Integrals*, 4th ed. Academic Press, 2008.

[182] W. C. Chew and J. M. Song, "Gedanken experiments to understand the internal resonance problems of electromagnetic scattering," *Electromagnetics*, vol. 27, no. 8, pp. 457–471, Nov. 2007.

[183] P. M. Morse and H. Feshbach, *Methods of Theoretical Physics.* McGraw-Hill, 1953.

[184] L.-W. Li, X.-K. Kang, and M.-S. Leong, *Spheroidal Wave Functions in Electromagnetic Theory.* New York: Wiley, 2002.

[185] J. E. Hansen, Ed., *Spherical Near-Field Antenna Measurements.* United Kingdom: The Institution of Engineering and Technology, 2008.

[186] (2017) MSC NASTRAN. [Online]. Available: http://www.mscsoftware.com/support/

[187] D. A. Dunavant, "High degree efficient symmetrical Gaussian quadrature rules for the triangle," *International Journal for Numerical Methods in Engineering*, vol. 21, pp. 1129–1148, June 1985.

[188] J. B. Knorr, "Consequences of symmetry in the computation of characteristic modes for conducting bodies," *IEEE Trans. Antennas Propag.*, vol. 21, no. 6, pp. 899–902, Nov. 1973.

[189] T. K. Sarkar, E. L. Mokole, and M. Salazar-Palma, "An expose on internal resonance, external resonance and characteristic modes," *IEEE Trans. Antennas Propag.*, vol. 64, no. 11, pp. 4695–4702, Nov. 2016.

[190] T. Bernabeu-Jimenez, F. Vico-Bondia, A. Valero-Nogueira, M. Cabedo-Fabres, E. Antonino-Daviu, and F. Gallee, "Understanding the analytical formulation of the characteristic modes of a metallic sphere," in *Antennas and Propagation Society International Symposium (APSURSI), 2013 IEEE*, July 2013, pp. 1764–1765.

[191] Q. I. Dai, Q. S. Liu, H. U. I. Gan, and W. C. Chew, "Combined field integral equation-based theory of characteristic mode," *IEEE Trans. Antennas Propag.*, vol. 63, no. 9, pp. 3973–3981, Sept. 2016.

[192] E. Safin and D. Manteuffel, "Reconstruction of the characteristic modes on an antenna based on the radiated far field," *IEEE Trans. Antennas Propag.*, vol. 61, no. 6, pp. 2964–2971, June 2013.

[193] (2016) CEM One. ESI Group. [Online]. Available: www.esi-group.com/software-services/virtual-environment/electromagnetics

[194] Advanpix. (2016) Multiprecision Computing Toolbox for MATLAB. [Online]. Available: http://www.advanpix.com/

[195] Y. Saad, *Numerical Methods for large Eigenvalue Problems.* Society for Industrial and Applied Mathematics (SIAM), 2001.

[196] G. S. Smith, "Efficiency of electrically small antennas combined with matching networks," *IEEE Trans. Antennas Propag.*, vol. 25, pp. 369–373, May 1977.

[197] G. B. Arfken, H. J. Weber, and F. E. Harris, *Mathematical Methods for Physicists*, 6th ed. Academic Press, 2005.

[198] A. Karlsson, "On the efficiency and gain of antennas," *Prog. Electromagn. Res.*, vol. 136, pp. 479–494, 2013.

[199] M. N. O. Sadiku, *Numerical Techniques in Electromagnetics with Matlab*, 3rd ed. CRC Press, 2009.

[200] G. H. Golub and C. F. Van Loan, *Matrix Computations.* Johns Hopkins University Press, 2012.

[201] Y. Chen and C.-F. Wang, "Electrically small UAV antenna design using characteristic modes," *IEEE Trans. Antennas Propag.*, vol. 62, no. 2, pp. 535–545, Feb. 2014.

[202] W. C. Gibson, *The Method of Moments in Electromagnetics*, 2nd ed. Chapman and Hall/CRC, 2014.

[203] P. C. Waterman, "Symmetry, unitarity, and geometry in electromagnetic scattering," *Phys. Rev. D*, vol. 3, no. 4, pp. 825 – 839, 1971.

[204] M. Gustafsson and S. Nordebo, "Characterization of MIMO antennas using spherical vector waves," *IEEE Transactions on Antennas and Propagation*, vol. 54, no. 9, pp. 2679–2682, Sept. 2006.

[205] Y. G. Liu, W. C. Chew, L. Jiang, and Z. Qian, "A memory saving fast A-EFIE solver for modeling low-frequency large-scale problems," *Applied Numerical Mathematics*, vol. 62, no. 6, pp. 682 – 898, 2012.

[206] D. Zuras, M. Cowlishaw, A. Aiken, M. Applegate, D. Bailey, S. Bass, D. Bhandarkar, M. Bhat, D. Bindel, S. Boldo *et al.*, "IEEE standard for floating-point arithmetic," *IEEE Std 754-2008*, pp. 1–70, 2008.

[207] R. Burden, J. Faires, and A. Burden, *Numerical Analysis.* Cengage Learning, 2015.

[208] J. Song and W. C. Chew, "Error analysis for the truncation of multipole expansion of vector Green's functions [EM scattering]," *IEEE Microwave and Wireless Components Letters*, vol. 11, no. 7, pp. 311–313, July 2001.

[209] F. Johansson *et al.* (2013, December) Mpmath: a Python library for arbitrary-precision floating-point arithmetic (version 0.18). [Online]. Available: http://mpmath.org/

[210] Intel. (2017) Intel Math Kernel Library 2017 update 3. [Online]. Available: https://software.intel.com/en-us/mkl

[211] G. Angiulli and F. Venneri, "Use of the simultaneous diagonalization technique in the $Ax = \lambda Bx$ eigenproblem applied to the computation of the characteristic modes," *ACES Journal*, vol. 17, no. 3, pp. 232–238, Nov. 2002.

[212] A. G. Polimeridis. (2010) Direct evaluation method in computational electromagnetics (DEMCEM). [Online]. Available: https://github.com/thanospol/DEMCEM

[213] A. G. Polimeridis and T. V. Yioultsis, "On the direct evaluation of weakly singular integrals in Galerkin mixed potential integral equation formulations," *IEEE Trans. Antennas Propag.*, vol. 56, no. 9, pp. 3011–3019, Sept. 2008.

[214] A. G. Polimeridis and J. R. Mosig, "Complete semi-analytical treatment of weakly singular integrals on planar triangles via the direct evaluation method," *International journal for numerical methods in engineering*, vol. 83, no. 12, pp. 1625–1650, Aug. 2010.

[215] ——, "On the direct evaluation of surface integral equation impedance matrix elements involving point singularities," *IEEE Trans. Antennas Propag.*, vol. 10, pp. 599–602, June 2011.

[216] L. Dagum and R. Menon, "OpenMP: an industry standard API for shared-memory programming," *Computational Science & Engineering, IEEE*, vol. 5, no. 1, pp. 46–55, Jan.–Mar. 1998.

[217] F. W. J. Olver, D. W. Lozier, R. F. Boisvert, and C. W. Clark, *NIST Handbook of mathematical functions*. New York: Cambridge University Press, 2010.

[218] D. B. Davidson, *Computational Electromagnetics for RF and Microwave Engineering*, 2nd ed. Cambridge University Press, 2010.

[219] B. Kolundzija and A. Djordjevic, *Electromagnetic modeling of composite metallic and dielectric structures*. Boston: Artech House Publishers, 2002.

[220] O. Ergul and L. Gurel, *The Multilevel Fast Multipole Algorithm (MLFMA) for Solving Large-Scale Computational Electromagnetics Problems*. Wiley – IEEE Press, 2014.

[221] K. Zhao, M. N. Vouvakis, and J.-F. Lee, "The adaptive cross approximation algorithm for accelerated method of moments computations of EMC problems," *IEEE Transactions on Electromagnetic Compatibility*, vol. 47, pp. 763–773, Nov. 2005.

[222] V. V. S. Prakash and R. Mittra, "Characteristic basis function method: A new technique for efficient solution of method of moments matrix equations," *Microwave and Optical Technology Letters*, vol. 36, no. 2, pp. 95–100, Jan. 2003.

[223] R. D. Graglia, D. R. Wilton, and A. F. Peterson, "Higher order interpolatory vector bases for computational electromagnetics," *IEEE Transactions on Antennas and Propagation*, vol. 45, no. 3, pp. 329–342, Mar. 1997.

[224] J. R. Mautz and R. F. Harrington, "Radiation and scattering from bodies of revolution," *Applied Scientific Research*, vol. 20, no. 1, pp. 405–435, Jan. 1969.

[225] S. Wandzura, C. Thoringtonm, R. Turley, and L. Hamilton, "Fast Fourier transform techniques for solving the electric field integral equation for a periodic body," *IEE Proceedings H Microwaves, Antennas and Propagation*, vol. 139, no. 5, p. 401, Oct. 1992.

[226] A. Polimeridis, J. Villena, L. Daniel, and J. White, "Stable FFT-JVIE solvers for fast analysis of highly inhomogeneous dielectric objects," *Journal of Computational Physics*, vol. 269, pp. 280–296, July 2014.

[227] J.-M. Jin and J. Volakis, "A hybrid finite element method for scattering and radiation by microstrip path antennas and arrays residing in a cavity," *IEEE Transactions on Antennas and Propagation*, vol. 39, no. 11, pp. 1598–1604, Nov. 1991.

[228] S. Gedney, J. fa Lee, and R. Mittra, "A combined FEM/MoM approach to analyze the plane wave diffraction by arbitrary gratings," *IEEE Transactions on Microwave Theory and Techniques*, vol. 40, no. 2, pp. 363–370, Feb. 1992.

[229] M. Ali, T. Hubing, and J. Dreniak, "A hybrid FEM/MOM technique for electromagnetic scattering and radiation from dielectric objects with attached wires," *IEEE Transactions on Electromagnetic Compatibility*, vol. 39, no. 4, pp. 304–314, Nov. 1997.

[230] T. Chio and D. Schaubert, "Hybrid 3-D finite element/MoM analysis for antennas with thin dielectric cover," in *IEEE Antennas and Propagation Society International Symposium. 1998 Digest. Antennas: Gateways to the Global Network. Held in conjunction with: USNC/URSI National Radio Science Meeting (Cat. No. 98CH36194)*. IEEE, 1998.

[231] J. Liu and J.-M. Jin, "A novel hybridization of higher order finite element and boundary integral methods for electromagnetic scattering and radiation problems," *IEEE Transactions on Antennas and Propagation*, vol. 49, no. 12, pp. 1794–1806, Dec. 2001.

[232] (2021) FEKO. Altair. [Online]. Available: https://altairhyperworks.com/product/Feko

[233] ANSYS HFSS. [Online]. Available: www.ansys.com

[234] J. Yun, M. W. Ali, and T. H. Hubing, "EMC applications of the EMAP5 hybrid FEM/MOM code," in *1998 IEEE EMC Symposium. International Symposium on Electromagnetic Compatibility. Symposium Record (Cat. No.98CH36253)*, vol. 1, 1998, pp. 543–546.

[235] J. A. Stratton, P. Morse, L. J. Chu, J. Little, and F. J. Corbato, *Spheroidal wave functions: including tables of separation constants and coefficients.* New York; London: Published jointly by the Technology Press of M.I.T. and John Wiley ; Chapman and Hall, 1956.

[236] V. H. Rumsey, "Reaction concept in electromagnetic theory," *Phys. Rev.*, vol. 94, no. 6, pp. 1483–1491, June 1954.

[237] T. B. A. Senior and J. L. Volakis, *Approximate Boundary Conditions in Electromagnetics.* IEE, 1995.

[238] (2021) CST Studio Suite. Dassault Systems. [Online]. Available: https://www.3ds.com/products-services/simulia/products/cst-studio-suite

[239] WIPL-D d.o.o. (2020) WIPL-D. [Online]. Available: http://www.wipl-d.com/

[240] (2020) CEM One. ESI Group. [Online]. Available: www.esi-group.com/software-services/virtual-environment/electromagnetics

[241] D. G. Dudley, *Mathematical Foundations for Electromagnetic Theory.* IEEE Press, 1994.

[242] M. I. Mishchenko, L. D. Travis, and D. W. Mackowski, "T-matrix computations of light scattering by nonspherical particles: A review," *Journal of Quantitative Spectroscopy and Radiative Transfer*, vol. 55, no. 5, pp. 535 – 575, May 1996.

[243] M. I. Mishchenko, L. D. Travis, and A. A. Lacis, *Scattering, absorption, and emission of light by small particles.* Cambridge, England: Cambridge University Press, 2002.

[244] K. T. Kim and B. A. Kramer, "Direct determination of the T-Matrix from a MoM impedance matrix computed using the Rao-Wilton-Glisson basis function," *IEEE Transactions on Antennas and Propagation*, vol. 61, no. 10, pp. 5324–5327, Oct. 2013.

[245] J. Markkanen and A. J. Yuffa, "Fast superposition T-matrix solution for clusters with arbitrarily-shaped constituent particles," *Journal of Quantitative Spectroscopy and Radiative Transfer*, vol. 189, pp. 181–188, Mar. 2017.

[246] R. F. Harrington, J. R. Mautz, and Y. Chang, "Characteristic modes for dielectric and magnetic bodies," *IEEE Trans. Antennas Propag.*, vol. 20, no. 2, pp. 194–198, Mar. 1972.

[247] W. Yang, "Improved recursive algorithm for light scattering by a multilayered sphere," *Applied Optics*, vol. 42, no. 9, p. 1710, Mar. 2003.

[248] R. Andreuccetti, D. Fossi and C. Petrucci. (1997) An internet resource for the calculation of the dielectric properties of body tissues in the frequency range 10 Hz–100 GHz. Based on data published by C.Gabriel et al. in 1996. [Online]. Available: http://niremf.ifac.cnr.it/tissprop

[249] A. Drossos, V. Santomaa, and N. Kuster, "The dependence of electromagnetic energy absorption upon human head tissue composition in the frequency range of 300–3000 MHz," *IEEE Transactions on Microwave Theory and Techniques*, vol. 48, no. 11, pp. 1988–1995, Nov. 2000.

[250] D. M. Pozar, *Microwave Enginnering*, 4th ed. Wiley, 2011.

[251] International Commission on Non-Ionizing Radiation Protection (ICNIRP), "Guidelines for limiting exposure to electromagnetic fields (100 kHz to 300 GHz)," *Health Physics*, vol. 118, no. 5, pp. 483–524, May 2020.

[252] J.-M. Jin, *Theory and Computation of Electromagnetic Fields*. Wiley, 2010.

[253] C. G. Montgomery, R. H. Dicke, and E. M. Purcell, *Principles of Microwave Circuits*. New York, United States: McGraw-Hill, 1948.

[254] P. Yla-Oijala and H. Wallen, "PMCHWT-based characteristic mode formulations for material bodies," *IEEE Transactions on Antennas and Propagation*, vol. 68, no. 3, pp. 2158–2165, Mar. 2020.

[255] Y. Chang and R. F. Harrington, "A surface formulation for characteristic modes of material bodies," *IEEE Trans. Antennas Propag.*, vol. 25, no. 6, pp. 789–795, Nov. 1977.

[256] S. Huang, J. Pan, and Y. Luo, "Study on the relationships between eigenmodes, natural modes, and characteristic modes of perfectly electric conducting bodies," *International Journal of Antennas and Propagation*, vol. 2018, p. 13, Apr. 2018.

# List of Figures

# List of Tables

# List of acronyms

| | |
|---|---|
| **AToM** | Antenna Toolfox for MATLAB |
| **CM** | characteristic mode |
| **CEM** | computational electromagnetism |
| **d-o-f** | degrees-of-freedom |
| **EFIE** | electric field integral equation |
| **ESA** | electrically small antenna |
| **EM** | electromagnetic |
| **FDTD** | finite-difference time-domain |
| **FEM** | finite element method |
| **GEP** | generalized eigenvalue problem |
| **IDA** | Integrated Development toolset for Antennas |
| **IEEE** | Institute of Electrical and Electronics Engineers |
| **MLFMA** | multilevel fast multipole algorithm |
| **MoM** | method of moments |
| **PEC** | perfect electric conductor |
| **QCQP** | quadratically constrained quadratic program |
| **RWG** | Rao-Wilton-Glisson |
| **SVD** | singular value decomposition |

# List of Symbols

The following tables explain the symbols used in the body of the thesis. The symbols used in the reprints of the individual articles in Appendices A–E are explained when they are first used.

| Symbol | Meaning | Units |
|---|---|---|
| $\mathcal{L}$, $\mathbf{L}$ | linear integrodifferential operator | — |
| $g$, $f$ | excitation and reaction of the system | — |
| $\alpha_n$ | expansion coefficient | — |
| $f_n$ | basis function | — |
| $w_n$ | testing function | — |
| $\hat{\boldsymbol{v}}$ | normal vector | — |
| $\delta_{mn}$ | Kronecker delta | — |
| $^{\mathrm{T}}$ | transpose | — |
| $^{\mathrm{H}}$ | conjugate (Hermitian) transpose | — |
| $_{\tan}$ | tangential part of a field | — |
| $\mathrm{j}$ | imaginary unit | — |
| $\Omega$ | object's region | — |
| $\mathbf{G}(\boldsymbol{r}, \boldsymbol{r}')$ | Green's dyadic | $\mathrm{m}^{-1}$ |
| $Z_0$ | wave impedance | $\Omega$ |
| $k$ | wavenumber | $\mathrm{m}^{-1}$ |
| $ka$ | electrical size | — |
| $\omega$ | angular frequency | $\mathrm{s}^{-1}$ |
| $P_n^{\mathrm{rad}}$ | radiated power of $n$-th mode | W |
| $W_n^{\mathrm{e}}$, $W_n^{\mathrm{m}}$ | stored electric/magnetic energy of $n$-th mode | J |
| $\boldsymbol{\psi}_i(\boldsymbol{r})$ | RWG basis function | $\mathrm{m}^{-1}$ |
| $\mathbf{Z}$ | impedance matrix[1] | $\Omega \cdot \mathrm{m}^2$ |
| $\mathbf{I}$ | current density expansion coefficients[1] | $\mathrm{A} \cdot \mathrm{m}^{-1}$ |
| $\mathbf{V}$ | excitation vector[1] | $\mathrm{V} \cdot \mathrm{m}$ |
| $\boldsymbol{J}_S$ | surface current density | $\mathrm{A} \cdot \mathrm{m}^{-2}$ |

[1] Depends on the choice of basic functions. In this case, the RWG basic functions are selected.

| Symbol | Meaning | Units |
|---|---|---|
| $\boldsymbol{E}$ | electric field | $\mathrm{V} \cdot \mathrm{m}^{-1}$ |
| $\boldsymbol{E}^{\mathrm{i}}(\boldsymbol{r})$ | incident electric field | $\mathrm{V} \cdot \mathrm{m}^{-1}$ |
| $\boldsymbol{E}^{\mathrm{s}}(\boldsymbol{r})$ | scattered electric field | $\mathrm{V} \cdot \mathrm{m}^{-1}$ |
| $a_n$, $\mathbf{a}$ | expansion coefficient of regular waves | $\mathrm{A} \cdot \sqrt{\Omega}$ |
| $f_n$, $\mathbf{f}$ | expansion coefficient of out-going waves | $\mathrm{A} \cdot \sqrt{\Omega}$ |
| $\mathbf{u}_\alpha^{(1)}(k\boldsymbol{r}')$ | regular spherical vector wave | — |
| $\mathbf{u}_\alpha^{(4)}(k\boldsymbol{r}')$ | outgoing spherical vector wave | — |
| $\mathbf{T}$ | T-matrix | — |
| $\mathbf{A}$, $\mathbf{B}$ | matrices | — |
| $\mathbf{x}_n$ | eigenvector of generalized eigenvalue problem | — |
| $\lambda_n$ | eigenvalues (characteristic numbers) | — |
| $t_n$ | eigenvalues of T-matrix decomposition | — |
| $\mathbf{U}_1$ | projection matrix | $\sqrt{\Omega} \cdot \mathrm{m}$ |

Department of Electromagnetic Field
Faculty of Electrical Engineering
Czech Technical University in Prague
Technická 2
166 27, Prague 6
the Czech Republic

**Abstract**—Spherical wave expansion and numerical methods based on integral equations are utilized in this thesis to study various aspects of characteristic mode decomposition, the determination of fundamental bounds, and the hybridization of the method of moments and T-matrix. The numeric precision of characteristic mode solvers is validated and compared with the analytic solution, leading to recommendations and testing cases for authors of both academic and commercial packages. Inspired by the conclusions of this benchmark study, a new technique for decomposing characteristic modes is developed utilizing Green's function separation into regular and outgoing spherical vector waves. The results have higher numerical dynamics and are evaluated faster. The projection matrix between spherical vector waves and piece-wise basis functions has been established, featuring many direct applications, such as determining the radiation matrix, determining characteristic modes, and mediating the interaction between the impedance matrix and the T-matrix. The definition of the modal Q-factor is modified to be valid outside the modal resonance. The fundamental bound on radiation efficiency for an arrangement of two concentric spherical shells is found analytically. This study helps to understand the thin-sheet model used for other numerical models and to estimate its precision based on comparisons with a numerical code. Finally, a hybrid method for analyzing the interaction between an electrically small radiator and a passive scatterer is developed using the insights gained by studying the analytical representation of the characteristic modes to combine the method of moments with the T-matrix method.